

Syracuse University

SURFACE

Dissertations - ALL

SURFACE

May 2016

Vortices and Quasiparticles in Superconducting Microwave Resonators

Ibrahim Nsanzineza
Syracuse University

Follow this and additional works at: <https://surface.syr.edu/etd>



Part of the [Physical Sciences and Mathematics Commons](#)

Recommended Citation

Nsanzineza, Ibrahim, "Vortices and Quasiparticles in Superconducting Microwave Resonators" (2016).
Dissertations - ALL. 446.
<https://surface.syr.edu/etd/446>

This Dissertation is brought to you for free and open access by the SURFACE at SURFACE. It has been accepted for inclusion in Dissertations - ALL by an authorized administrator of SURFACE. For more information, please contact surface@syr.edu.

Abstract

Superconducting resonators with high quality factors are of great interest in many areas. However, the quality factor of the resonator can be weakened by many dissipation channels including trapped magnetic flux vortices and nonequilibrium quasiparticles which can significantly impact the performance of superconducting microwave resonant circuits and qubits at millikelvin temperatures. Quasiparticles result in excess loss, reducing resonator quality factors and qubit lifetimes. Vortices trapped near regions of large microwave currents also contribute excess loss. However, vortices located in current-free areas in the resonator or in the ground plane of a device can actually trap quasiparticles and lead to a reduction in the quasiparticle loss. In this thesis, we will describe experiments involving the controlled trapping of vortices for reducing quasiparticle density in the superconducting resonators. We provide a model for the simulation of reduction of nonequilibrium quasiparticles by vortices. In our experiments, quasiparticles are generated either by stray pair-breaking radiation or by direct injection using normal-insulator-superconductor (NIS)-tunnel junctions.

Vortices and Quasiparticles in Superconducting Microwave Resonators

BY

IBRAHIM NSANZINEZA

Master of Science, Syracuse University, 2012

Master's Diploma in Mathematical Sciences, University of Cape Town, 2008

Bachelor of Science, Kigali Institute of Education, 2005

DISSERTATION

Submitted in partial fulfillment of the requirements for the
degree of Doctor of Philosophy in Physics

Syracuse University

May 2016

Copyright 2016 Ibrahim Nsanzineza

All rights Reserved

Acknowledgments

I would like to express my wholehearted appreciation and thanks to my research advisor, Prof. B. L. T. Plourde. I can't say thank you enough for his tremendous help, support, assistance, valuable discussions and encouragement at every stage of my PhD studies.

I would like to send my thanks to my academic advisor, Prof. Alan Middleton, for his advice and interests in my progress during my Ph.D studies. He had many duties but he always checked with me about my progress and gave me some advice.

I owe many thanks to the following people for their support and assistance: Prof. Christina Marchetti, Prof. Mark Bowick, Prof. Saulson, Mrs Diane Sanderson, Mrs Penny Davies, Mrs Patti Ford, Mrs Patricia Whitmore, Mrs Linda Terramiggi and Mrs Yudaisy Salomon. I am indebted with plenty of thanks to members of physics department machine shop for their kindness and help they provided me. Many thanks to Charlie Brown, Lou Bouda, Phil Arnold and Lester Schmutzer.

I would like to say thank you to Prof. Robert McDermott and Dr. Umesh Patel, from the university of Wisconsin, for helping us to fabricate some of the devices we have used. I would like to say thank you to all the superconducting group members at Syracuse University for their informal discussions and assistance in any respect. Many blessings to Prof. Matthew LaHaye, Dr. Francisco Rouxinol, Dr. Daniela F. Bogorin, Dr. Mathew Hutchings.

Many thanks are also extended to my fellow colleagues Caleb Howington, Yu Hugo Hao, Haozhi Wang, and Kenneth Dodge Jr. I also worked with Chunhua Song during her final year of PhD, I want to thank her for teaching me to use Helium-3 fridge and some techniques in data analysis.

I offer my regards and blessings to Dr. Michael Defoe for helping me learn some fabrication skills and he gave me many rides to Cornell Nanoscale Science and Technology Facility (CNF) and introduced me to many CNF users. Thanks to Dr. Matthew Ware and Dr. Joe Strand to give me hand during initial wiring of the adiabatic demagnetization refrigerator.

I express thanks to my family for supporting me throughout my Ph.D. studies.

May God bless you all.

Contents

1	Introduction	1
2	Magnetic flux vortices and quasiparticles in superconductors	4
2.1	Introduction to superconductivity	4
2.2	Characteristic parameters of a superconductor	5
2.2.1	London equations and Meissner-Ochsenfeld effect	5
2.2.2	Coherence concept and Pippard's non-local modification of the London theory	6
2.2.3	Ginzburg-Landau theory	6
2.2.4	BCS theory and the energy gap Δ	7
2.2.5	Limiting cases for the electrodynamic response	8
2.3	Type-I and Type-II superconductors	9
2.4	Threshold field for trapping vortices	12
2.5	Vortex motion in superconductors	14
2.6	Thermal and nonequilibrium quasiparticles	17
2.6.1	Mattis-Bardeen equations for thermal quasiparticles	17
2.6.2	Nonequilibrium quasiparticles at millikelvin temperatures	18
3	Coplanar waveguide resonators	20
3.1	Lumped-elements resonators circuits	20
3.2	Distributed transmission-line resonators	21
3.2.1	Coplanar waveguide geometry: Half-wave and Quarter-wave resonators . . .	22
3.3	Loss mechanisms in microwave resonators	24
3.3.1	Microwave losses due to radiation and coupling to feedline	24
3.3.2	Microscopic Two-Level System (TLS) loss	25
3.3.3	Quasiparticles loss	26
3.3.4	Microwave loss due to vortices	26

4	Experimental setup and device design and fabrication	28
4.1	Microwave setup	28
4.1.1	Adiabatic Demagnetization Refrigerator	28
4.1.2	Experimental wiring in cryostat	32
4.1.3	Cryogenic microwave amplifier	33
4.1.4	Vector network analyzer and S-parameters	34
4.1.5	Shielding and generation of magnetic fields	35
4.2	Microwave resonator design	37
4.2.1	Resonator mask design and writing	38
4.3	Chip fabrication	38
4.3.1	HF cleaning versus ion-milling of silicon wafer	39
4.3.2	Wet etch of aluminum	39
4.4	Resonator measurement	41
4.4.1	Extracting resonator parameters with a 4-parameter fitting routine	42
4.4.2	Calibration of the input line and resonator input power	44
4.4.3	RRR and low temperature resistivity measurement	45
5	Trapping a single vortex in the microwave resonator	46
5.1	Introduction	46
5.2	Design of structures for resolving a single vortex	47
5.3	Field-cooled measurement	49
5.3.1	Trapping vortices in the ground plane and reducing background quasiparticles density	53
6	Numerical simulations of reduction of density of nonequilibrium quasiparticles due to trapped vortices	54
6.1	Introduction	54
6.2	Variation in loss with cryostat temperature	55
6.3	Quasiparticle diffusion equation	56
6.4	Conclusion	62
7	Resonator response against direct quasiparticle injection	63
7.1	Introduction to NIS tunnel junction	63
7.2	Sample fabrication	64
7.2.1	I-V characteristics of the NIS junction	65

CONTENTS	vii
7.2.2 Dependence of resonator quality factor on tunneling power	66
7.2.3 Effects of vortices on the quasiparticles loss	67
7.3 Effects of cuts in the ground plane on the quasiparticles loss	69
8 Nonlinear microwave response of vortices	71
8.1 Larkin-Ovchinnikov flux-flow nonlinearity	71
8.2 Sample design	73
8.3 Power dependence of internal loss at various applied magnetic field	74
8.4 Dependence of vortex loss on microwave power	76
8.5 Conclusion	77
9 Ongoing measurements, future directions, and conclusion	78
9.1 Ongoing measurements and future directions	78
9.2 Conclusions	81
Bibliography	82

List of Figures

2.1	Variation of superconducting energy gap with temperature. Right: plot using Eq. (2.12) for high temperature approximation and Left: plot using Eq. (2.14) for low temperature approximation.	7
2.2	A schematic illustrating the H-T diagrams of (a) Type-I and (b) Type-II superconductors.	9
2.3	Schematic representation of (a) magnetic field penetration of a type-II superconductor. The vortex is surrounded by screening currents. (b) The vortex represents a singularity in the order parameter. (c) The maximum field is at the center of vortex. From reference [1].	11
2.4	Gibbs free energy as a function of the applied magnetic field. The Gibbs free energy has its first minimum at the magnetic field B_0 . With pinning defects, vortices penetrate the superconductor at lower field B_p than the threshold field B_s when no pinning. From Stan et al. 2004 [2].	13
2.5	Plot of threshold cooling fields B_{th} for different width segments on resonator from [3] (filled circles) and $B_{th}(W)$ values for quarter-wave uniform-width resonators from separate device as discussed in text (open squares). Curve corresponds to Eq. (2.23) for $\xi = 235$ nm.	14
2.6	Variation of thermal quasiparticles with temperature for $T_c = 1.2$ K. Calculations based on Eq. 2.33.	17
3.1	Lumped elements in (a) parallel and (b) series resonant circuits.	20
3.2	Geometry of the CPW transmission line.	22
4.1	Temperatures vs. time for the 60 K (Red) and 3 K (Blue) stages of the pulse-tube refrigerator during an initial cooldown of the ADR cryostat from room temperature.	30
4.2	Cooling of FAA salt pill coupled to sample during adiabatic demagnetization.	31

4.3	Microwave measurement setup.	32
4.4	Noise temperature (Blue) and gain (Red) of HEMT amplifier, for temperature below 17K. These curves are taken from the Caltech datasheet for this HEMT.	33
4.5	Left: Vector Network Analyzer (VNA). Right: a circuit diagram for a two-port network.	34
4.6	Left: Schematic of cryostat including sample brass box and mount along with Helmholtz coil (not to scale). Right: Cryoperm shield mounted on the 3K plate.	35
4.7	Plot of calibration for converting applied current to magnetic field in the Helmholtz coil, the slope is $3.23 \mu\text{T}/\text{mA}$	36
4.8	Drawing of resonator design and simulated frequency response $ S_{21} $	37
4.9	Chip design in Cadence software.	38
4.10	Left: Optical micrographs of chip after wet etch. Right: Zoom-in of bulge region for vortex trapping near center of resonator.	39
4.11	Microwave measurement setup outside the ADR cryostat.	40
4.12	Chip wirebonded on a printed circuit board.	41
4.13	Magnitude and phase raw data of forward transmission S_{21} . The data was measured for a small span of (0.5 MHz) with 800 frequency points.	41
4.14	Magnitude and phase of background transmission. The blue points far away from the resonance were used to find a polynomial and linear fit functions for the magnitude and phase, respectively. The data was measured for a wide span of 6.0 MHz.	42
4.15	Plots of magnitude and phase after subtracting off the baseline transmission data.	43
4.16	Calibrated complex transmission data fitted with a 4-parameter fit model in complex plane.	43
4.17	Measurement of input coax cable attenuation from top to bottom of ADR cryostat. The measurement was done at room temperature	44
5.1	Optical micrographs of (a) entire resonator including feedline, (b) close-up of bulge region for vortex trapping near center of resonator, (c) close-up of coupling elbow and feedline. Schematic of resonator without turns (not to scale) along with standing-wave pattern of microwave current for (d) fundamental, (e) first-harmonic resonance. From Nsanzineza & Plourde, Physical Review Letters 113, 117002(2014) [3].	47
5.2	Power dependence of total resonator loss for the fundamental resonance 3.0713 GHz and coupling quality factor $Q_c = 765,000$. All field-cooled measurements were performed at sufficiently high powers, with $\sim 10^5$ photons in the resonator.	48

5.3	$1/Q_v(B)$ for fundamental resonance for cooling fields in the vicinity of $B_{th}(8\mu\text{m})$ for the central bulge region. Vertical dashed lines correspond to field steps $\Delta B = 5\mu\text{T}$. From Nsanzineza & Plourde, Phys. Rev. Lett. 113, 117002(2014) [3].	49
5.4	$1/Q_v(B)$ for fundamental (blue circles) and first harmonic (red squares) resonance – note different scales on loss axes. (insets) $ S_{21}(f) $ for (left) fundamental; (right) harmonic for $B = 41.7\mu\text{T}$ (no vortices) and $46.2\mu\text{T}$ (one-vortex step). From Nsanzineza & Plourde, Phys. Rev. Lett. 113, 117002(2014) [3].	50
5.5	Variation of current density along the width of the conductor trace of in middle of resonator in the bulge region. The current density is minimum at center of the conductor trace, and it is maximum along the edges. In the ground planes on either side of the bulge, the current density falls quickly from the edges of the gaps. Calculations based on equation 3.22.	51
5.6	Vortex loss plotted as a function of applied magnetic field. Vortices trapped in ground plane at vanishing current density reduce quasiparticles density.	53
6.1	Measurements of $1/Q$ vs. cryostat temperature for zero-field cooling for (a) fundamental, (b) harmonic resonance. The temperature of the cold-finger and sample remained below 140mK during the measurements. Dashed line is a guide to the eye for a quadratic dependence while the solid line corresponds to a linear dependence. From Nsanzineza & Plourde, Phys. Rev. Lett. 113, 117002(2014) [3].	55
6.2	Variation of the quasiparticle diffusion constant with energy. The calculations are based on equation 6.2.	57
6.3	(a) Simulated $n_{qp}(x)$ for several example cooling fields. Labels indicate vortex number in central bulge + coupling elbow. (b) Measured $1/Q_i(B)$ for harmonic, normalized by average of $1/Q_i$ below threshold field (points); computed normalized quasiparticle loss on harmonic from simulated $n_{qp}(x)$ (solid line). From Nsanzineza & Plourde, Phys. Rev. Lett. 113, 117002(2014) [3].	59
6.4	Simulated normalized quasiparticle loss on harmonic for different intervortex spacings for (i) 2 vortices in central bulge (circles), (ii) 5 vortices in central bulge (squares), (iii) 7 vortices in central bulge that are fixed in place plus 2 vortices in coupling elbow with variable spacing (diamonds). Red arrows indicate the intervortex spacing used in Figure 6.3(b).From Nsanzineza & Plourde, Phys. Rev. Lett. 113, 117002(2014) [3].	60

6.5	(Color online) Measured $1/Q_i(B)$ for harmonic, normalized by average of $1/Q_i$ below threshold field (points); simulations of normalized quasiparticle loss on harmonic for different parameters (solid line): (a) $D = 30 \text{ cm}^2/\text{s}$, $\Gamma_R = 20 \mu\text{m}^3/\text{s}$, $\Gamma_v = 7 \times 10^6 \text{ s}^{-1}$; (b) $D = 150 \text{ cm}^2/\text{s}$, $\Gamma_R = 40 \mu\text{m}^3/\text{s}$, $\Gamma_v = 2 \times 10^6 \text{ s}^{-1}$. From Nsanzineza & Plourde, Phys. Rev. Lett. 113, 117002(2014) [3].	61
7.1	Optical photograph of the sample with 6 resonators coupled along same feedline. The sample include two Cu/AlOx/Al junction with Copper traces used to inject Quasiparticles into the ground plane of chip.	64
7.2	Copper-Aluminum oxide-Aluminum junction with overlap area of $5 \times 5 \mu\text{m}^2$	64
7.3	Current-Voltage (I-V) characteristics of Cu/AlOx/Cu junction. The normal state resistance of the junction is $\sim 50 \Omega$, and the superconducting energy gap is $\Delta \sim 200 \mu\text{eV}$. Data was taken at 100 mK.	65
7.4	Resonator internal quality factor measured at different NIS injection powers in zero magnetic field. Insert: Magnitude of complex transmission S_{21} as function of frequency for two different injection powers (power = current \times voltage).	66
7.5	Resonator internal quality factor measured at different NIS injection powers and magnetic fields.	67
7.6	Quasiparticles loss measured at different NIS injection powers and magnetic fields.	68
7.7	Left: Optical image of a chip with a cut in the ground plane of the chip. Right: Zoomed image optical image to aluminum strips that are designed to trap quasiparticles at edge of the ground plane of NIS.	69
7.8	Quasiparticles loss a function of injected quasiparticles in NIS junction ground plane, for various magnetic fields.	70
8.1	Chip wirebonded on a printed circuit board. To minimize unintended spurious transmission modes, we added some interconnections across each resonator and across the feedline.	73
8.2	Plot of resonator internal loss as function of internal power for various magnetic fields.	74
8.3	Plot of vortex loss and change of vortex loss as function of internal power for various magnetic fields.	76
9.1	Copper traps engineered in the middle of the center conductor of resonator.	79
9.2	Internal quality factor of resonator with and without copper traps.	80

List of Tables

6.1	The values of D , Γ_R , Γ_v from the three simulations in figures 6.3 and 6.5	61
-----	---	----

Chapter 1

Introduction

Superconducting resonators with high quality factors are of great interest in many areas including photon detectors for astrophysical applications [4], parametric amplifiers [5, 6], microwave filters [7], and in the field of quantum information science, where microwave resonators play an extremely important role in superconducting qubit design [8], interqubit coupling [9], quantum information storage [10–12] and in the quantum-state dispersive readout [13–16]. Most of the applications of superconducting resonators require that resonators have high quality factors. However, the quality factor of the resonator can be weakened by many dissipation channels including trapped magnetic flux vortices in the device, two-level system fluctuators at the metal-substrate or substrate-air interfaces, energy loss due to coupling to external circuitry, and dissipation due to nonequilibrium quasiparticles.

One other important application of microwave resonators is their use as probes to address the above loss mechanisms that limit the quality factors of the resonator and hence the performance of other devices that couple to these resonators. In fact, because resonators are fabricated using the same materials as filters, amplifiers, or qubits, it is important to understand the fabrication-dependent limits to the device parameters [17–22].

There have been several investigations that have demonstrated that without extensive shielding of stray light, superconducting aluminum circuits measured at millikelvin temperatures can exhibit a significant excess of nonequilibrium quasiparticles leading to significant quasiparticle loss [23–25]. Blackbody photons emitted by warmer regions of the measurement cryostat, even if only at a few Kelvin, can be sufficiently energetic to break Cooper pairs in aluminum films due to the relatively small superconducting energy gap, and this will result in a change of surface impedance of the superconductor.

Understanding the response of trapped flux is important because often microwave components used in low-temperature experiments have strong magnetic fields and magnetic shielding may not be ideal. From the physics point of view, we are interested in the study of the fundamental response of single vortices and the dynamics of quasiparticles in the superconducting microwave resonators. Motivated by previous experiments on quasiparticle lifetime [26], tunnel junction photon detectors [27] and Normal-insulator-superconductor coolers [28] at low temperatures in the presence of a uniform distribution of many vortices, we designed experiments to trap only a single vortex and reduce the density of nonequilibrium quasiparticles in the microwave resonators.

In this thesis we discuss our first experiments to quantify the response of a single vortex in a superconducting coplanar waveguide resonator. We will describe a series of experiments that we have conducted to study the dynamics of vortices and quasiparticles in superconducting microwave resonators. We also made designs to study the resonator response against direct quasiparticle injection.

In Chapter 2 we introduce the fundamental properties of superconductors that form the basis for the topics we cover in this thesis. We will give an introduction to superconductivity and we discuss the characteristic length scales and energy gap of superconductors in the framework of the London theory, Ginzburg-Landau theory, and also BCS theory. We discuss the characteristic parameters of a superconductor and how they influence its electrodynamic response. We introduce the concept of surface impedance of the superconductor and how it is influenced by the motion of vortices and also by the change in the density of quasiparticles.

In chapter 3 we will discuss the fundamental properties of coplanar waveguide resonators (CPW). We introduce lumped-element and distributed resonant circuits and describe the expressions for the impedance, resonance frequency, and quality factor of these circuits. We will also review the current understanding of the loss mechanisms in superconducting coplanar waveguide resonators, and we focus on the loss due to vortices and nonequilibrium quasiparticles.

In Chapter 4 we will first describe the Adiabatic Demagnetization Refrigerator (ADR) and how we use it to reach millikelvin temperatures. We describe our experimental wiring in the ADR cryostat and devices involved in the measurements, such as a cryogenic microwave amplifier, a vector network analyzer (VNA). We also describe how we generate the magnetic field for trapping vortices in the resonators using a Helmholtz coil, as well as our technique for shielding any background fields. We will also discuss the procedure for the design, fabrication, and measurement of our devices.

In Chapter 5 we discuss the experiments we have conducted to trap a single vortex in a superconducting coplanar waveguide resonator. We describe our strategy to trap a few vortices in the CPW resonator and show our field-cooled results where we quantify the loss from just a single vortex.

We show that when vortices are trapped at locations of vanishing local current density, they do not contribute loss and, most importantly, they can act as quasiparticle traps and, as a result of this trapping, the resonator quality factor increases.

In Chapter 6 we discuss numerical simulations of the reduction of the density of nonequilibrium quasiparticles due to trapped vortices. We describe all of the terms in the modified diffusion equation and how we performed our simulations. We will present the results of our simulations for different vortex distributions in the resonator and show that the results from the simulations are consistent with our experimental results.

In Chapter 7 we will discuss our further efforts to understand the dynamics of nonequilibrium quasiparticles in the the superconducting coplanar waveguide resonators. We describe our experiments that we have conducted to study the resonator response under the direct injection density of nonequilibrium quasiparticles using normal metal- insulator-superconductor (NIS) tunnel junctions. We will show that in the presence of trapped vortices, there is a slowing down of the increase of loss due to the increase of loss due to injected nonequilibrium quasiparticles.

In Chapter 8 we will discuss our experiments that we have conducted to study the nonlinearity of vortex dynamics at microwave frequencies with strong driving.

In Chapter 9 we present some ongoing experiments and we conclude our discussion of this thesis.

Chapter 2

Magnetic flux vortices and quasiparticles in superconductors

In this Chapter we describe the fundamental properties of superconductors that we will use throughout this thesis. We will give an introduction to superconductivity, and we discuss the characteristic length scales and energy gap of superconductors in the framework of London theory, Ginzburg-Landau theory, and also the BCS theory. We use the length scales to define the fundamental classes of superconductors, namely type-I and type-II superconductors, and we give conditions at which a superconductor is considered to be in the dirty or clean limits and the expressions for the local and nonlocal response of a superconductor. We discuss the dependence of surface impedance on the applied magnetic field, we also discuss vortex motion and quasiparticle excitations in superconductors.

2.1 Introduction to superconductivity

Superconductivity manifests itself mainly as a resistanceless flow of dc electrical current below some critical temperature. It was discovered in Leiden in 1911 by Heike Kamerlingh Onnes, three years after he first liquefied helium [29]. He performed measurements of the electrical resistance of mercury and noticed a sharp decrease in the resistance near 4.2 K (onset of superconductivity) when mercury was cooled down. The electrical resistivity of normal metals generally decreases with decreasing temperature. For typical metals, the resistivity decreases as the temperature is lowered and lattice vibrations are reduced, but various types of defect scattering limit the resistivity at some non-zero level for arbitrarily low temperatures [30]

2.2 Characteristic parameters of a superconductor

2.2.1 London equations and Meissner-Ochsenfeld effect

In 1933, nearly 22 years after the discovery of superconductivity, Walther Meissner and Robert Ochsenfeld first performed experiments that showed that a superconducting material is different from a perfect conductor [29, 30]. They observed that for temperatures below the critical temperature of the superconducting material, the magnetic flux density is zero inside the superconducting material, independent of whether the superconductor was cooled in zero or nonzero magnetic field. This is known as the Meissner-Ochsenfeld Effect or just simply the Meissner effect. The complete exclusion of magnetic flux means that a superconducting material is a perfect diamagnet. Therefore, perfect diamagnetism and zero dc resistivity are basic properties of the superconducting state.

In order to explain the Meissner effect and zero resistivity, the two brothers Fritz and Heinz London proposed the following two phenomenological equations relating currents with electric and magnetic fields in a superconductor [29, 31]

$$\mathbf{E} = \frac{\partial}{\partial t} \left(\frac{m}{n_s e^2} \mathbf{J} \right) \quad (2.1)$$

and

$$\mathbf{B} = -\nabla \times \left(\frac{m}{n_s e^2} \mathbf{J} \right). \quad (2.2)$$

In the two London equations 2.1 and 2.2, \mathbf{J} is the screening current density. It includes the normal current obeying Ohm's law, the Maxwell's displacement current, and the supercurrent. In a superconductor, the normal current and the Maxwell's displacement current are negligible for slowly changing fields, but are important for rapidly changing fields [31]. Equation 2.2 leads to

$$\nabla^2 \mathbf{h} = \frac{1}{\lambda_L^2} \mathbf{h}. \quad (2.3)$$

For a semi-infinite slab with its surface at $x = 0$, the applied magnetic field $h(0)$ falls in its interior as [31]

$$h(x) = h(0)e^{-x/\lambda_L}. \quad (2.4)$$

For $x \gg \lambda$, $H(x) = 0$ in accordance with the Meissner-Ochsenfeld effect. Therefore, in stationary conditions, a superconductor cannot sustain a magnetic field in its interior, but only within a narrow surface layer. The magnetic field decays to $1/e$ of its value over a distance equal to λ_L , called the London penetration depth [31]

$$\lambda_L = \left(\frac{m}{\mu_0 n_s e^{*2}} \right)^{\frac{1}{2}}, \quad (2.5)$$

where n_s is the density of superelectrons. The superelectrons carry a double electronic charge equal to $e^* = 2e$. The penetration depth varies with temperature approximately as [29] $\lambda_L(T) =$

$\lambda_L(0) (1 - (T/T_c)^4)^{1/2}$. $\lambda_L(0)$ is the penetration depth at zero temperature, and it is given by equation 2.5.

2.2.2 Coherence concept and Pippard's non-local modification of the London theory

The magnetic penetration depth in superconductors predicted by the London equations was found to be smaller than the values measured for pure superconductors [29]. In 1950, Pippard introduced the concept of coherence of the superconducting state and provided a generalization of the London theory by taking into account the effect of the electronic mean free path l . According to Pippard [31], if the local electronic state is characterized by an order parameter ψ , any perturbation in ψ will spread out over a distance ξ , called the coherence length, from the center of disturbance. Thus, the coherence length ξ in the presence of scattering is related to the electronic mean free path l as [29]

$$\frac{1}{\xi} = \frac{1}{\xi_0} + \frac{1}{l}, \quad (2.6)$$

where ξ_0 is the coherence length for pure material.

2.2.3 Ginzburg-Landau theory

The Ginzburg-Landau (G-L) theory is a phenomenological treatment of the superconducting phase transition, it is only valid near the critical temperature T_c . G-L theory considers that the free energy of a superconductor in the vicinity of T_c can be described by a complex order parameter ψ [29] such that $|\psi|^2 = n_s$, where n_s is the local density of superelectrons. The Ginzburg-Landau free energy density f_{sh} in the presence of an applied magnetic field h is given by [29]

$$f_{sh} = f_{s0}(T, \psi) + \frac{\hbar^2}{8\pi} + \frac{1}{2m} \left| -i\hbar\nabla\psi - \frac{e^*}{c}\mathbf{A} \right|^2, \quad (2.7)$$

where $f_{s0}(T, \psi)$ is the free energy in the absence of magnetic field. It is given by

$$f_{s0}(T, \psi) = f_n(T) + \alpha(T) |\psi|^2 + \frac{1}{2} \beta(T) |\psi|^4. \quad (2.8)$$

$\alpha(T)$ and $\beta(T)$ are temperature dependent coefficients. At $T = T_c$, $\alpha(T)_c = 0$ and $\beta(T)_c > 0$. But for $T < T_c$, $\alpha(T)_c < 0$ and $\beta(T)_c > 0$. The idea is to minimize the equation 2.7 with respect to ψ and \mathbf{A} over the all volume of the superconducting material. The main results of the derivation are the Ginzburg-Landau penetration depth and coherence length, given by

$$\lambda = \left(\frac{m}{4\mu_0 e^{*2} \psi_0^2} \right)^{\frac{1}{2}} \quad (2.9)$$

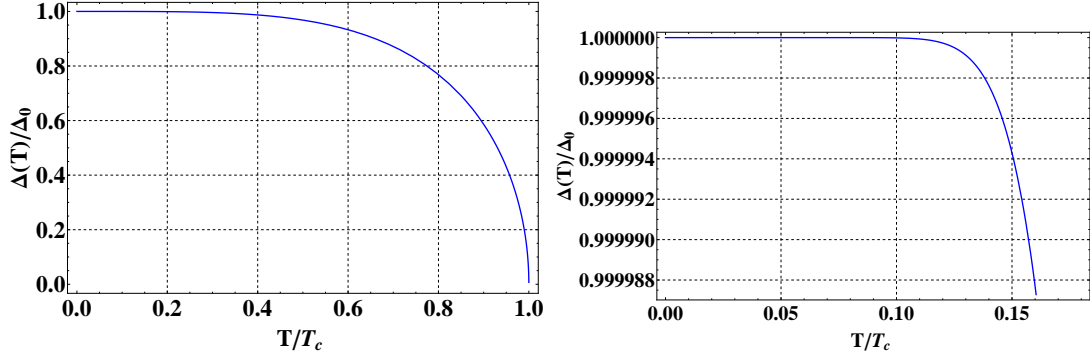


Figure 2.1: Variation of superconducting energy gap with temperature. Right: plot using Eq. (2.12) for high temperature approximation and Left: plot using Eq. (2.14) for low temperature approximation.

and

$$\xi = \left(\frac{\hbar^2}{4m|\alpha|} \right)^{\frac{1}{2}}. \quad (2.10)$$

The ratio of London penetration depth and the coherence length is called Ginzburg-Landau parameter κ_{GL} , Thus,

$$\kappa_{GL} = \frac{\lambda}{\xi}. \quad (2.11)$$

2.2.4 BCS theory and the energy gap Δ

The G-L theory, like the London theory, could not answer to the fundamental question of why a superconductor behaves according to the London equations. In other words, G-L and London theory could not explain what are superelectrons whose behavior they were intended to describe. This question was finally resolved in 1957 by the tremendous work by J. Bardeen, L. N. Cooper and J. R. Schrieffer [32]. After the discovery of the isotope effect, it became clear that the vibrations of the lattice of ions of a metal play a critical role in creating the superconducting state. What the BCS theory considered is that the interaction between electrons and quantized excitations of the crystal lattice, phonons, can lead to an attractive electron-electron attraction and hence to the formation of Cooper pairs with zero total spin [33]. The Cooper pairs are able to condense into a ground state with macroscopic phase coherence. All Cooper pairs in the condensate have same wave function that depends on single spatial coordinate. The condensate can move through the material with no dissipation. The key feature of the BCS theory is the prediction that there is an energy gap of $\pm\Delta$ about the Fermi energy. The energy gap is a function of temperature, and at high temperature it is written as

$$\Delta(T) = \Delta_0 \left[1 - \left(\frac{T}{T_c} \right)^4 \right]^{\frac{1}{2}}, \quad (2.12)$$

where Δ_0 is the superconducting energy gap at zero temperature, that is the value of the superconducting energy gap with no quasiparticles and for a weak-coupling superconductor, it is given by [29]

$$\Delta_0 = 1.76k_B T_c, \quad (2.13)$$

where k_B is the Boltzmann constant, and T_c is the transition temperature of the superconductor. For temperatures well below T_c , the superconducting energy gap varies slowly with temperature, and the approximate expression for energy gap at low temperature is [34]

$$\Delta(T) \cong \Delta_0 \exp \left[-\frac{2\pi k_B T}{\Delta_0} \exp \left(-\frac{\Delta_0}{k_B T} \right) \right]. \quad (2.14)$$

The superconducting energy gap Δ_0 is related to the coherence length ξ_0 as follows [29]

$$\xi_0 = \frac{\hbar v_F}{\pi \Delta_0}, \quad (2.15)$$

where v_F is the fermi velocity of the condensate. The density n_{qp} of the single-particle excitations (quasiparticles) at an energy $|E| > \Delta$ with respect to the Fermi level is given by [35, 36]

$$n_{qp} = 4N(0) \int_{\Delta}^{\infty} \rho(E) f(E) dE, \quad (2.16)$$

where $N(0)$ is the single-spin density of electron states at the Fermi energy, for aluminum film it is $N(0) = 6.9 \times 10^{28} \text{ J}^{-1} \mu\text{m}^{-3}$ [37]. $\rho(E) = \frac{E}{\sqrt{E^2 - \Delta^2}}$ is the normalized density of the quasiparticles states. For $0 \leq |E| < \Delta$, $\rho(E) = 0$, that is, the quasiparticle density of states is zero for energies lower than gap energy. Note that these energies are measured with respect to the Fermi energy E_F . $f(E)$ is the Fermi-Dirac distribution function.

2.2.5 Limiting cases for the electrodynamic response

The coherence length ξ , the penetration depth λ , the mean-free path l are very fundamental parameters that characterize a superconductor and defines its electrodynamic behavior. In fact, for clean superconductors, $\xi_0 \ll l$, in which case we have $\xi_0 = \xi$ by using the equation 2.6. In contrast, dirty superconductors have the mean free path that is much smaller than the coherence length, $\xi_0 \gg l$ [34].

According to Gao [34] and Zmuidzinas et al. [35], the extreme anomalous limit occurs when the response of the superconductor is no longer local because the mean free path l is long compared to the distance over which the field varies significantly. That means, in this limit, the effective

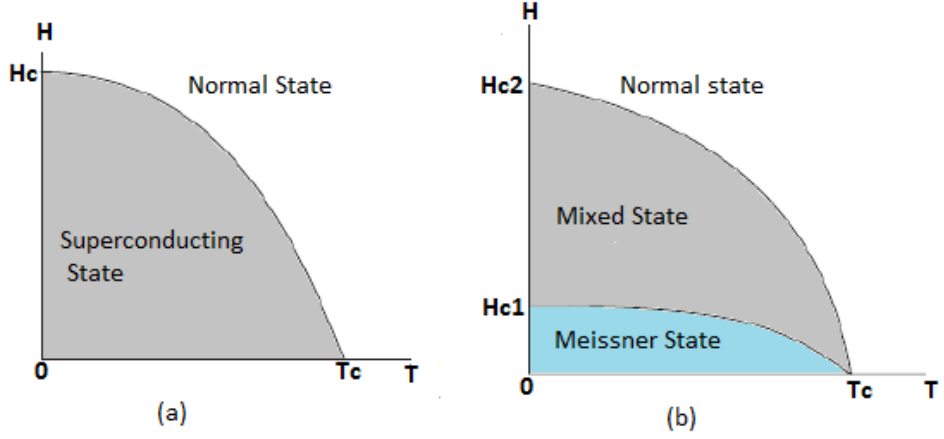


Figure 2.2: A schematic illustrating the H-T diagrams of (a) Type-I and (b) Type-II superconductors.

penetration depth length λ is smaller than the mean free path l or the coherence length ξ_0 . The penetration depth is given by $\lambda_{\text{eff}} = 0.65(\lambda\xi_0)^{1/3}$

The local limit occurs when the effective penetration depth λ_{eff} is much longer than the coherence length and the mean free path [34, 35, 38], in local limit the effective penetration depth is given by $\lambda_{\text{eff}} = \lambda_L (1 + \xi_0/l)^{1/2}$ for dirty superconductors and $\lambda_{\text{eff}} = \lambda_L$ for clean superconductors.

For the case of a thin film, the penetration depth is smaller than the film thickness, $d < \lambda$. In this case the thickness d plays a role. In fact, for thin films the screening currents are simply spread out over larger distances. For applied magnetic field perpendicular to the thin film, the penetration depth is given by [2] $\lambda_{\perp} = 2\lambda^2/d$. For a thin film in the dirty limit, the effective penetration depth and coherence length can be calculated from the following expressions [39]

$$\lambda_{\text{eff}} = 1.05 \times 10^{-3} \times \left(\frac{\rho}{T_c}\right)^{1/2} \quad (2.17)$$

and

$$\xi_{\text{eff}} = 1.81 \times 10^{-8} \times (T_c \times S)^{-1/2}, \quad (2.18)$$

where S is the slope that can be obtained from the $T_c - B$ plots. ρ is the low temperature resistivity of the superconducting material.

2.3 Type-I and Type-II superconductors

The ratio of λ and ξ determines the energy for forming a domain wall between a superconducting and normal region. This ratio $\kappa = \lambda/\xi$ is called the Ginzburg-Landau parameter and gives us a

crossover between two fundamental superconducting classes, namely type-I ($\kappa < 1/\sqrt{2}$) and type-II ($\kappa > 1/\sqrt{2}$) superconductors [40].

Type-I superconductors, also known as Pippard superconductors, have one critical field which is the same as thermodynamic critical field H_c . Below the critical magnetic field H_c and at temperatures $T < T_c$, type-I superconductors with no demagnetizing effects show a complete Meissner effect and zero resistance. The phase transition for type-I superconductor to normal state is of first order.

Type-II superconductors have two critical fields, a lower critical field H_{c1} and an upper critical field, H_{c2} . In the applied magnetic range $0 < H < H_{c1}$ and in the absence of demagnetizing effects, the magnetic flux is completely expelled and the Meissner effect is complete. The magnetic field penetration in the form of vortices sets in at H_{c1} . Each flux vortex carries a single flux quantum given by

$$\Phi_0 = \frac{hc}{2e} = 20.7 \text{ G} - \mu\text{m}^2. \quad (2.19)$$

In the field range $H_{c1} < H < H_{c2}$, the type-II superconductor resides in the mixed state and is no longer a perfect diamagnetic material, that is, the magnetic field can penetrate the superconductor, but not completely. All magnetic flux threading the superconductor in the mixed state is carried by the Abrikosov vortices, which means the magnetic flux density can be written as $B = n_v \Phi_0$, where n_v is the number of vortices per unit area. The superconducting order parameter is reduced to zero in the core of a vortex over a length scale of ξ ; this core then contains bound quasiparticle states that cause the core to behave effectively like a cylindrical normal metal region of radius ξ [29]. The magnetic flux extends out beyond the core as over a distance of order of penetration depth λ . The magnetic field at the center of vortex is given by [41]

$$h(0) \approx \frac{\Phi_0}{2\pi\lambda^2} \ln \kappa. \quad (2.20)$$

As the field is increased, the density of vortices increases also and at H_{c2} , the normal cores of vortices overlap and as a consequence, the order parameter goes continuously to zero [42] and in the end, the superconductivity is destroyed and the material goes into the normal state. The phase transition from the vortex state to the normal state is of second order.

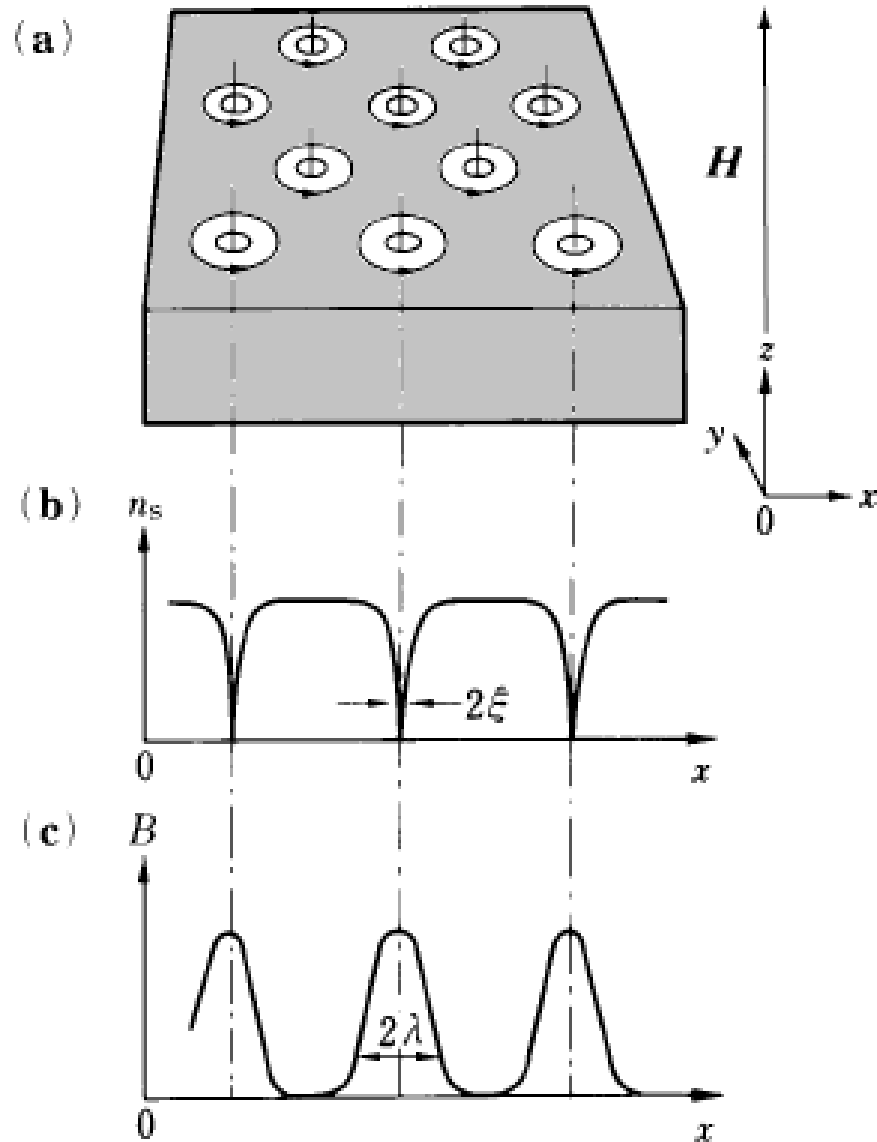


Figure 2.3: Schematic representation of (a) magnetic field penetration of a type-II superconductor. The vortex is surrounded by screening currents. (b) The vortex represents a singularity in the order parameter. (c) The maximum field is at the center of vortex. From reference [1].

Transition from type-I to type-II in thin films: Critical thickness d_c

Below some critical thickness, thin films of a bulk type-I superconductor in a perpendicular magnetic field can behave like a type-II superconductor, in that they develop a vortex lattice in which each vortex carries a single-flux quantum [43–48]. Tinkham [49] was the first to point out that films

of type-I superconductors with a thickness less than a critical thickness assume an Abrikosov vortex state in a perpendicular magnetic field, the same as the mixed state of type-II superconductors. Tinkham's theory was motivated by experimental results that very thin film of type-I superconductors show a second order phase transition in a perpendicular magnetic field [40, 44, 50, 51]. Several experiments have been carried out with thin films of Pb, Sn, In, and Al, and established the single-quantum nature of the individual flux spots [52–57]. In the framework of G-L theory, the fluxoid structure in superconducting films in the presence of a magnetic field has been studied in more detail [58–61]. The main result is the derivation of the critical film thickness d_c below which the Abrikosov vortex lattice is energetically stable and the phase transition in perpendicular magnetic field is of second order. The critical thickness is given by [40, 55–57, 62, 63]

$$d_c \approx \frac{C\delta}{4(1 - \sqrt{2}\kappa^2)}, \quad (2.21)$$

where C is a constant varying between 3.5 and 9 [51]. δ is the surface-energy parameter in the Landau domain theory, it is related to penetration depth as $\delta/\lambda \approx 1.13 - 1.6$, with $0.1 < \kappa < 1.0$ [64]. For aluminum, d_c was found in the range $1.8 - 2.0 \mu\text{m}$ for $T/T_c = 0.8 - 0.96$ [40, 51].

2.4 Threshold field for trapping vortices

In geometries with large demagnetizing factors like a thin Superconducting sheet in a perpendicular field, the screening currents are spread out over large distances so that the threshold field B_{th} for establishing vortices can be lower than H_{c1} . The relationship between the width of a superconducting strip and the value of B_{th} has been studied in references [2, 65] with field-cooling followed by imaging of the vortex distributions. Stan [2] performed scanning Hall probe microscopy experiments to study vortex nucleation in narrow-thin film superconducting strips and established that the first flux penetration into the strip occurs when the vortex is absolutely stable in the center of the strip, and this happens when the Gibbs free energy is zero in the middle of the strip. His results were in reasonable agreement with theoretical predictions of Likharev and Clem, that the Gibbs free energy $G(W/2)$ at the middle of the superconducting strips of width W is [2]

$$G(W/2) = \left(\frac{\Phi_0^2}{8\pi^2\lambda} \right) \ln \left(\frac{2W}{\pi\xi} \right) \left[1 - \frac{B}{B_{th}} \right]. \quad (2.22)$$

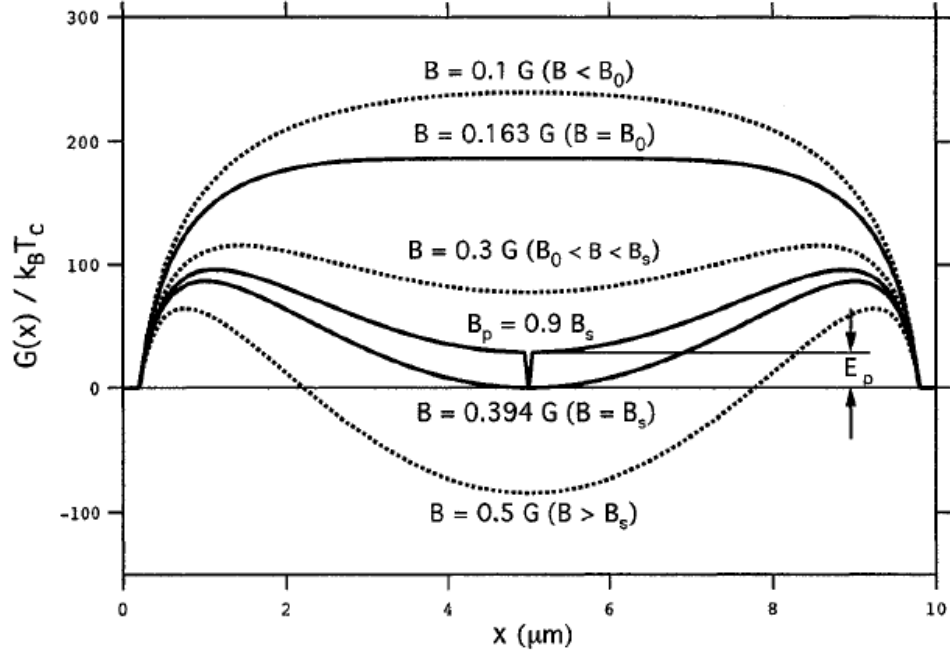


Figure 2.4: Gibbs free energy as a function of the applied magnetic field. The Gibbs free energy has its first minimum at the magnetic field B_0 . With pinning defects, vortices penetrate the superconductor at lower field B_p than the threshold field B_s when no pinning. From Stan et al. 2004 [2].

The extracted values of B_{th} for strips of different width W were found to be in reasonable agreement with the expression

$$B_{th} = \frac{2\Phi_0}{\pi W^2} \ln\left(\frac{\alpha W}{\xi}\right), \quad (2.23)$$

where $\Phi_0 \equiv h/2e$ is the superconducting flux quantum and ξ is the coherence length at the temperature at which the vortices freeze into their respective pinning sites, and $\alpha = 2/\pi$ in the Clem model and $\alpha = 1/4$ in the Likharev model [2]. The above expression pertains to field-cooling, therefore the process for vortex entry into a zero-field cooled state is rather different. Because we will present field-cooled experiments in chapters 5 and 6, the following discussion will be the focus in the two chapters. In reference [3], we have extracted values of B_{th} for $w = 3, 6, 8 \mu\text{m}$ for the three characteristic widths in the different regions of our resonator and we plot these values in figure 2.5. Because this is a rather narrow range of W to compare with Equation 2.23, we have chosen to include some previously unpublished B_{th} data from our lab on some other aluminum resonators with a different geometry, but a wider range of linewidths. This other chip contained four quarter-wave coplanar waveguide resonators with uniform-width center conductors, similar to the device in reference [66], with widths $W = 10, 12, 18, 26 \mu\text{m}$. Also, the thickness of the aluminum film on this other chip was 150 nm.

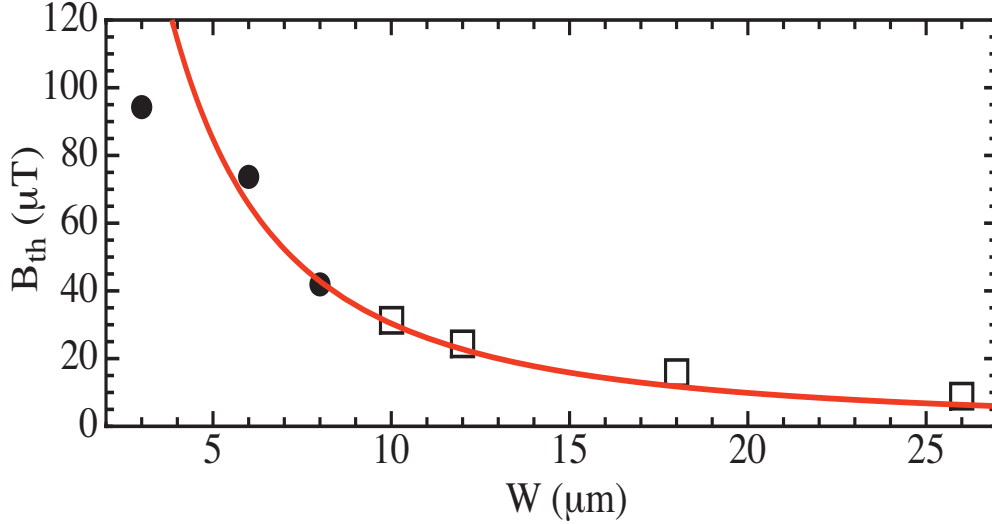


Figure 2.5: Plot of threshold cooling fields B_{th} for different width segments on resonator from [3] (filled circles) and $B_{th}(W)$ values for quarter-wave uniform-width resonators from separate device as discussed in text (open squares). Curve corresponds to Eq. (2.23) for $\xi = 235$ nm.

We have extracted B_{th} for the four resonators of different widths and we include this data in Figure 2.5 with the $B_{th}(W)$ points extracted from the measurements in [3]. We then include a curve corresponding to Equation 2.23 by adjusting ξ . We find that for $\xi = 235$ nm, we obtained reasonable agreement with the measured $B_{th}(w)$ points, although the curve is not a perfect match to the data. Differences between the measurements and the predicted dependence of equation 2.23 could be due to the variations in the details of the vortex freezing process between the strips of different widths. Also, for some of our features, such as the $6 \mu\text{m}$ and $8 \mu\text{m}$ regions of our resonator, the finite length of these regions may change the details of Equation 2.23 as well. Nonetheless, the general trend of B_{th} is clear and vortices trap at higher threshold fields for narrower superconducting traces.

2.5 Vortex motion in superconductors

In a field-cooled process, the application of a perpendicular magnetic field that is greater than the threshold field B_{th} for trapping vortices introduces vortices into a type-II superconductor. Vortices can move under the influence of a Lorentz force that could come from external currents or from screening currents due to an external magnetic field [42, 64]. The Lorentz force acting on a single vortex is related to the current density as [29]

$$\mathbf{f}_L = \mathbf{J} \times \Phi_0. \quad (2.24)$$

The motion of the vortices will induce an electric field \mathbf{E} according to Faraday's law, and the induced electric field is related to the vortex velocity \mathbf{v} as

$$\mathbf{E} = (\mathbf{B} - \mathbf{B}_{th}) \times \mathbf{v}, \quad (2.25)$$

where B is the magnetic flux density, and is given by $(B - B_{th}) = n_v \Phi_0$, B_{th} , given by equation 2.23, is the threshold field above which vortices penetrate into the superconducting film. Hence the motion of vortices induce a resistive voltage and some power is dissipated. Assuming that there is no pinning, the motion of vortices is retarded only by viscous force $f_v = \eta v$. A free-flux-flow (FFF) of vortices is characterized by a balance between the Lorentz force $j\Phi_0$, where J is the current density, and the viscous force ηv giving rise to the flux flow resistivity given by

$$\rho_f = \frac{E}{J} = \frac{(B - B_{th})v}{J} = (B - B_{th}) \frac{\Phi_0}{\eta} = n_v \frac{\Phi_0^2}{\eta}. \quad (2.26)$$

Hence, the flux flow resistivity is proportional to the magnetic flux density, and therefore, to the number of vortices per unit area. Thus, free-flux-flow consists of purely viscous motion of the vortices in which the pinning effect on the vortices is negligible [67]. Recall that the vortex core contains non-superconducting single-particle excitations, which leads to the vortex viscosity.

If a superconductor has pinning defects, which are often regions of weakened superconductivity and that form a region where a vortex core can sit and lower the overall system free energy [41], vortices will be pinned by these defects and they cannot move. The current flow in the superconductor with vortices pinned by defects will result in vanishing resistance, which could be from crystalline structure such as impurities or grain boundaries or they could be artificial pinning centers such as holes (antidots), magnetic dots, arrays of dots or slots.

Vortices may become unpinned by a sufficient driving force produced by transport current and the screening currents due to an external magnetic field and their motion also is subject to a damping force which gives rise to dissipation as explained above. The dissipation associated with a moving vortex is parameterized by a vortex viscosity η given by [68]

$$\eta(v) = \frac{\eta(0)}{1 + (v/v^*)^2}, \quad (2.27)$$

where $\eta(0)$ is the viscous damping coefficient at zero vortex velocity. v^* is the critical vortex velocity at which the non-linear effects occurs as we will explain in detail in chapter 8.

The high-frequency ac currents lead to oscillatory motion of vortices about their equilibrium positions in pinning sites. The vortex mass is small enough that for most materials it can be neglected at microwave frequencies [69]. Assuming a harmonic form for pinning potentials characterized by a spring constant, we write the simple equation of motion of a single vortex in a superconducting

material as [70]

$$\eta v + k_p x = j \Phi_0. \quad (2.28)$$

In equation 2.28, j is the applied oscillatory current density at frequency ω , k_p is the restoring force constant of a pinning potential and η is the vortex viscosity coefficient. The ratio k_p/η of restoring force constant and vortex viscosity defines the depinning frequency [66]. Thus, [70]

$$\omega_p = \frac{k_p}{\eta}. \quad (2.29)$$

For frequencies $\omega \ll \omega_p$ the vortex response is mostly elastic and pinning will dominate. In contrast, for high frequencies $\omega \gg \omega_p$, the vortex response is increasingly dissipative as the vortex viscosity is more important.

At high frequencies $\omega \gg \omega_p$, the dissipation caused by the motion of vortices is reflected in the change the surface impedance of the superconductor [71]. In fact, the surface impedance Z_s of the superconductor is defined as

$$Z_s = R_s + iX_s, \quad (2.30)$$

where R_s is the surface resistance and X_s is the surface reactance. The surface impedance is related to the complex resistivity by the following expression [72]

$$Z_s = \sqrt{i\omega\mu_0(\rho_1 + i\rho_2)}. \quad (2.31)$$

The vortex resistivity ρ_v can be used to model the surface impedance for a superconductor containing vortices. Various models have been proposed to derive the vortex complex resistivity $\tilde{\rho}_v$. In fact, Gittleman and Rosenblum [73] considered the simple vortex equation 2.28, including pinning only. The model was extended by Coffey and Clem [74] and then extended further by Brandt [75] to include flux creep effects due to different thermal effects. In 2008, motivated by the various treatments of the complex vortex resistivity, Pompeo and Silva showed that all of the previous models can be described by the following expression [76]

$$\frac{\tilde{\rho}_v(\omega)}{\rho_f} = \frac{\epsilon + i\omega/\omega_p}{1 + \omega/\omega_p}, \quad (2.32)$$

where ρ_f is the flux flow resistivity given by equation 2.26, ω is the microwave angular frequency, ϵ is the flux creep factor and ω_p is given by equation 2.29. The solution to equation 2.32 has a real (dissipative) and the imaginary (reactive).

2.6 Thermal and nonequilibrium quasiparticles

2.6.1 Mattis-Bardeen equations for thermal quasiparticles

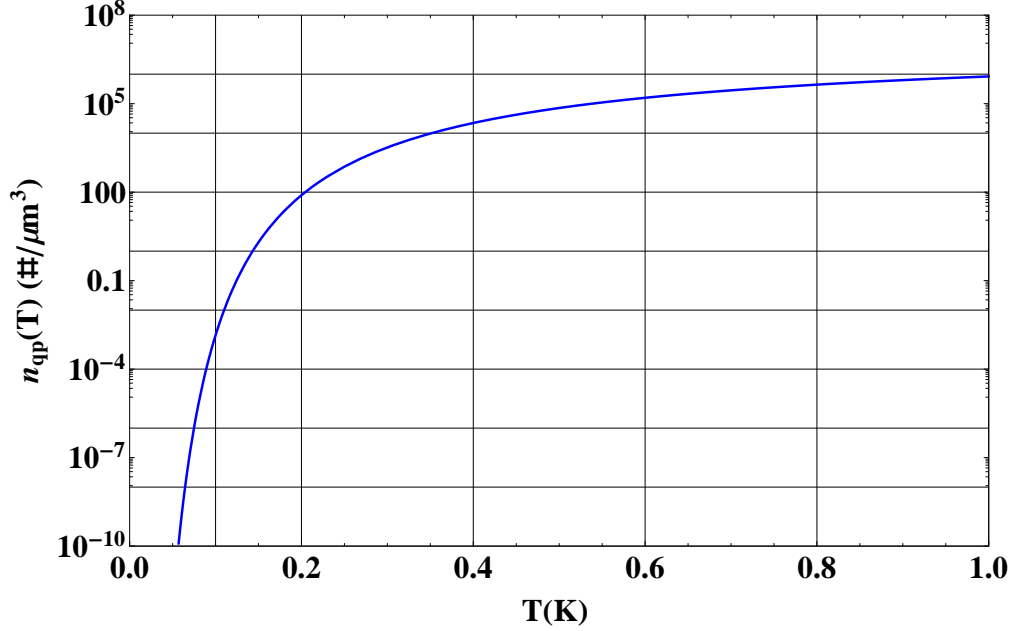


Figure 2.6: Variation of thermal quasiparticles with temperature for $T_c = 1.2$ K. Calculations based on Eq. 2.33.

A phonon with energy greater than 2Δ can break a Cooper pair, and generate two single-particle excitations, called quasiparticles. When two quasiparticles recombine into a Cooper pair, a 2Δ phonon is emitted. Therefore, in equilibrium, the state of a superconductor is formed by the Cooper pairs with a density n_{cp} and thermally excited quasiparticles with a density n_{qp} [77]. The quasiparticle density and recombination time as a function of temperature have been calculated in reference [36, 37, 78] and given by

$$n_{qp} = 2N(0) (2\pi k_B T \Delta)^{\frac{1}{2}} \exp\left(-\frac{\Delta}{k_B T}\right) \quad (2.33)$$

and

$$\tau_{qp} = \frac{\tau_0}{\sqrt{\pi}} \left(\frac{k_B T_c}{2\Delta}\right)^{5/2} \left(\frac{T_c}{T}\right)^{1/2} e^{\Delta/k_B T}. \quad (2.34)$$

Recall that $N(0)$ is the single-spin density of electron states at the Fermi energy. $N(0) = 6.9 \times 10^{28} J^{-1} \mu\text{m}^{-3}$ for aluminum film [37]. τ_0 is a material specific parameter, it describes the strength of the electron-phonon coupling [37]. Therefore, in thermal equilibrium, the quasiparticle density n_{qp} in a superconductor follows an exponential temperature dependence while the quasiparticle lifetime τ_{qp} has an inverse temperature dependence. As the temperature decreases, the quasiparticle recombination time τ increases exponentially because of the reduced density of quasiparticles. The

electrodyanamic behavior of a superconductor is often expressed in terms of its complex conductivity, defined as

$$\sigma(\omega) = \sigma_1(\omega) - i\sigma_2(\omega). \quad (2.35)$$

The real part σ_1 denotes the conductivity by quasiparticles and the imaginary part σ_2 is due to the superconducting condensate. Using BCS theory, Mattis and Bardeen derived the expression for the real σ_1 and imaginary part of the complex conductivity σ_2 relative to the normal conductivity σ_n .

The Mattis-Bardeen equations reads [34, 35, 39]

$$\frac{\sigma_1(\omega, T)}{\sigma_n} = \frac{4\Delta_0}{\hbar\omega} \exp\left(-\frac{\Delta_0}{k_B T}\right) \sinh\left(\frac{\hbar\omega}{2k_B T}\right) K_0\left(\frac{\hbar\omega}{2k_B T}\right) \quad (2.36)$$

$$\frac{\sigma_2(\omega, T)}{\sigma_n} = \frac{\pi\Delta_0}{\hbar\omega} \left[1 - \sqrt{\frac{2\pi k_B T}{\Delta_0}} \exp\left(-\frac{\Delta_0}{k_B T}\right) - 2e^{-\Delta_0/k_B T} e^{-\frac{\hbar\omega}{2k_B T}} I_0\left(\frac{\hbar\omega}{2k_B T}\right) \right], \quad (2.37)$$

where K_0 and I_0 are the modified Bessel functions of the first and second kind. Therefore, comparing equations 2.33, 2.36 and 2.37, we find that as $T \rightarrow 0$, σ_1 and n_{qp} vanish. However, the imaginary part of the conductivity, associated with the inertia of the superconducting electrons, remains nonzero, $\sigma_2(\omega, 0)/\sigma_n \approx \pi\Delta_0/\hbar\omega$. Thus, at low temperature $T \ll T_c$ the dissipative response of the quasiparticle system is very small compared to the reactive response of the cooper pairs. Furthermore, $\sigma_1(\omega, T) \propto n_{qp}(T)$ and $\sigma_2(\omega, T) - \sigma_2(\omega, 0) = \delta\sigma_2(\omega, T) \propto n_{qp}(T)$. The surface impedance in equation 2.30 can be expressed in terms of the complex conductivity $\sigma(\omega, T)$ as [35]

$$Z_s(\omega, T) = Z_s(\omega, 0) \left(1 + i \frac{\delta\sigma(\omega, T)}{\sigma(\omega, 0)} \right)^\gamma, \quad (2.38)$$

where $Z_s(\omega, 0)$ is the surface impedance of the superconductor at zero temperature. $\gamma = 1, -1/2, -1/3$ for the thin film limit, local limit, and extreme anomalous limit, respectively.

2.6.2 Nonequilibrium quasiparticles at millikelvin temperatures

Several experiments have reported that at millikelvin temperatures, there is a deviation from an exponential temperature dependence for quasiparticles density [77]. At low temperatures below roughly one tenth of the critical temperature T_c , various experiments have observed the quasiparticle density to become independent of temperature and saturate at a value that is orders of magnitude above the predicted thermal level[25, 79, 80]. Quasiparticles could be generated by various sources of pair-breaking radiation, including stray infrared light, cosmic rays or energy relaxation in the superconducting material [36, 81]. Motivated by the Rothwarf-Taylor coupled differential. equations for the quasiparticle density and phonon density [82], Barends [23] proposed a simple model to take into account the nonequilibrium quasiparticles, the rate equation for total number of quasiparticles

$$\frac{\delta N_{qp}}{\delta t} = \frac{P}{\Delta} + G - \Gamma_R N_{qp}^2, \quad (2.39)$$

where P is the power absorbed for which $hf > 2\Delta$, G is the standard thermal generation term due to pair breaking by phonons, and Γ_R is a material-dependent recombination constant given by [37]

$$\Gamma_R = 2 \left(\frac{\Delta}{k_B T_c} \right)^3 \frac{1}{N(0)\Delta\tau_0}. \quad (2.40)$$

Without P/Δ term, equation 2.39 reduces to equation 2.33. n_{qp} become proportional to P/Δ when the quasiparticle density exceeds that of the thermal quasiparticles.

Chapter 3

Coplanar waveguide resonators

Superconducting coplanar microwave guide resonators with high quality factors are of great interest in many areas including photon detectors for astrophysical applications [4], parametric amplifiers [5, 6], microwave filters [7], and in the field of quantum information science where microwave resonators play an extremely important role in superconducting qubit design [8], interqubit coupling [9], quantum information storage [10–12] and in the quantum-state dispersive readout [13–16]. The other very important application of microwave resonators is their use as sensitive probes to study the loss mechanisms that limit the quality factors of the resonator. In fact, because resonators are fabricated using the same materials as filters, amplifiers, or qubits, it's important to understand the fabrication-dependent limits to device parameters [17–22]. In this chapter we give a survey on lumped- and distributed-element resonators and we discuss key design parameters of a coplanar waveguide resonator. Then we discuss the current understanding of the various loss mechanisms in coplanar waveguide resonators.

3.1 Lumped-elements resonators circuits

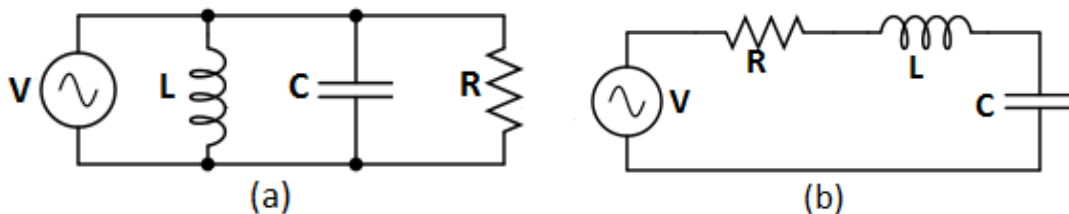


Figure 3.1: Lumped elements in (a) parallel and (b) series resonant circuits.

In this section we describe parallel and series lumped-elements resonator circuits. We describe the input impedance, resonance frequency and quality factor of these circuits. Our discussion will follow the analysis of [83].

Parallel RLC Resonator

The input impedance of a parallel RLC resonant circuit in figure 3.1(a) is given by

$$Z_{\text{in}} = \left(\frac{1}{R} + \frac{1}{j\omega L} + j\omega C \right)^{-1}. \quad (3.1)$$

At resonance, Z_{in} is minimum and, the resonance frequency ω_0 is defined as

$$\omega_0 = \frac{1}{\sqrt{LC}}. \quad (3.2)$$

The unloaded quality factor Q of the parallel resonant circuit, in the absence of loading effects caused by external circuitry, is defined as

$$Q = \omega \frac{\text{average energy stored}}{\text{energy loss per unit of time}}. \quad (3.3)$$

Thus, the quality factor of a parallel resonant circuit is

$$Q = \omega_0 RC = \frac{R}{\omega_0 L}. \quad (3.4)$$

Series RLC Resonator

The resonance frequency ω_0 of a series RLC is also given by

$$\omega_0 = \frac{1}{\sqrt{LC}}. \quad (3.5)$$

The unloaded quality factor Q of the series resonant circuit is

$$Q = \frac{\omega_0 L}{R} = \frac{1}{\omega_0 RC}. \quad (3.6)$$

3.2 Distributed transmission-line resonators

The values of quality factors obtained using lumped elements are small. It is also difficult to achieve lumped element resonant circuits with high frequencies as this requires small capacitors and inductors. These limitations are resolved using distributed transmission lines resonators which can be built to achieve quality factor of hundreds of thousands, and can be used at microwave frequencies. We describe half-wave and quarter-wave transmission line resonators following the analysis of Pozar [83].

The distributed resonant circuit utilizes open or shorted transmission line. As the resonance occurs in the form of standing waves, its dimensions are comparable with the wavelength, λ . Therefore, any form of transmission line of suitable length can be used to form a resonator.

3.2.1 Coplanar waveguide geometry: Half-wave and Quarter-wave resonators

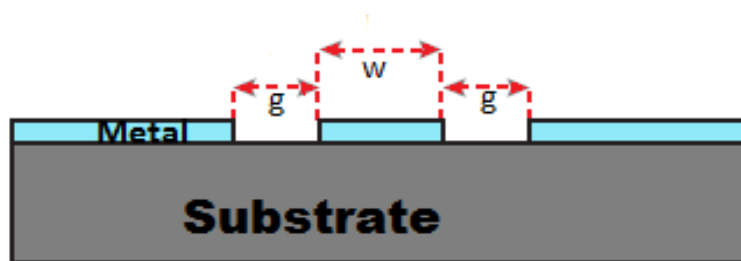


Figure 3.2: Geometry of the CPW transmission line.

CPW geometry is most appropriate for Superconducting thin-film devices fabricated on dielectric substrates. The coplanar waveguide (CPW) geometry has all of the metal traces only on the top surface of a dielectric substrate. It has a center conductor of width w and the ground planes on either side. The gap g separates the ground planes and the center conductor. The dimensions of the center strip, the gap, and the thickness and permittivity of the dielectric substrate determine the effective dielectric constant ϵ_{eff} , characteristic impedance Z_0 , and internal losses (which could be dielectric loss, metal loss, radiation loss, coupling loss, etc.).

The voltage and current on a transmission line are discussed in details in Pozar [83]. We review the main results relevant to our discussions in the next chapters. In fact, the total voltage and current on a transmission line are given by

$$V(z) = V_I [e^{-\gamma z} + \Gamma e^{\gamma z}], \quad (3.7)$$

and

$$I(z) = \frac{V_I}{Z_0} [e^{-\gamma z} - \Gamma e^{\gamma z}], \quad (3.8)$$

where we assumed the transmission is along the z -axis, V_I is the voltage amplitude of the incident wave referenced at $z = 0$, $\Gamma = (Z_L - Z_0)/(Z_L + Z_0)$ is the reflection coefficient of the load, with Z_L is the impedance of the load, and Z_0 is the characteristic impedance of the transmission line. $\gamma = \alpha + i\beta$ is the complex propagation constant, with α the attenuation constant and β is the phase constant or wave number. Applied to a half-wave resonator which has both ends open, the

equations 3.7 and 3.8 are given by $V(z) = 2V_I \cos(\beta z)$ and $I(z) = (-2iV_I/Z_0) \sin(\beta z)$. For a quarter-wave resonator that has one end open and the opposite end shorted to ground, the expressions for voltage and current are $V(z) = -2iV_I \sin(\beta z)$ and $I(z) = (2V_I/Z_0) \cos(\beta z)$ [83]

The characteristic impedance of a CPW transmission line resonator can be calculated according to Simmons [84]

$$Z_0 = 30\pi \left(\frac{1 + \epsilon}{2} \right)^{-\frac{1}{2}} \frac{K(k'_0)}{K(k_0)}, \quad (3.9)$$

where ϵ is the relative permittivity of the substrate. $K(k_0)$ and $K(k'_0)$ are the complete elliptic integrals with modulus k_0 and k'_0 , respectively, given by $k_0 = w/(w + 2g)$ and $k'_0 = \sqrt{1 - k_0^2}$, with w the width of the center conductor and g the width of the gap, as shown in figure 3.2. For a silicon substrate, $\epsilon \approx 11.9$ and for a sapphire substrate $\epsilon \approx 9.9$. Once we choose the substrate we will use, we can solve Equation 3.9 in Mathematica by adjusting the values of the width of center conductor w and the value of the gap g between the center conductor and ground planes in order to get the 50Ω impedance. The length l of the CPW resonator can be calculated from the dielectric constant of the substrate ϵ and resonator center frequency f_0 as follows

$$l = \frac{c}{mf_0} \left(\frac{2}{1 + \epsilon} \right)^{\frac{1}{2}}, \quad (3.10)$$

where $m = 2$ for a half-wave resonator and $m = 4$ for a quarter-wave resonator. c is the speed of light. All the resonator designs that we will discuss in this thesis have a CPW geometry. The half-wave resonators we fabricate are open at both ends; that is the center conductor and ground planes are not connected. We fabricated also quarter-wave resonators with one end open, and the other end shorted to ground.

Very high quality factors can be achieved in these resonators once we have taken care of the various sources of microwave loss. We briefly review the various loss mechanisms in CPW resonators. The analysis of equations 3.7 and 3.8 leads to the expressions for the coupling quality factor. For a half wave resonator, the coupling quality factor is given by [85, 86]

$$Q_c = \frac{n\pi}{4Z_0Z_L(2\pi f_{0n}C_c)^2}, \quad (3.11)$$

where $n = 1, 2, 3$, etc. gives the mode number. f_{0n} is the resonance frequency of the resonator mode that is excited. C_c is the coupling capacitance that is determined by the length of the elbow. For a quarter-wave resonator, the coupling quality factor is [87]

$$Q_c = \frac{\pi}{2Z_0Z_L(2\pi f_{0n}C_c)^2(2n - 1)}, \quad (3.12)$$

where $n = 1, 2, 3$, etc. gives the the different modes. The total quality factor Q of a resonator is

related to the coupling quality factor Q_c as

$$\frac{1}{Q} = \frac{1}{Q_i} + \frac{1}{Q_c}, \quad (3.13)$$

where Q_i is the internal quality factor defined by equation 3.4. The ratio Q_i/Q_c defines three coupling regimes, Thus,

$$\frac{Q_i}{Q_c} \begin{cases} > 1, & \text{overcoupled regime} \\ = 1, & \text{critical regime} \\ < 1, & \text{undercoupled regime .} \end{cases} \quad (3.14)$$

3.3 Loss mechanisms in microwave resonators

The coplanar waveguide resonator performance is sensitive to both the details of its geometry and the materials and processes that are used in its fabrication. Low losses are important for applications of superconducting resonators in quantum information or detectors. The resonator quality factor is determined by various energy loss mechanisms, namely, two-level system loss in dielectrics, the dissipation by quasiparticles, energy leaking out of the resonator through the capacitors, and radiation into free space produced by a transmission line [88]. Over the last decade, there have been many efforts to identify and minimize the individual dissipation mechanisms. In this section we describe the current understanding of the various loss mechanisms in CPW resonators. The internal loss in the resonator can be summarized as

$$\frac{1}{Q_i} = \frac{1}{Q_{rad}} + \frac{1}{Q_{TLS}} + \frac{1}{Q_{qp}} + \frac{1}{Q_v} + \dots, \quad (3.15)$$

where $1/Q_{rad}$ is the loss due to radiation, $1/Q_{TLS}$ is the loss due to two-level system in dielectric, $1/Q_{qp}$ is the loss due to quasiparticles, and $1/Q_v$ gives the dissipation due to vortices.

3.3.1 Microwave losses due to radiation and coupling to feedline

The coupling loss $1/Q_c$ is due to energy that leaks out of the CPW resonator through the coupling capacitors to the external measurement circuitry. Equations 3.11 and 3.12 tell us that the coupling loss is inversely proportional to the square of coupling capacitance and resonance frequency as

$$\frac{1}{Q_c} \propto (2\pi f_0 C_c)^2. \quad (3.16)$$

Radiation loss $1/Q_{rad}$ is given by the radiation produced by a transmission line. The radiation loss is proportional to the square of the ratio between the distance S separating the ground planes and the length L of the CPW resonator, thus [39]

$$\frac{1}{Q_{rad}} \propto \left(\frac{S}{L}\right)^2. \quad (3.17)$$

Therefore, for properly designed coplanar waveguide resonators, $1/Q_c$ and $1/Q_{rad}$ can be engineered with a high degree of control, and hence these two loss channels are not the limiting factors.

3.3.2 Microscopic Two-Level System (TLS) loss

The primary source of energy dissipation at low powers and low temperatures in superconducting CPW resonators are two-levels defects (TLS) on the various surfaces. TLS are abundant in amorphous dielectrics such as native oxides. Previous studies of two-level system distribution and loss [17, 18, 36, 77, 89–93] have shown that TLS mostly reside at metal-substrate and substrate-air interfaces. Gao et al. [90] showed that TLS loss has a strong dependence on resonator geometry, with larger loss observed for narrow CPW resonator. Typical defects in amorphous dielectrics often have two possible levels with a characteristic energy difference, and there is a broad distribution of these energy differences. But a significant fraction of TLS can have their energy difference near the energy of a typical resonator, thus providing a path for energy to leak out of the resonant mode and into the TLS. Because they have electrical dipole moments, TLS can couple to the electric fields of the coplanar waveguide resonators. At low temperatures such that $\hbar\omega > k_B T$, the internal loss due to TLS can be approximated as [17, 90]

$$\frac{1}{Q_{TLS}} \propto \frac{\tanh(\hbar\omega/2k_B T)}{\sqrt{1 + (E/E_s)^2}}, \quad (3.18)$$

where $E_s = \hbar/p\sqrt{T_1 T_2}$ is the saturation field, The numerator in right hand side reflects the thermal population difference between lower and upper level. As E increases, more TLS get driven into the excited state and saturated where they can no longer absorb energy from the resonator, thus resulting in a decrease in the internal loss due to TLS. The internal loss is expressed in terms of standing wave voltage as

$$\frac{1}{Q_{TLS}} \propto \frac{\tanh(\hbar\omega/2k_B T)}{\sqrt{1 + (V_{rms}/V_s)^{1.6}}}, \quad (3.19)$$

where $V_s \sim gE_s$ is the saturation voltage which is proportional to the width of resonator gap. TLS loss saturates at low powers corresponding to excitations of only a few photons, and at very high powers all TLS are saturated, and do not contribute loss. Some efforts to reduce TLS loss include thorough substrate cleaning and deposition process [94], the use of low-loss substrate such as crystalline sapphire and removing the substrate from regions with a high electric field density [22].

3.3.3 Quasiparticles loss

In chapter 1, we found that at low temperatures the density of nonequilibrium quasiparticles saturates, i.e, they vanish. Experiments have measured a significant quasiparticle density in the range $10 - 100 \mu\text{m}^{-3}$. Martinis et al. [79] derived an expression for the energy dissipation due to nonequilibrium quasiparticles in qubits and resonators. According to his model, the internal loss due to nonequilibrium quasiparticles in the resonator can be written as [79]

$$\frac{1}{Q_{qp}} = \left[\frac{\alpha}{\pi} \left(\frac{2\Delta}{\hbar\omega} \right)^{\frac{1}{2}} \frac{1}{D(E_F)} \right] n_{qp}, \quad (3.20)$$

where Δ is the superconducting energy gap, $\alpha = L_k/(L_k + L_g)$ is the fractional kinetic inductance equal to kinetic inductance L_k divided by total inductance, with L_g the geometric inductance. $D(E_F)$ is the two-spin density of states at the fermi energy. n_{qp} is the density of nonequilibrium quasiparticles. ω is the angular frequency. To reduce the effects of excessive quasiparticles, some traps can be engineered to restrict quasiparticles away from the resonator and thus reduce the dissipation.

3.3.4 Microwave loss due to vortices

In chapter 2 we showed that the motion of vortices in a superconductor can cause depairing of Cooper pairs and lead to energy dissipation [40, 64] and hence to a reduction of resonator quality factor [66]. In an effort to prevent vortex motion, several methods have been studied over the last decade related to controllably pinning magnetic flux vortices by use of microfabricated structures so as to reduce power dissipation and hence improve the resonator quality factor in magnetic fields. Some of these methods include the use of narrow slots [95], micropatterned holes (antidots) [96, 97] in ground planes and center conductors to reduce the degrees of freedom of vortices in the superconducting film [98]. The pinning of vortices is due to the variation in vortex energy with the length of the vortex, since vortices tend to pin in thinner regions of a superconductor so as to lower their energy [41]. We define the vortex quality factor as [66]

$$Q_v = \frac{\omega L'}{R_v}, \quad (3.21)$$

where L' is the inductance per unit length, $R_v = j(x)\rho_v l/Wd$ is the vortex resistance. W and d are the width of film and the thickness of the film, respectively. l is the length of the resonator and ρ_v is the vortex resistivity we defined in equation 2.32. d is the thickness of the superconducting film and $j(x)$ is a dimensionless factor that takes into account the variation of current density J_s along

the width of the center conductor of the resonator. It is given by [39]

$$j(x) = \frac{J_s^2(x)}{\langle J_s \rangle^2} = \frac{4}{\pi^2} \frac{W^2}{W^2 - 4x^2}, \quad (3.22)$$

where $\langle J_s \rangle$ is the average current density along the width of center conductor. Therefore we can write the vortex loss in terms of the complex resistivity as

$$\frac{1}{Q_v} = j(x) \frac{\text{Re}[\tilde{\rho}_v]}{\omega_0 W d L'}. \quad (3.23)$$

We can expand the equation 2.32 and separate real and imaginary parts,

$$\frac{\tilde{\rho}_v(\omega_0)}{\rho_f} = \frac{(\omega_0/\omega_p)^2 + \epsilon}{1 + (\omega_0/\omega_p)^2} + i \frac{(\omega_0/\omega_p)(1 - \epsilon)}{1 + (\omega_0/\omega_p)^2}. \quad (3.24)$$

Therefore, the vortex loss $1/Q_v$ in equation 3.23 can be rewritten as

$$\frac{1}{Q_v} = n_v j(x) \frac{\Phi_0^2}{\omega_0 \eta W d L'} \left[\frac{(\omega_0/\omega_p)^2 + \epsilon}{1 + (\omega_0/\omega_p)^2} \right], \quad (3.25)$$

where n_v is the density of vortices per unit area, given by $n_v = (B - B_{th})/\Phi_0$. Therefore, the vortex loss increases with the number of vortices as expected. When vortices are trapped at the location of vanishing current density, they do not cause any dissipation as the Lorentz force is zero. In contrast, vortices cause dissipation when trapped at nonzero local current density. For a superconducting coplanar wave guide resonator with a center conductor of width w and gap g , the current density is maximum at the edges of the center conductor and is smaller at the center line. Therefore, vortices trapped in middle of the resonator cause less dissipation compared to the case when they are trapped near the edges of the center conductor. In the ground planes, the current density is maximum near the edges of the gaps to the center conductor and is reduced to zero far away from the gap to the center conductor.

Furthermore, the standing wave current density varies along the length of the resonator and the value of current density depends on the type of resonator and the resonator mode that is excited. In fact, for a fundamental mode, the current density is maximum at middle of resonator and is zero at the ends of half-wave resonator, while for the quarter wave-guide resonator the current density is maximum at shorted end and zero at open end. Thus, when vortices are trapped at middle of half-wave resonator, we expect maximum vortex loss for the fundamental mode and no vortex loss when the first harmonic mode is excited.

In order to reduce the dissipation due to the moving vortices, any sort of pinning sites has to be engineered at locations of vanishing current density such as in middle of a half-wave resonator or in the ground plane far way from the resonator gaps.

Chapter 4

Experimental setup and device design and fabrication

In this chapter we will describe our microwave measurement setup, resonator design and chip fabrication, and measurement strategies. we will describe our Adiabatic Demagnetization Refrigerator and how it works, then discuss the wiring of all the microwave components we use in our measurements. we will discuss our device design using the Sonnet and Cadence tools. Then we will describe the processes that we follow to fabricate our devices. Finally we will discuss how we perform our measurements and analyze the results.

4.1 Microwave setup

4.1.1 Adiabatic Demagnetization Refrigerator

The adiabatic demagnetization, proposed by Peter Debye in 1926 and independently by William Francis Giauque in 1927 [99–101] is a process used to lower the temperature of the material. The material is first polarized in a large magnetic field at a certain temperature, then the opening of a thermal switch prevents any heat from flowing into the magnetic material while the magnetic field is reduced. With this procedure, we cooldown our devices that are pre-cooled, from 3 K to ~ 44 mK.

4.1.1.1 Brief description of ADR 106 Cryostat

We have conducted our experiments using a pulse-tube driven Adiabatic Demagnetization Refrigerator (ADR, Model 106) cryostat from High Precision Devices, Inc. (HPD). The cryostat consists

of four temperature stages at approximately 60 K, 3 K, 500 mK and 50 mK. The three stage plates (300 K, 60 K, and 3 K) of the cryostat are connected by thermally isolating supports. The cryostat has a vacuum jacket, 60 K shield, and a 3 K shield. The cryostat connects to a Cryomech Pulse-Tube Refrigerator (PTR). The PTR is a closed loop system consisting of a water-cooled compressor connected to the remote motor by helium gas flex lines, the PTR provides the cooling of the 60 K and 3 K stages.

ADR 106 contains a superconducting 4 T magnet within a Hiperco 50 magnetic shield, a Kevlar suspension system, and two paramagnetic salt pills. The paramagnetic salt pills used are Gadolinium Gallium Garnet (GGG) pill that can cool to 500 mK and the Ferric Ammonium Alum (FAA) salt pill that can cool to a base temperature a ~ 44 mK. The salt pills are connected to copper cold fingers that we then attach our experimental hard ware onto. A Kevlar suspension system isolates the salt pills from warmer stage temperatures while supporting experimental loads of a few pounds (Maximum recommended weight be about 2 kg). The superconducting magnet generates the magnetic field necessary for the operation of the ADR. It has a large inductance of 32.17 H, a room-temperature resistance of 11.25 k Ω , and a fieldto-current ratio of 4.364 kG/A. A gold-plated copper thermal shield reduces the radiative load on the Hiperco 50 shield and magnet [102]

When the heat switch is closed, the 3 K stage is shorted thermally to both colder stages of the ADR (FAA and GGG). When the heat switch is open, the 3 K stage and both FAA and GGG stages are disconnected thermally from each other. There are Ruthenium Oxide (RuO₂) thermometers mounted on both the 500 mK and 50 mK stages, while a silicon diode thermometer is mounted on each of the 60 K and 3 K stages.

4.1.1.2 ADR 106 cryostat cooldown procedure

The cryostat volume must be under vacuum during operation to avoid gaseous thermal conduction between the room-temperature vacuum jacket and the various stages. We use a portable turbo pump cart with a scroll backing pump. Initially we use the scroll pump to reach the pressure of $\sim 10^{-3}$ Torr. Then we turn on the turbo pump, initially at low-speed mode and then switch to the high-speed mode, to pump the cryostat down to high-vacuum ($\sim 3 \times 10^{-5}$ Torr). To get good vacuum we usually handle the cryostat shield with gloves to avoid any fingerprint buildup or particle contaminants on the vacuum sealing surfaces.

Once the cryostat has reached a sufficiently high vacuum level ($\sim 3 \times 10^{-5}$ Torr), we open and close the heat switch. Then we open the water valve to allow cooling water to flow through the compressor. Note that, due to a slow leak in the high-pressure helium system for this particular ADR, it is important to check that the helium pressures in the flex lines reads ~ 220 psi when

the compressor is not running. Otherwise if the static pressure is low, the compressor needs to be recharged with ultra-high purity helium gas. We turn on the pulse tube compressor and run the LabVIEW program to record the temperatures of 60 K and 3 K stages as the cryostat cools down from room temperature.

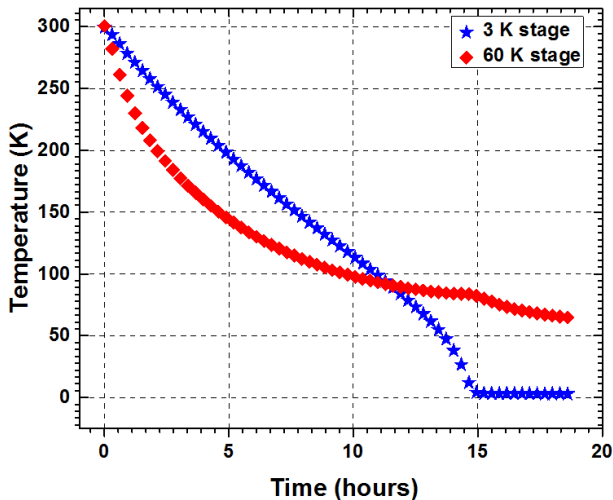


Figure 4.1: Temperatures vs. time for the 60 K (Red) and 3 K (Blue) stages of the pulse-tube refrigerator during an initial cooldown of the ADR cryostat from room temperature.

After approximately 15-16 hours, the 3 K stage temperature should have fallen below 50 K, and the cryostat will have reached a high vacuum level ($\sim 4 \times 10^{-8}$ Torr). We close the vacuum valve, then we turn off the pump cart and disconnect it. At temperatures below 50 mK the cryostat’s ability to cryopump any slowly leaking gas is more effective than the turbo pump cart.

4.1.1.3 Magnetization process

When the temperature of the ADR magnet has reached around 3 K, we cycle (open and close) the heat switch to ensure functionality before beginning the first magnetization cycle. For the initial cooldown from room temperature, we let the compressor run about 18-20 hours before starting an ADR cycle to allow for better thermal equilibration of the GGG and FAA salt pills.

With the heat switch kept closed, we gradually increase the current flowing in the superconducting magnet using an Agilent system DC power supply (Model 6641A, 0-13 V/ 0-15.3 A) operated in a constant voltage mode, until reaching the full field. We typically apply 620 mV using the power supply to reach the maximum magnetic field, corresponding to a current flowing in the magnet of

9.06 A and a magnetic field of about 4 T. Note that for the ADR cryostat Model 106 the maximum current the superconducting magnet can withstand is 9.17 A. During the next re-magnetization cycles, we close the heat switch after the salt pill temperatures reach that of the 3 K stage. Doing that will prevent any heat flow from 3 K stage to cold finger that could potentially quench the superconducting magnet. To prevent the magnet from quenching, we ramp up the voltage of system DC power supply at a rate of 0.07 mV/s for the voltage developed across the superconducting magnet not to exceed 0.1 V. At the full field, we cycle the heat switch (open and close), so as to free any thermal stresses in the switch mechanism and Kevlar suspension system. We then wait for the salt pill to soak for enough time (1-4 hours) before beginning demagnetization.

4.1.1.4 Adiabatic demagnetization process

We keep the heat switch closed to let the salt pills soak for more than an hour. The purpose of the soaking process is to allow the salt pills to equilibrate at their maximum magnetization at the lowest temperature of the pulse tube cooler. We then open the heat switch and unplug its power cord in order to start the demagnetization process. Recall that when the switch is open, the 3 K stage and both 500 mK and 50 mK stages of the ADR are disconnected thermally from each other. We reduce the current through the superconducting magnet by decreasing the voltage of the system DC power supply. The salt pill cools because the magnetic field is being reduced and the process is adiabatic since the heat switch is open. Because no heat can flow, the temperature must decrease as B is reduced.

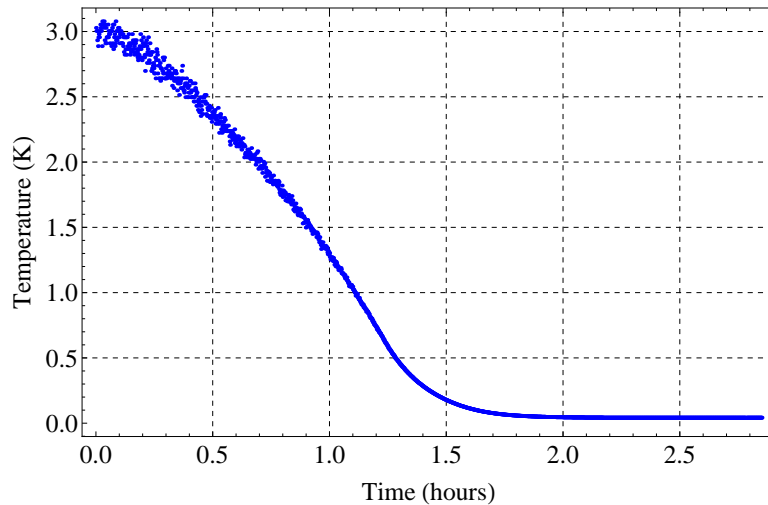


Figure 4.2: Cooling of FAA salt pill coupled to sample during adiabatic demagnetization.

We slowly ramp down the voltage of the magnet power supply at a rate of 0.07 mV/s, and

eventually no current flows through the superconducting magnet and the magnetic field is zero. Reducing the magnetic field from 4 T to zero takes about 1 hour and a half. With the magnetic field reduced to zero, the temperature of the FAA stage that supports the experimental loads (sample and connectors) will have reached the base temperature of around 44 mK. In order to keep the temperature of the cold finger above the base value 44 mK, we increase the magnet field above zero. Therefore, if the sample starts to warm up, to compensate for any heat absorbed by salt pill, we slowly decrease the applied magnetic field whereas, if the sample temperature drops, we increase the applied magnetic field to compensate for any heat reduction in the salt pill. The ADR model 106 cryostat that we use can maintain the sample at temperatures below 150 mK for at least 24 hours. After that time, as we can no longer hold the temperature constant we must repeat the magnetization-demagnetization cycle.

4.1.2 Experimental wiring in cryostat

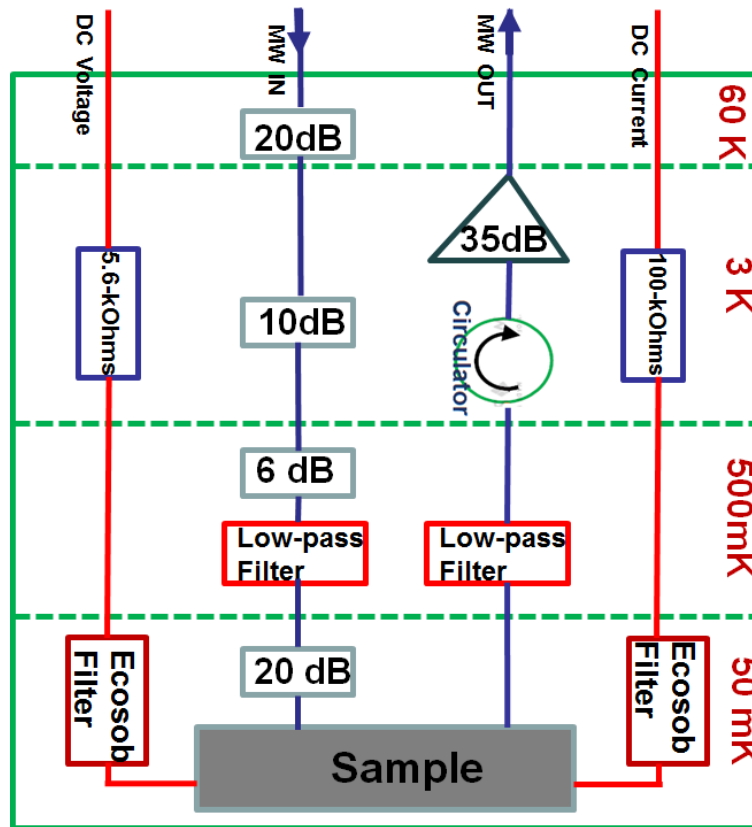


Figure 4.3: Microwave measurement setup.

The ADR cryostat microwave input and output coax cables are made of copper nickel (CuNi) coax, with a silver-clad inner conductor (SC-086/50-SCN-CN). All the measurements were done in the ADR described above, using the vector network analyzer (VNA, model N523A, 300kHz-20GHz). The microwave input signal sent from the input port of the VNA goes through 20 dB of attenuation at the 60 K stage, followed by 10 dB at 3 K stage and 6 dB at 500 mK stage. It then enters a low-pass filter that has a roll-off at ~ 11 GHz mounted at 500 mK. Before entering the sample holder, the input signal passes through a final 20 dB attenuator anchored to the cold finger near the sample holder. In total we have 56 dB of cold attenuation on the input line in addition to the frequency-dependent coax cable loss (Figure 4.3). Note that we distribute the attenuators at different stages of ADR to minimize any thermal noise and also interference from room temperature. The output microwave signal passes through a second low-pass filter, mounted also at 500 mK, followed by a circulator at 3 K. The signal is then amplified by a high electron mobility transistor (HEMT) amplifier mounted at 3 K. The circulator and low-pass filter on the output line attenuate any noise from the HEMT before it reaches the sample. Before entering the output port of the VNA, the signal is further amplified by a 35 dB-gain room temperature amplifier.

4.1.3 Cryogenic microwave amplifier

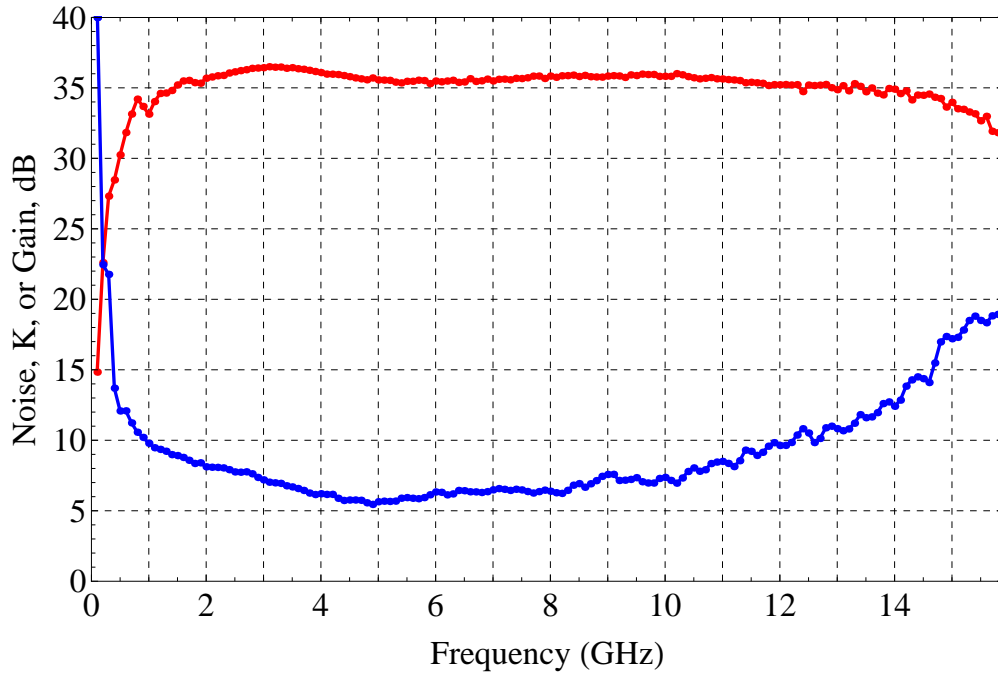


Figure 4.4: Noise temperature (Blue) and gain (Red) of HEMT amplifier, for temperature below 17 K. These curves are taken from the Caltech datasheet for this HEMT.

We are interested in measuring the resonators at very weak microwave powers, so we require significant amplification to be able to have a measurable signal. At the same time, we need amplifiers with extremely low added noise in order to have a reasonable signal-to-noise ratio. The output microwave signal is amplified by a high electron mobility transistor (HEMT, model SN479D) amplifier from Caltech. It is mounted at 3 K stage. The HEMT has a constant gain over a wide range of frequencies 1 – 12 GHz. The noise temperature of the HEMT is about 5 K. We bias the HEMT using a homemade bias box. We use one voltage power supply to apply the drain-source bias and the voltage bias for the two gates. We apply a drain voltage equal to 1.2 V which produces 23.5 mA of current. The bias voltages for the gates are the same, and equal to 0.25 V. These bias points correspond to the optimum gain and noise performance for this particular HEMT.

4.1.4 Vector network analyzer and S-parameters

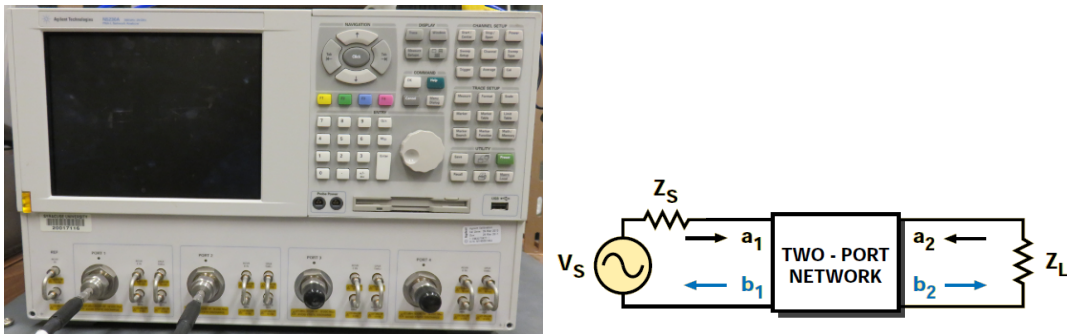


Figure 4.5: Left: Vector Network Analyzer (VNA). Right: a circuit diagram for a two-port network.

We measure resonators using a vector network analyzer (VNA, Agilent model N5230A, 300kHz-20GHz). The data from the VNA consists of the complex transmission S_{21} for the 800 frequency points in the desired frequency span. We briefly discuss the scattering parameters (S-parameters) for a two-port network. These parameters define relations between variables (a_i, b_i) . The independent variables a_i and dependent variables b_i are normalized complex voltage waves incident on and reflected from the port i of the network, respectively. They are defined in terms of the terminal voltages V_i . For a two-port network, they defined as follows [83, 103, 104]

$$a_1 = \frac{V_{i1}}{\sqrt{Z_0}} \quad (4.1)$$

$$a_2 = \frac{V_{i2}}{\sqrt{Z_0}} \quad (4.2)$$

$$b_1 = \frac{V_{r1}}{\sqrt{Z_0}} \quad (4.3)$$

$$b_2 = \frac{V_{r2}}{\sqrt{Z_0}}. \quad (4.4)$$

where Z_0 is the characteristic impedance. S-parameters are dimensionless and that they are typically measured in decibels. For a two-port network, the S-parameters are defined by the following linear equations

$$b_1 = S_{11}a_1 + S_{12}a_2 \quad (4.5)$$

$$b_2 = S_{21}a_1 + S_{22}a_2 \quad (4.6)$$

or in matrix notation

$$\begin{pmatrix} b_1 \\ b_2 \end{pmatrix} = \begin{pmatrix} S_{11} & S_{12} \\ S_{21} & S_{22} \end{pmatrix} \begin{pmatrix} a_1 \\ a_2 \end{pmatrix}. \quad (4.7)$$

S_{11} is the input reflection coefficient with the output port terminated by a matched load set by $Z_L = Z_0$, $S_{11} = b_1/a_1$ for $a_2 = 0$. S_{22} is the output reflection coefficient with the input port terminated by a matched load set by $Z_S = Z_0$, $S_{22} = b_2/a_2$ for $V_S = 0$. S_{21} is the forward transmission with the output port terminated in a matched load, $S_{21} = b_2/a_1$ for $a_2 = 0$. S_{12} is the reverse transmission with the input port terminated in a matched load, $S_{12} = b_1/a_2$ for $a_1 = 0$. In our experiments, we measure the magnitude and phase of the complex forward transmission S_{21} .

4.1.5 Shielding and generation of magnetic fields

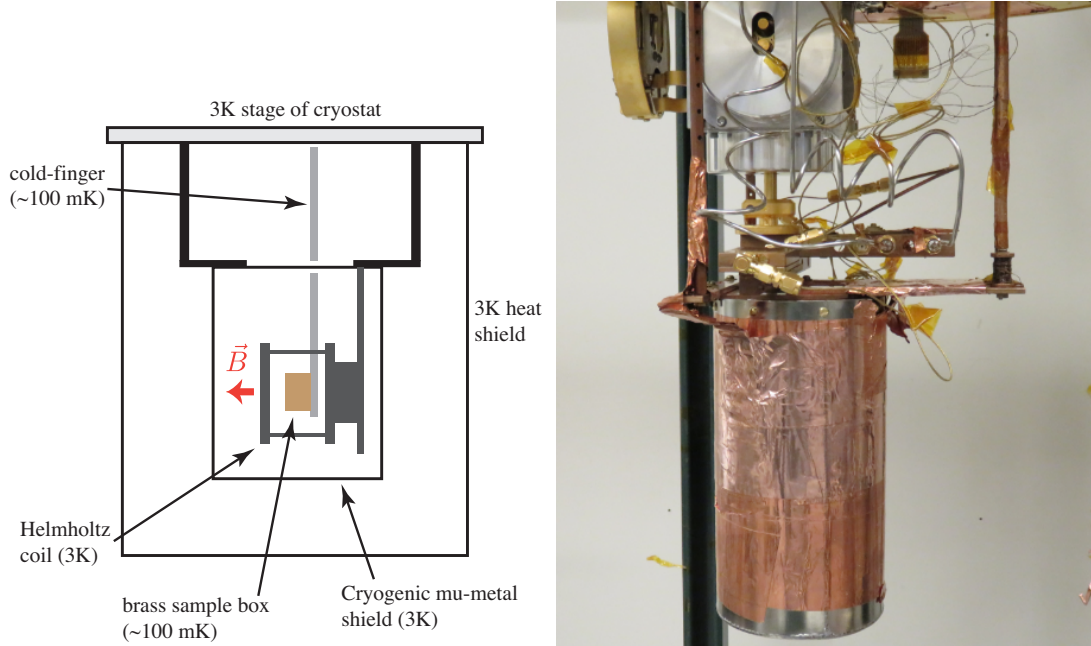


Figure 4.6: Left: Schematic of cryostat including sample brass box and mount along with Helmholtz coil (not to scale). Right: Cryoperm shield mounted on the 3K plate.

We would to apply a magnetic field to the sample in order to trap vortices in the microwave resonators. The magnetic field is applied perpendicular to the sample and we have used a homemade Helmholtz coil that has same dimensions as the one described in reference [39]. At 3K stage, the superconducting wire is made of niobium titanium CuNi-clad with a diameter of 0.005 inch. The coil wire at upper stages and outside of ADR is made of copper wire. The helmholtz coil frame is made of Oxygen-free high thermal conductivity (OFHC) copper. The radius of the coil is 1.25 inch we have made 115 turns on each coil, so the total number of turns in the two coils is 230. At room temperature, the resistance of the superconducting wire is $1050\ \Omega$ and the resistance is $\sim 0.5 - 1\ \Omega$ at millikelvin temperatures. We typically apply small fields in the range $0 - 220\ \mu\text{T}$ without noticing any heating of the cold finger or 3K stage. A cryogenic mu-metal can at 3K shields the resonator from stray magnetic fields outside of the cryostat as well as any residual stray fields from the ADR magnet. We cooled down a test device and measured both positive and negative magnetic fields applied from the Helmholtz coil, and we estimated the component of the background magnetic field perpendicular to our sample to be less than $2\ \mu\text{T}$. This value is much smaller the threshold fields to introduce vortices in all of the devices that we have studies.

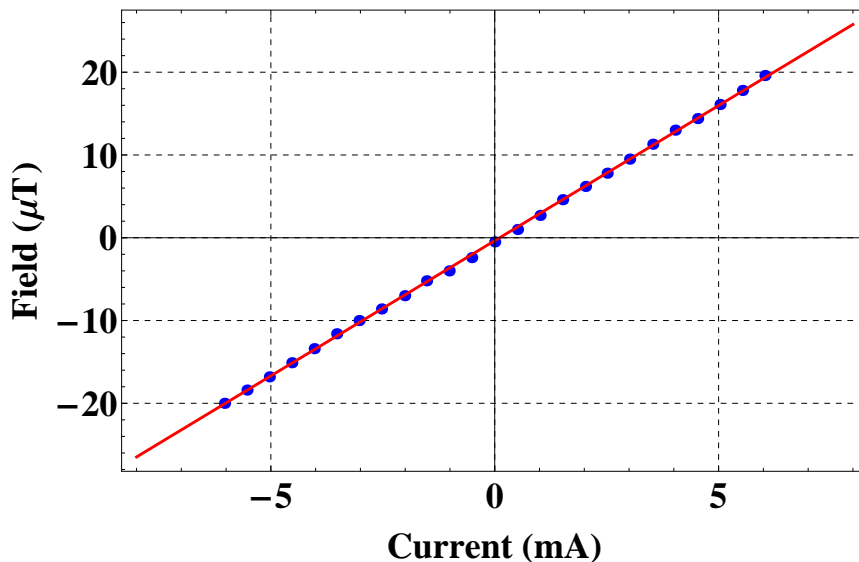


Figure 4.7: Plot of calibration for converting applied current to magnetic field in the Helmholtz coil, the slope is $3.23\ \mu\text{T}/\text{mA}$.

Using the Lakeshore Gaussmeter (Model 450), we calibrated the Helmholtz coil to convert current in mA that we apply using a current source to the resulting magnetic field in μT . We calculated the conversion factor to be $3.23\ \mu\text{T}/\text{mA}$ by fitting the calibration data as shown in figure 4.7. We recall that the current and magnetic field in a Helmholtz coil are related as $B = (4/5)^{3/2}(\mu_0 n I / R)$ where

n is the number of turns, I is the applied current, μ_0 is the magnetic permeability in free space, and R is the coil radius. This expression gives $B/I \approx 3.27 \mu\text{T}/\text{mA}$, which is close to our measured slope. We place our sample mounted on the cold finger ($\sim 44 \text{ mK}$) in the middle of the Helmholtz coil that is attached on the 3 K stage. We minimize any stray background magnetic field by using a cryoperm shield mounted also on 3 K plate.

4.2 Microwave resonator design

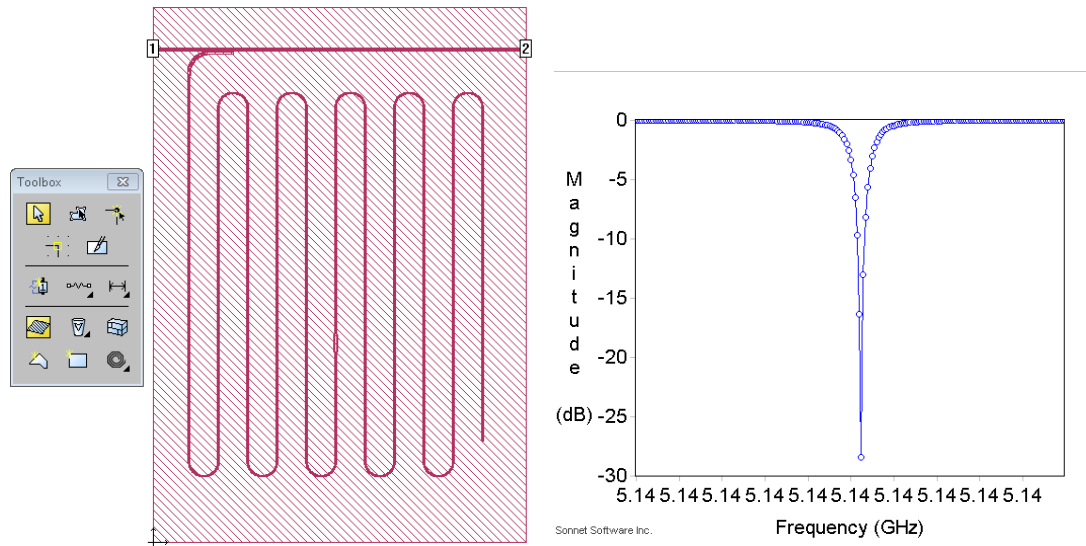


Figure 4.8: Drawing of resonator design and simulated frequency response $|S_{21}|$.

We are using superconducting resonators to study the dynamics of trapped vortices and nonequilibrium quasiparticles. Each type of experiment that we perform drives the design of the resonator layout such as the resonance frequency, the coupling quality factor Q_c , resonator linewidth, etc. We decide on the structures and dimensions of each resonator and substrate that we want to use for our experiments. Using Mathematica we compute some of the resonator parameters such as the gaps on both side of resonator and feedline center conductor that would give a 50Ω impedance, using the equations 3.10 and 3.9. We then draw and simulate the resonator using Sonnet and AWR tools. We come up with final resonator designs that meet our needs such as range of resonance frequencies or lengths of the resonator, resonator coupling quality factor or resonator coupling capacitance. By including the kinetic inductance, calculated based on results from our previous resonator measurements and simulations, we obtained good match between designed and measured resonance frequencies. We designed half-wave and quarter wave CPW resonators, with fundamental resonance

frequencies in the range 3-7 GHz. To avoid trapping vortices everywhere in the ground planes, we include holes of $5.6 \mu^2$ in the ground plane to trap magnetic flux. The spacing of holes is designed to be less than the linewidth of the center conductor of the resonator as shown in figure 4.9 and also in figure 4.10.

4.2.1 Resonator mask design and writing

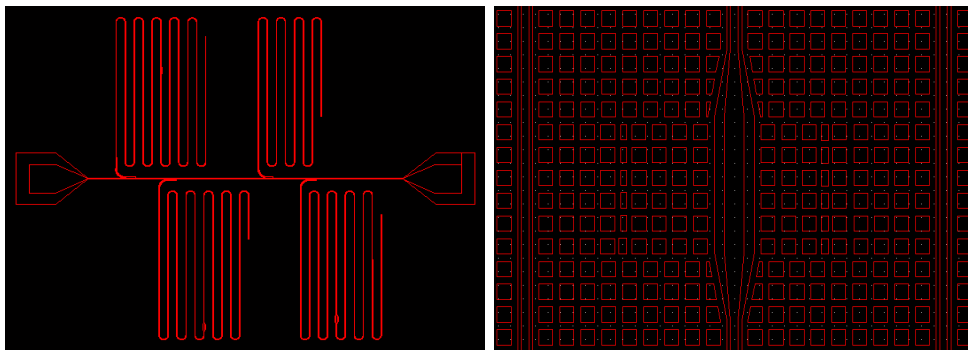


Figure 4.9: Chip design in Cadence software.

Once we have finished the simulations of the resonator using Sonnet, we use the Cadence computer-aided design software tool to draw the designs in a layout appropriate for one of the photosteppers at the Cornell NanoScale Facility. From Cadence we export a gds file that we will transfer to the mask writer tool. We have written the sample patterns using the Heidelberg Instruments DWL 2000 using a 4 mm lens on a photosensitive chrome mask plate. We write the masks to use with GCA Autostep 200 DSW i-line stepper and masks to use with ASML 300C DUV Stepper. After writing the patterns, we use Hamatech-Steag HMP900 Mask processor to develop automatically (using MIF-726 developer) and then etch (chrome etch) the mask. Before using the mask, we soak it in a resist hot strip bath that contains heated solvent for photoresist stripping for about 30 minutes. We use a dump rinser and double-stack rinse dryer for easy stripping of the photomask.

4.3 Chip fabrication

We evaporated a 60 – 150 nm thick aluminum layer over the whole 4 inch, (100)-oriented high resistivity ($10 \text{ k}\Omega - \text{cm}$) Silicon substrate, purchased from Addison Engineering, Inc. and patterned using photolithography. We fabricated resonators at Cornell NanoScale Science and Technology Facility (CNF). The resonators we discussed in chapter 5 and 6 were patterned using GCA Autostep 200 DSW i-line Stepper. All other resonators we describe in this thesis were patterned using ASML

300C DUV Stepper. ASML mask is much bigger than Autostep mask, and in addition to this, ASML tool offers an option to choose which patterns to expose, and we can pattern more sample designs. We have used SPR220-3.0 resist to pattern aluminum layer on Autostep. On ASML, we have used two layers of resists, a bottom layer of the anti-reflective resist DSK101-312 that is 120 nm thick and a top layer of DUV210-0.6 that is 700 nm thick.

4.3.1 HF cleaning versus ion-milling of silicon wafer

Prior to aluminum evaporation onto the silicon wafer we carefully clean the silicon substrate surface to remove any residues or oils or to remove/decrease native oxides present on the silicon substrate surface. We briefly review here the standard recipe to treat the silicon surface. One way to clean the silicon surface is in-situ ion-milling of wafer surface between 6 – 13 seconds. We perform the ion-milling step in the evaporation chamber at Syracuse University immediately before the aluminum evaporation. During ion-mill, argon ions are accelerated by the ion gun towards the wafer and bombard the surface of the wafer and gradually remove organic residues, oils and native oxides that are present on the silicon surface. HF/RCA clean is an alternative that we haven't pursued for this fabrication because the HF/RCA cleaning area is at the CNF and our deposition system is at Syracuse.

4.3.2 Wet etch of aluminum

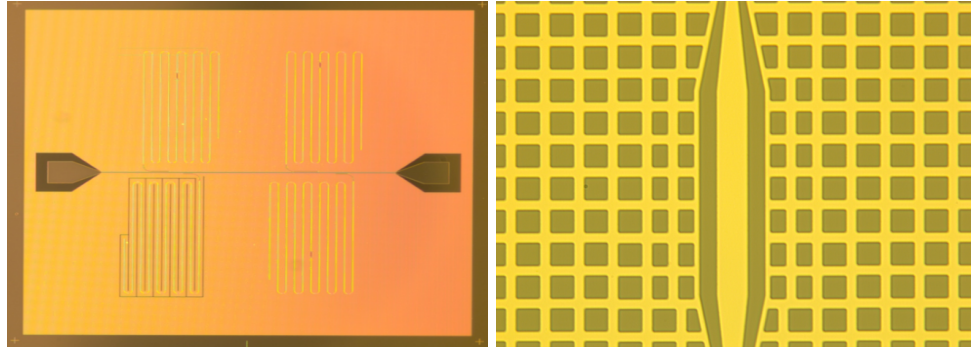


Figure 4.10: Left: Optical micrographs of chip after wet etch. Right: Zoom-in of bulge region for vortex trapping near center of resonator.

The wafer with patterned Aluminum layer is structured using wet etch into 4 to 6 half-wave ($\lambda/2$) resonators of different frequencies f_0 and coupling quality factors Q_c . All the resonators we fabricate have the CPW geometry. For each chip the resonators are coupled through the elbows to a feedline. We wet etch Aluminum using Aluminum etchant type-A, a standard Aluminum etchant for use on

silicon devices. One of the advantages of aluminum etchant type-A is that it does not attack silicon or silicon dioxide. After fabrication, we cover the wafers with a polymethyl methacrylate (PMMA) or SPR220-3.0 layer to protect them during dicing. We dice the wafer at a speed of 3.25 mm/sec into chips of 6.5 mm^2 using the dicing saw DISCO at Syracuse University. We then remove the resist layer covering the chips prior to mounting in sample holders for measurements. We strip off the protective resist using acetone followed by isopropanol and a deionized water rinse. An alternate recipe we often use to strip off resist is 1165 resist stripper heated to 60 Celcius degrees, followed by a deionized water rinse.

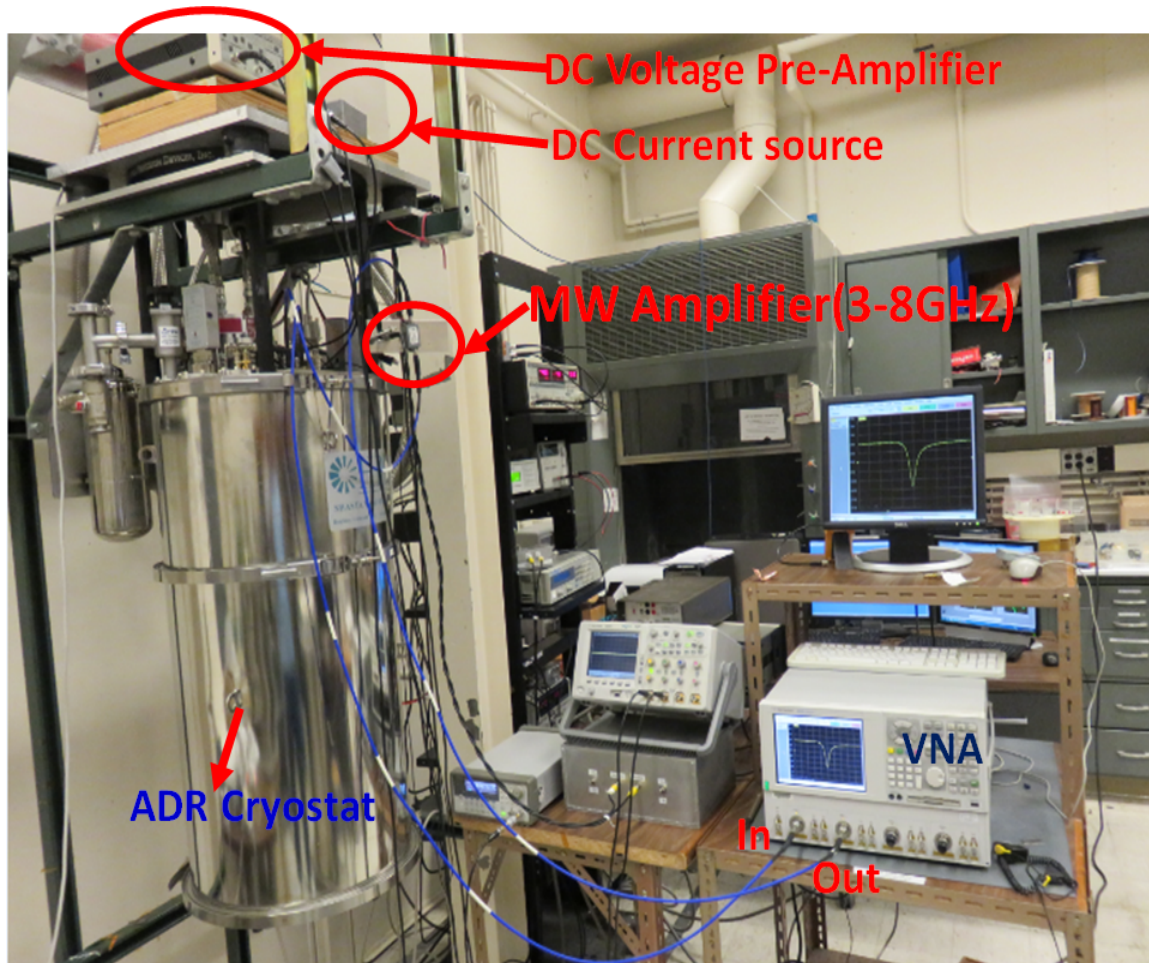


Figure 4.11: Microwave measurement setup outside the ADR cryostat.

4.4 Resonator measurement

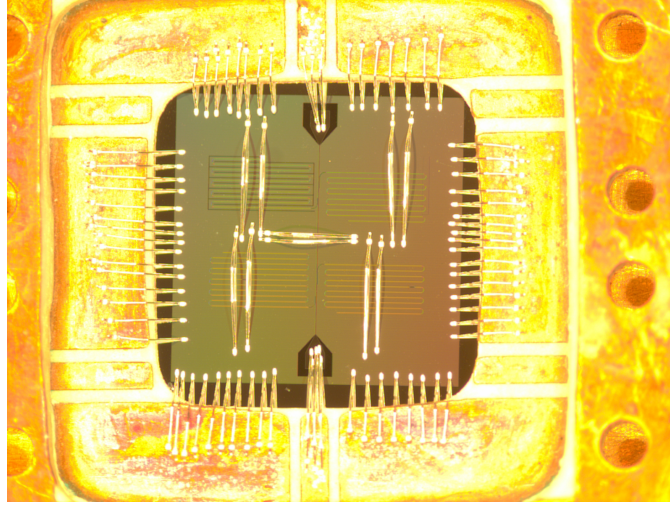


Figure 4.12: Chip wirebonded on a printed circuit board.

The device is wire-bonded to a microwave board and enclosed in a brass box. We adjust the cold-finger to position the sample at the center of the Helmholtz coil. The arrangement of the various components and their associated temperatures is shown in figure 4.6. We add room temperature amplifier with a Gain of 35 dB to further amplify the microwave output signal.

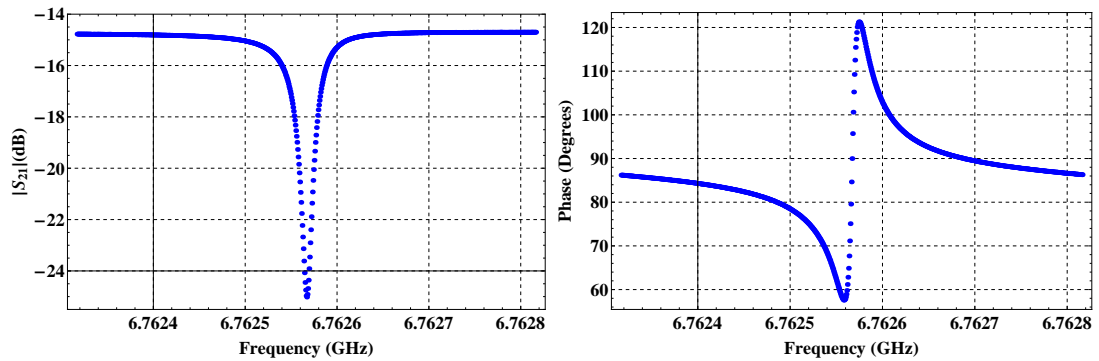


Figure 4.13: Magnitude and phase raw data of forward transmission S_{21} . The data was measured for a small span of (0.5 MHz) with 800 frequency points.

We measure the forward transmission S_{21} of the resonators directly using the vector network analyzer by sweeping the frequency of the microwave signal applied along the feedline. To allow the ADR to remain at the measurement temperature for as long as possible while minimizing thermal quasiparticles, we have chosen to do our resonator measurements at 100 mK.

4.4.1 Extracting resonator parameters with a 4-parameter fitting routine

The transmission signal $S_{21}(f)$ through the sample, attenuators, filters, amplifiers and cables can be written as follows [92]:

$$S_{21}(f) = ae^{-2\pi if\tau} \left[1 - \frac{Qe^{-i\theta}/Q_c}{1 + 2iQ\delta x} \right]. \quad (4.8)$$

The parameters a , τ and θ account for the gain, cable delay, and rotation of the resonance circle in the complex plane, respectively. $\delta x = (f - f_0)/f_0$ is the fractional frequency shift, with f_0 the resonance frequency. In chapter 3 we showed that the resonator total quality factor Q is related to coupling quality factor Q_c as in equation 3.13

$$\frac{1}{Q} = \frac{1}{Q_i} + \frac{1}{Q_c},$$

where Q_i is the resonator total internal quality factor. The fitting model in 4.8 contains 6 parameters. In our fitting routine, we calibrate out the two parameters a and τ by performing a subtraction of a separate baseline measurement of the magnitude and phase of the background transmission [3].

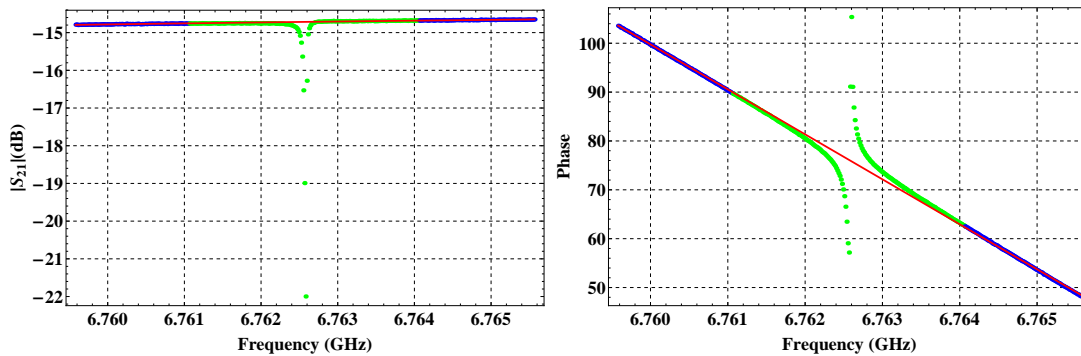


Figure 4.14: Magnitude and phase of background transmission. The blue points far away from the resonance were used to find a polynomial and linear fit functions for the magnitude and phase, respectively. The data was measured for a wide span of 6.0 MHz.

We use the vector network analyzer to measure the magnitude of S_{21} for a wide span (6.0 MHz) centered on each resonance, and we find a polynomial fit and linear fit functions for points away, for the magnitude and phase of S_{21} , respectively,

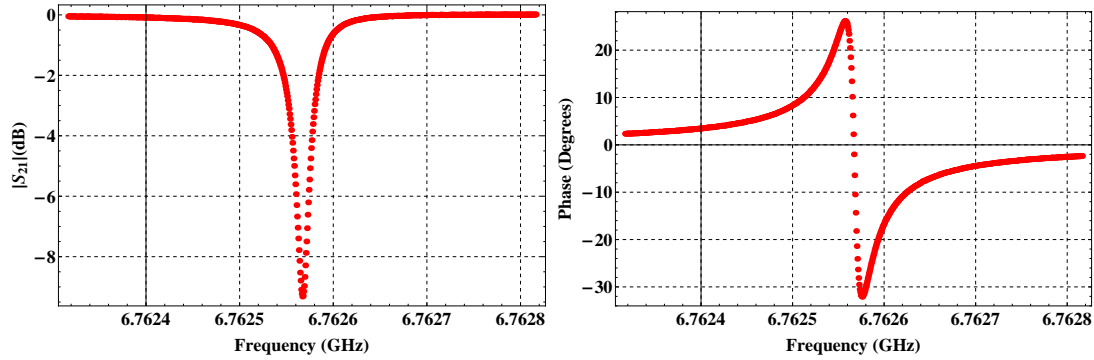


Figure 4.15: Plots of magnitude and phase after subtracting off the baseline transmission data.

We then subtract off the polynomial fit function from the magnitude of S_{21} taken for a small frequency span zoomed in on each resonance of frequencies (0.5 MHz) in figure 4.13. We follow a similar procedure for the phase by using a linear fit function instead of polynomial fit function. After we have corrected for the gain and cable delay, we can now rewrite the expression 4.8 (by setting $a = 1$ and $\tau = 0$) as follows

$$S_{21}(f) = 1 - \frac{Qe^{-i\theta}/Q_c}{1 + 2iQ\delta x}. \quad (4.9)$$

The expression has a Lorentzian shape. From the magnitude and phase of S_{21} we calculate the real and imaginary parts of the transmission signal, and when plotted in the complex plane, this function forms a circle.

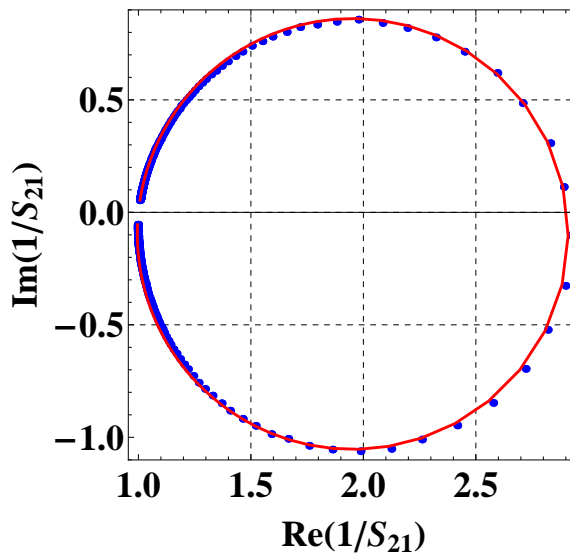


Figure 4.16: Calibrated complex transmission data fitted with a 4-parameter fit model in complex plane.

After the calibration of the magnitude and phase, we now have only four fitting parameters.

We fit the inverse of $S_{21}(f)$ as described in [94] in the complex plane to extract the resonator total internal quality factor Q_i , the resonance frequency f_0 and the coupling quality factor Q_c . We have written a mathematica routine to perform the above four parameter fit procedure.

4.4.2 Calibration of the input line and resonator input power

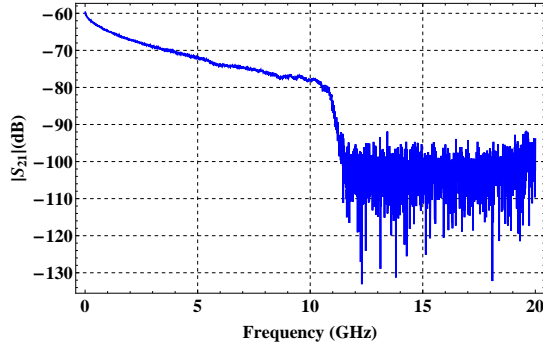


Figure 4.17: Measurement of input coax cable attenuation from top to bottom of ADR cryostat. The measurement was done at room temperature

The coax cables contribute a frequency-dependent loss in addition to the significant amount of cold attenuation that we add on the line. We have done the calibration of the input coax cable to find the total attenuation of the input line and then calculated the internal power inside the resonator following the same procedure as detailed in references [86, 105]. In figure 4.17 we plot the baseline transmission of the input cabling as a function of frequency. We perform numerical interpolation of the baseline transmission in Mathematica in order to find the interpolation function for frequency range 0.3 – 11 GHz and evaluated the total attenuation for each resonator mode that we measured. Therefore, for each resonator mode the microwave readout power P_f at input of the sample’s feedline is calculated as

$$P_f = P_{VNA} + dp, \quad (4.10)$$

where dp is the total attenuation on the input line and P_{VNA} is the power sent from the vector network analyzer. In equation 4.10, we assumed that the changes in attenuation that likely occur upon cooling down the coax cables, attenuators, etc. are so small and can be neglected. We recall that to convert power in Watts, we use $P(\text{Watts}) = 10^{[(P(\text{dBm})-30)/10]}$, or convert back to dBm as $P(\text{dBm}) = 10 \log_{10} P(\text{Watts}) + 30$. The internal power inside the resonator is given by

$$P_{\text{int}} = \alpha \frac{Q^2}{Q_c} P_f, \quad (4.11)$$

where $\alpha = 2/\pi$ for a half-wave resonator, and $\alpha = 1/\pi$ for a quarter-wave resonator [86].

4.4.3 RRR and low temperature resistivity measurement

The residual resistivity ratio of a metal film, i.e RRR, is defined as the ratio of resistance at 293 K to the resistance at 4.2 K [66]. We have measured the resistance of the feedline using a 4-wire measurement technique. For one particular aluminum film with the thickness $t = 60$ nm, we measured the resistance equal to $R_{293\text{ K}} = 295.3\ \Omega$. We dip the test sample into liquid helium, and measure the resistance of the feedline at 4.2 K, we find $R_{4\text{ K}} = 34.5\ \Omega$. Therefore, RRR is equal to ~ 9 . The total length L of feedline trace is $2965\ \mu\text{m}$ and its width w is $6\ \mu\text{m}$ (and hence the feedline cross-section area A is equal to $t \times w$). We deduct that the low temperature resistivity of our aluminum film is $0.5\ \mu\Omega - \text{cm}$ ($\rho = R \times A/L$). For the various aluminum films that we have measured, RRR values range between 8 – 10, and the low temperature resistivity values are in the range $0.3 - 0.7\ \mu\Omega - \text{cm}$.

Chapter 5

Trapping a single vortex in the microwave resonator

5.1 Introduction

The microwave response of superconducting coplanar waveguide resonators can be affected by the conditions in which they are operated. In fact, microwave components often have strong magnetic field or the magnetic shielding may not be ideal, therefore vortices can penetrate in the center conductor of resonators or in the ground plane of the chip. The response of magnetic flux vortices in superconducting thin-film has been studied in several previous field-cooled experiments in the context of vortex viscosity as well as pinning of vortices [66]. In general, when magnetic flux vortices are trapped in the resonator, they can cause a reduction in resonator quality factor, and the magnitude of the effect scales with the total number of vortices. Vortices also can cause a downwards shift in the resonance frequency. Several techniques have been proposed in an efforts to reduce power dissipation and hence improve the resonator quality factor in the circuits that require operation in large magnetic fields. Many of these techniques consist of microfabricated structures such as the use of narrow slots [95], micropatterned holes (antidots) [96, 97] in ground planes and center conductor to reduce the degrees of freedom of vortices in the superconducting film [98]. All of these experiments involved microwave resonators with many trapped vortices. In this chapter, we present our first experiments aimed to quantify the response of a single vortex in such a microwave circuit.

5.2 Design of structures for resolving a single vortex

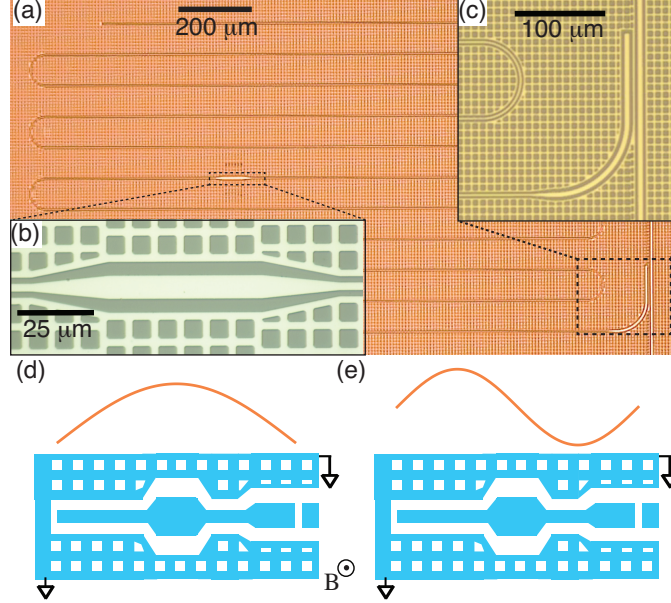


Figure 5.1: Optical micrographs of (a) entire resonator including feedline, (b) close-up of bulge region for vortex trapping near center of resonator, (c) close-up of coupling elbow and feedline. Schematic of resonator without turns (not to scale) along with standing-wave pattern of microwave current for (d) fundamental, (e) first-harmonic resonance. From Nsanzineza & Plourde, *Physical Review Letters* 113, 117002(2014) [3].

We want to study the microwave response of few vortices in the CPW resonator. To do that, we have designed a device based on the fact that the threshold field to trap vortices goes like $\sim 1/w^2$. We introduced a bulge in the middle of our half-wave resonator to control the location of the trapped vortices upon field-cooling. The bulge is $8 \mu\text{m}$ wide and $50 \mu\text{m}$ long. The width of the elbow coupler is $6 \mu\text{m}$ and its length determines the coupling quality factor as we explained in chapter 4. The rest of resonator is designed to be $3 \mu\text{m}$ wide. Therefore, the bulge region will begin trapping vortices at a smaller applied magnetic field compared to the rest of the resonator.

To resolve the microwave dissipation from just a single vortex, we also needed to optimize some other parameters. We needed to do our measurements at low temperatures, $50 - 100 \text{ mK}$ to reduce the density of hot quasiparticles, and hence we suppress any dissipation from these quasiparticles. As discussed in chapter 4, we can achieve millikelvin temperatures with the Adiabatic demagnetization refrigerator (ADR). With a vanishing loss from hot quasiparticles, we now have the flexibility to design weakly coupled resonators, we designed resonators with coupling quality factors in the range $500k - 1M$. Our device is shown in figure 5.1. It is intended to have reasonably high internal quality factor Q_i so that we can resolve the influence of individual vortices. Furthermore, to prevent any

vortices to be trapped outside of the center conductor of the resonator, we designed holes in the ground plane that are $5.6 \mu\text{m}$ wide and separated by a superconducting web that has a linewidth of $2.8 \mu\text{m}$.

The resonator we discuss in this chapter is 17.1 mm long and is capacitively coupled to the feedline through an elbow-style capacitive coupler at one end, the other end is an open circuit as shown in figure 5.1. For the fundamental resonance, we expect that a vortex trapped in the middle of the resonator at the center of the bulge will experience a strong Lorentz force, and hence contribute to more loss. On the contrary, from the standing-wave current pattern of the first harmonic in figure 5.1 we can notice that the middle of resonator corresponds to a current node, and a vortex sitting there do not feel Lorentz force, and hence no vortex loss. Therefore, for applied magnetic field to trap vortices only in bulge we expect zero vortex loss and, therefore, no change in the quality factor for first harmonic, and an increase in vortex loss for fundamental resonance. We have evaporated 60 nm of aluminum film and fabricated the resonators following the procedure as discussed in chapter 4. The CPW resonator that we measured in this experiment is quite narrow ($3 \mu\text{m}$) along most of its length and, therefore, should have a large superconducting kinetic inductance contribution. So, the nonlinear effects of the superconducting resonator itself dominate the frequency response to changes in the magnetic field [106]. Because of that, we have chosen to focus our analysis on the changes in vortex loss, rather than changes in the resonance frequency.

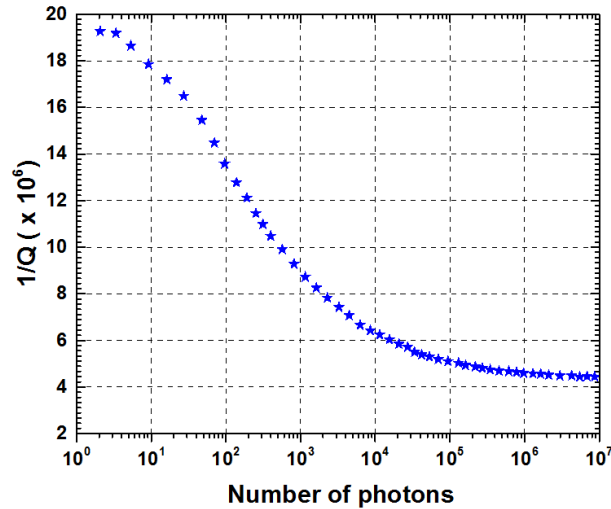


Figure 5.2: Power dependence of total resonator loss for the fundamental resonance 3.0713 GHz and coupling quality factor $Q_c = 765,000$. All field-cooled measurements were performed at sufficiently high powers, with $\sim 10^5$ photons in the resonator.

5.3 Field-cooled measurement

We discuss the field-cooled measurements of a CPW resonator with a geometry that we designed so that we can trap vortices in only a small region over a range of applied magnetic fields. We measured the device on an adiabatic demagnetization refrigerator (ADR) as discussed in Chapter 4. We recall that in field-cooled measurements, we repeatedly heat up the cold-finger to ~ 1.5 K to exceed the aluminum film transition temperature $T_c \sim 2$ K to apply a different magnetic field with the Helmholtz coil. We then cooldown to 100 mK. Upon reaching 100 mK for each field-cooling point, we measure the microwave transmission S_{21} through the feedline using a vector network analyzer (VNA, model N5230A, 300kHz-20GHz). We perform the measurements of the transmission at sufficiently high powers, with $\sim 10^5$ photons in the resonator, to minimize the dissipation due to two-level defects on the surfaces and interfaces [17]. We have measured the fundamental resonance at 3.0713 GHz and the measured coupling quality factor is $Q_c = 765,000$, extracted from measured data following the fitting routine we described in Chapter 4. In zero-field cooled measurements, we measured the total quality factor $Q = 185,000$. This resonator is significantly under-coupled, the internal losses dominate the coupling losses as $1/Q = 1/Q_i + 1/Q_c$.

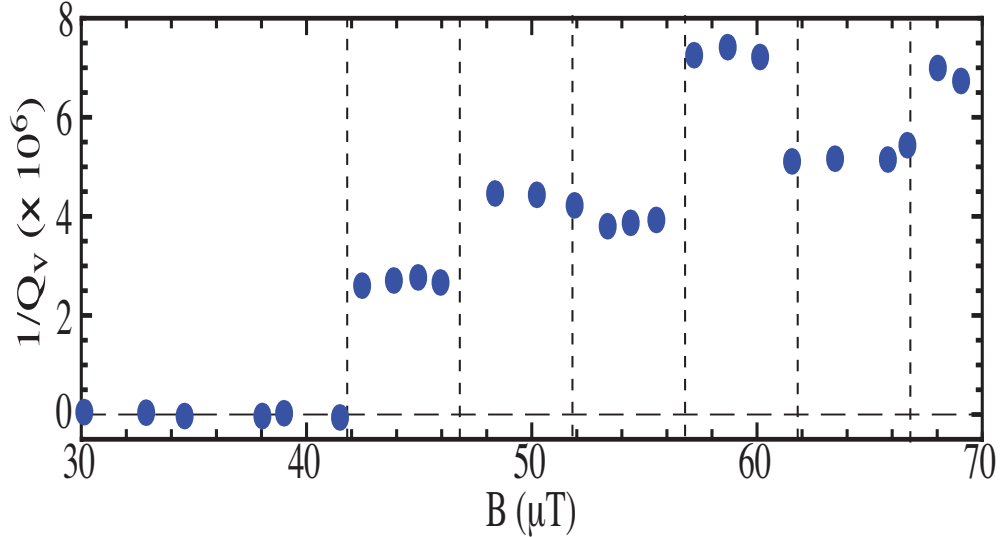


Figure 5.3: $1/Q_v(B)$ for fundamental resonance for cooling fields in the vicinity of $B_{th}(8 \mu\text{m})$ for the central bulge region. Vertical dashed lines correspond to field steps $\Delta B = 5 \mu\text{T}$. From Nsanzineza & Plourde, Phys. Rev. Lett. 113, 117002(2014) [3].

At each cooling field, we define the loss due to vortices as [66]

$$\frac{1}{Q_v} = \frac{1}{Q} \Big|_{B \neq 0} - \frac{1}{Q} \Big|_{B=0}. \quad (5.1)$$

That means we subtracted out the contributions from all the other loss mechanisms. In figure 5.3, we show the plot of vortex loss $1/Q_v(B)$ for fundamental resonance for various applied magnetic fields in the vicinity of the threshold field to trapping vortices in the bulge region. For sufficiently small B , we observe $1/Q_v = 0$ as there are no vortices trapped in the resonator. As we applied the magnetic field past the threshold field $42 \mu\text{T}$ corresponding to the width of the central bulge, we can observe the effect of single vortex trapped in the resonator through field cooling, from the plot we notice steps at regular field intervals. We can scale the flux quantum carried by a single vortex by the effective area of the central bulge and see that this field interval matches the steps in our measurements. In fact, if assume that each step is due to an increase in the number of vortices by one, we calculate the effective area for vortex trapping as effective area $= \Phi_0/\Delta B \approx 400 \mu\text{m}^2$ which matches with the bulge region in our resonator. We recall that $\Phi_0 = 20.7 \text{ G} - \mu\text{m}^2$ is the magnetic flux quantum.

Thus, the abrupt first step upwards in $1/Q_v$ we attribute it to the trapping of one vortex in the central bulge. This value of $B_{th}(8 \mu\text{m})$ for the central bulge is consistent with the vortex-trapping expression studied in reference [2]. As we further increase magnetic field, we observe a series of other steps spaced by $\Delta B \approx 5 \mu\text{T}$. a second vortex is trapped in the bulge, which is translated into the second step of the plot, the third vortex trapped in the bulge will give rise to a third step, and so on. When we keep increasing the magnetic field, in the end vortices are trapped everywhere,

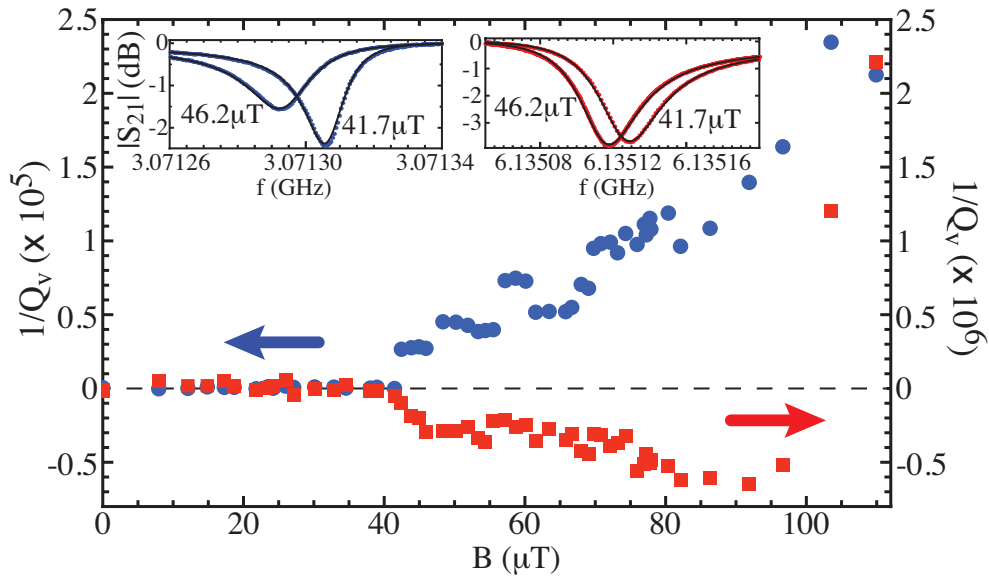


Figure 5.4: $1/Q_v(B)$ for fundamental (blue circles) and first harmonic (red squares) resonance – note different scales on loss axes. (insets) $|S_{21}(f)|$ for (left) fundamental; (right) harmonic for $B = 41.7 \mu\text{T}$ (no vortices) and $46.2 \mu\text{T}$ (one-vortex step). From Nsanzineza & Plourde, Phys. Rev. Lett. 113, 117002(2014) [3].

in the bulge and outside of the bulge, steps are washed out as we have many vortices, a rapid increase in the vortex loss with the field is observed (Figure 5.4). We notice that the step widths are quantized, but the step heights are clearly not constant as we would expect for the sequential addition of one vortex. Also, the sequential addition of one vortex does not always have the same sign, as we notice in the step from 4 to 5 vortices. In fact, the vortex loss $1/Q_v$ depends on the local current density that is not uniform across the width of the bulge as shown in figure 5.5. The current density is a minimum at the center of the conductor trace, and it is maximum along the edges. In the ground planes on either side of the bulge, the current density falls quickly from the edges of the gaps as shown in figure 5.5.

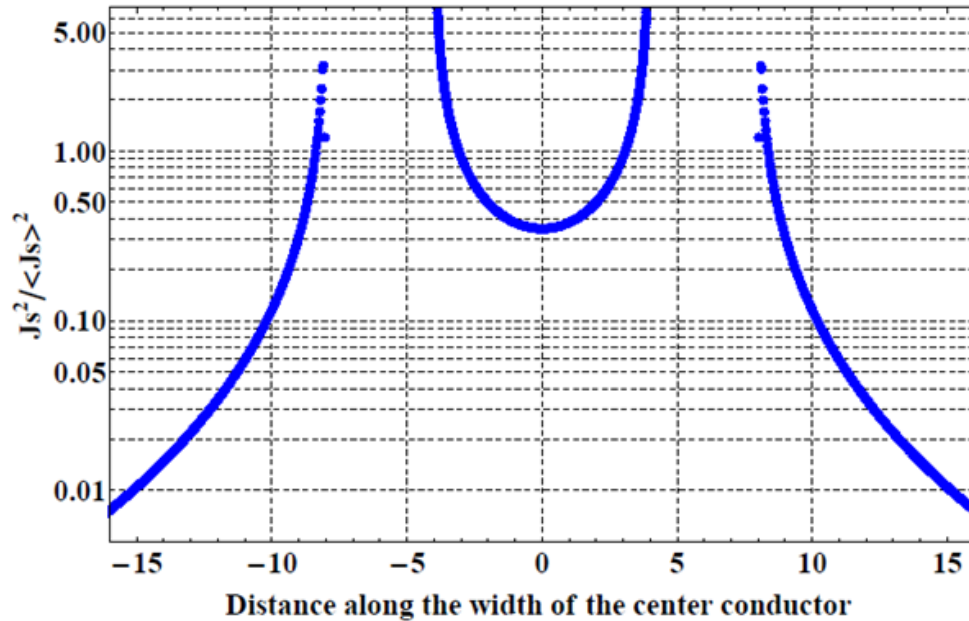


Figure 5.5: Variation of current density along the width of the conductor trace of in middle of resonator in the bulge region. The current density is minimum at center of the conductor trace, and it is maximum along the edges. In the ground planes on either side of the bulge, the current density falls quickly from the edges of the gaps. Calculations based on equation 3.22.

Therefore, we can say that vortices that are located near the edge of the bulge will contribute

more dissipation compared to a vortex near the centerline. In fact, the random pinning potential governs the positions of the vortices in the aluminum film. The distribution of vortices is also affected by the inter-vortex interactions that are present immediately below T_c when the vortices are still mobile before they become pinned somewhat further below T_c [107]. At our measurement temperature 100 mK, the penetration depth is less than 100 nm and we think that the vortices will no longer interact with one another. We can estimate an approximate loss per vortex using equation 3.25 for our aluminum film on this device. We obtained a value between $1 - 5 \times 10^{-6}$ depending on the vortex location along the width of the bulge region. Our estimate is consistent with the measured steps in $1/Q_v$.

In addition to measuring the vortex response for the fundamental mode of the resonator, we measured the first harmonic at 6.13513 GHz, with $Q_c = 341,000$. As we discussed above, this corresponds to a full-wavelength resonance with a current node at the middle of the resonator in bulge region. For the first harmonic, we expect no loss from vortices that are trapped in the bulge as there is no current to drive these vortices. Interestingly, our measurements of the vortex loss $1/Q_v$ for the first harmonic resonance show a decrease in the loss at the same $B_{th}(8 \mu\text{m})$ where we observed the first step upwards in the $1/Q_v$ for the fundamental mode (Figure 5.4). Thus, the quality factor for the first harmonic goes up as we trap vortices in the bulge.

The downwards trend for the first harmonic, although clearly visible, is not as sharp as the upwards step for the fundamental. The changes in the vortex loss $1/Q_v$ for the first harmonic are about one order of magnitude less than those on the fundamental. Any slight changes in the extracted loss, due possibly to fluctuations in the temperature of our ADR cryostat or variations in the electromagnetic environment for measuring the CPW resonator over the course of measurements, tend to smooth out small features in the vortex loss $1/Q_v(B)$ plot for the harmonic. The vortex loss $1/Q_v$ continues to decrease for larger applied magnetic fields until a field of $\sim 90 \mu\text{T}$. As we further increase the magnetic field, we started to observe a significant increase in vortex loss of the first harmonic. We associate this increase at large fields to vortices that begin to trap along the entire length of the resonator for $B > B_{th}(3 \mu\text{m})$, where there are significant microwave currents to drive the vortices. For applied magnetic fields $B > 110 \mu\text{T}$, the resonator internal losses due to the vortices is large compared to the coupling loss $1/Q_c$ and because of that we were not able to fit the data to get value for the quality factor Q .

5.3.1 Trapping vortices in the ground plane and reducing background quasiparticles density

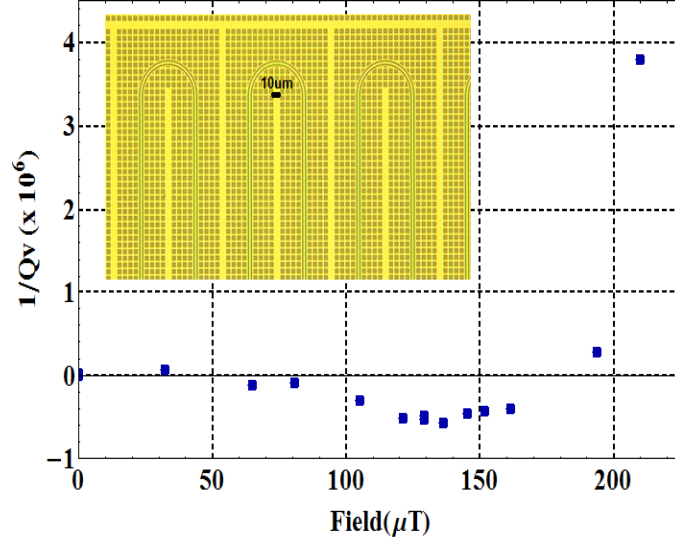


Figure 5.6: Vortex loss plotted as a function of applied magnetic field. Vortices trapped in ground plane at vanishing current density reduce quasiparticles density.

We have shown that we can reduce the background quasiparticles density by vortices located at vanishing current density in the resonator, resulting in an enhancement of resonator quality factor. We have performed field-cooled measurement to trap magnetic vortices in aluminum traces that are $10 \mu\text{m}$ wide (figure 5.6). We fabricated a sample with 150 nm -thick Aluminum. We designed aluminum traces to be at locations of vanished current density in the ground plane of the chip, at $\sim 35 \mu\text{m}$ far away from the center conductor of the resonator. For fields that are above the threshold field for trapping vortices in a $10 \mu\text{m}$ in ground plane but below the threshold for trapping vortices in the resonator center conductor (that is $4 \mu\text{m}$ wide), we observed an enhancement of resonator quality factor for a wide range of fields. This enhancement of quality factor is consistent with a decrease in background nonequilibrium quasiparticles originated from stray infrared radiation from warmer parts of the ADR cryostat, as discussed in detail in Chapter 6. Once vortices are trapped in the center conductor of the resonator at locations with nonzero local current density, the value of extracted resonator quality factor decreases as magnetic vortices contribute more loss, and hence a decrease in quality factor.

Chapter 6

Numerical simulations of reduction of density of nonequilibrium quasiparticles due to trapped vortices

6.1 Introduction

In chapter 5, we showed that there is dramatic difference in the effects of the first several trapped vortices on the various resonance mode that we excited. When the vortices are trapped near an antinode of the current standing-wave pattern, we observed a stepwise increase in the vortex loss. However, we have seen that vortices located near a current node contributed no extra dissipation, and, in fact, lead to an enhancement of the resonator quality factor.

We interpret the decrease in vortex loss $1/Q_v$ for the first harmonic resonance as a signature of a reduction in the loss due to nonequilibrium quasiparticles $1/Q_{qp}$ due to interactions between the quasiparticles and the vortex cores. As we pointed out in chapter 3, at millikelvin temperatures the density of thermal quasiparticles should be vanishingly small. However, because of nonequilibrium sources, the superconducting aluminum circuits can exhibit a significant excess of nonequilibrium quasiparticles with a typical volume density $n_{qp} \sim 10 - 100 \mu\text{m}^{-3}$ [23–25]. Blackbody photons emitted by warmer parts of the ADR cryostat, even at milliKelvin temperatures, can be sufficiently energetic to break Cooper pairs because aluminum films exhibit a relatively small value of the

superconducting energy gap. The quasiparticles dissipation $1/Q_{qp}$ increases as the density of quasiparticles rises. In this chapter we describe our numerical simulations of the reduction of the density of nonequilibrium quasiparticles due to trapped vortices.

6.2 Variation in loss with cryostat temperature

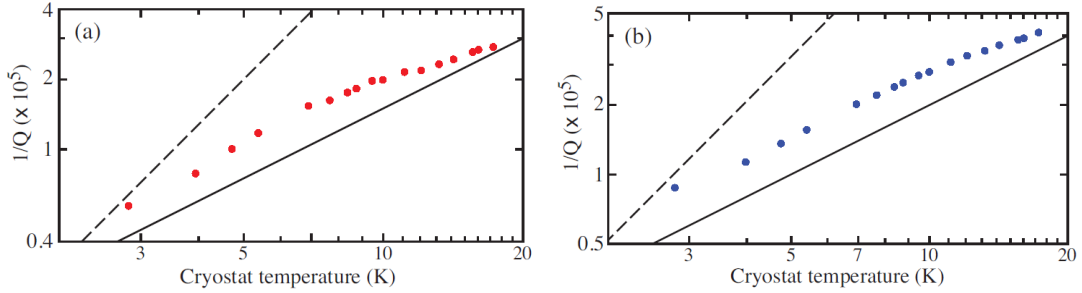


Figure 6.1: Measurements of $1/Q$ vs. cryostat temperature for zero-field cooling for (a) fundamental, (b) harmonic resonance. The temperature of the cold-finger and sample remained below 140 mK during the measurements. Dashed line is a guide to the eye for a quadratic dependence while the solid line corresponds to a linear dependence. From Nsanzineza & Plourde, Phys. Rev. Lett. 113, 117002(2014) [3].

Barends et al. [23] have performed experiments to investigate the effectiveness of different levels of infrared shielding of aluminum resonators, where the cryostat temperature on an ADR was increased while the cold-finger was maintained below 150 mK. With minimal shielding, comparable to our experimental setup, the high-power resonator loss was observed to increase with the cryostat temperature, as we would expect from a blackbody source.

We have performed a similar measurement to reference [23] for our standard sample shielding techniques to confirm the presence of a significant density of nonequilibrium quasiparticles in our resonators due to pair-breaking radiation from warmer parts of the cryostat. By changing the temperature of the cryostat, separate from the cold-finger and sample, one can change the radiation power and spectrum that is influencing the resonator. For this test, we cooled the resonator with no magnetic field applied with our Helmholtz coil to avoid trapping any vortices. By turning off the pulse-tube compressor with the sample at the base temperature, the pulse-tube stage warmed up, thus also warming the Helmholtz coil, magnetic shield, and 3 K thermal shield. Even once these components reached 18 K, the sample temperature increased no higher than 140 mK.

We recorded S_{21} along with the cryostat temperature during this warming process. In figure 6.1 we show the plot of the loss $1/Q$ for the fundamental and harmonic resonance vs. the ADR cryostat temperature. For both resonance modes, the loss increased significantly as the ADR cryostat

temperature was raised. For a blackbody source with the full spectrum of radiation shining on the resonator, one would expect $1/Q \propto T_{cryostat}^2$ according to reference [23].

For increased levels of IR shielding surrounding the sample, the radiation spectrum can be cut off, leading to smaller exponents for the increase [23]. Our observed increase in $1/Q$ is closer to linear rather than quadratic, suggesting that our brass sample box that encloses our resonator chip provides some attenuation of the IR radiation. The immediate increase in $1/Q$ with $T_{cryostat}$ strongly suggests that nonequilibrium quasiparticles due to stray IR radiation in our ADR cryostat dominate the loss in our CPW resonator measurements.

6.3 Quasiparticle diffusion equation

The interactions between quasiparticles and vortices have been reported previously, in the measurements of quasiparticle lifetime in aluminum films at low temperatures [26]. These studies were also performed in the experiments involving tunnel junction photon detectors [27] and Normal metal-Insulator-Superconductor (NIS) coolers [28]. All these experiments were carried out in the presence of a uniform distribution of many vortices. The superconducting energy gap gradually decreases in the vicinity of the vortex core, hence providing a pathway for quasiparticle relaxation and trapping. In reference [26], quasiparticles were injected with a tunnel junction at one end of an aluminum strip, and they diffuse along the strip. A second tunnel junction some distance away was used to measure the diffusion of the quasiparticles. When the magnetic field was applied, the density of quasiparticle reaching the detector junction was significantly reduced. Ullom et al. modeled this process by a diffusion equation with an addition of a recombination term that depends on the fraction of non-superconducting regions, related to the density of vortices in the aluminum film.

We consider a similar picture to model the quasiparticle diffusion in our CPW resonator, and we added discrete regions of enhanced recombination localized around each vortex in our simulations. We will consider one-dimensional diffusion equation model for quasiparticles, neglecting variations in the width of the center conductor of the resonator. We modify the diffusion equation to include a spatially-dependent enhanced recombination from the vortex. We focus on steady state solution, assuming that nonequilibrium quasiparticles are generated uniformly at a constant injection rate. We can take values of the diffusion constant and uniform background recombination rate for aluminum films from the literature, and we can then use the recombination rate parameter together with the measured value of internal loss when no vortex is present to estimate the generation rate for quasiparticles in our system. Our modified diffusion equation reads

$$D\nabla^2 n_{qp} - \Gamma_R n_{qp}^2 + \gamma_i - \Gamma_v n_{qp} e^{-(x-x_v^i)^2/l_v^2} = 0. \quad (6.1)$$

D is the quasiparticle diffusion constant, which varies with energy [26]

$$D(E) = D_n(1 - (\Delta/E)^2)^{1/2} \quad (6.2)$$

where D_n is the normal metal diffusion constant. The normal metal diffusion constant D_n directly affects D and there is a range of reported values of D_n for aluminum films, including $49 \text{ cm}^2/\text{s}$ [108] and $140 \text{ cm}^2/\text{s}$ [89]. Of course, such variations can be caused by different electronic mean free paths depending on the film quality in the various experiments.

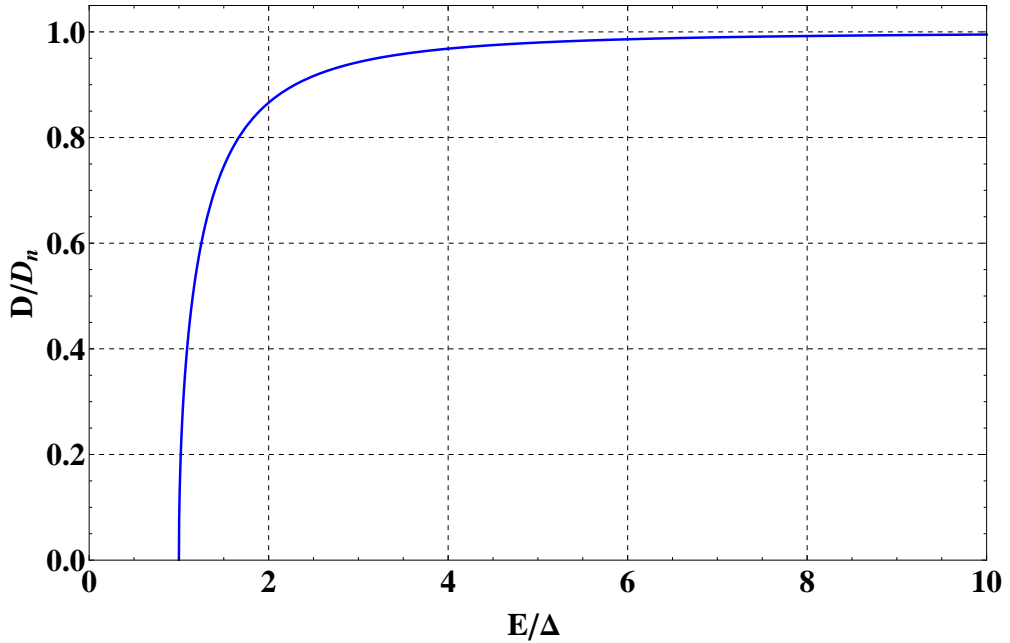


Figure 6.2: Variation of the quasiparticle diffusion constant with energy. The calculations are based on equation 6.2.

The diffusion constant $D(E)$ has the strongest variation for quasiparticles with energies that are just above the gap, Δ , while D only varies by $\sim 15\%$ for energies above 2Δ .

The Cooper-pair breaking radiation in our system is possibly originating from the 3 K shield and warmer regions of our ADR cryostat. Therefore, the significant part of this spectrum will lead to the majority of the nonequilibrium quasiparticles that have energies that are a few times Δ and above. Consequently, to simplify our analysis while still capturing the essential dynamics, we use $D = D(2\Delta)$. However, even after accounting for the reduction in D due to the quasiparticle energy, there is evidence that the effective D is typically reduced further still [109]. For our Al film, we estimate $D_n = 150 \text{ cm}^2/\text{s}$ based on the measured resistivity at 4 K of $0.5 \mu\Omega\text{-cm}$. In order to account for the anomalous reduction described in reference [109], we used $D_n = 60 \text{ cm}^2/\text{s}$, combined with an

estimate for the approximate quasiparticle energy, to determine D for the simulations presented in Figure 6.3(b).

Γ_R is the effective background quasiparticle recombination rate and is position-independent, and is calculated using the equation 2.40. However, the exact value of Γ_R depends on details of phonon trapping; we can estimate it based on the values extracted by others for aluminum thin films, but Γ_R can be constrained to $10 - 100 \mu\text{m}^3/s$ [26]. γ_i , which is also independent of position, is the quasiparticle generation rate due to photons. We adjust the value of γ_i to match the value of n_{qp} with no vortices present that we obtained from our measured $1/Q_i$ for zero-field cooling.

The last term in equation (6.1) represents the vortex- quasiparticle interaction, with the vortex centered at x_v^i , where the superscript i labels a particular vortex in the bulge. Γ_v corresponds to the rate of the quasiparticle trapping and relaxation in the vicinity of the vortex. Because the superconducting energy gap varies in the vicinity of the vortex core, this term should have a strong spatial variation to take into account the variation of gap energy near the vortex core. We have assumed a Gaussian profile for the vortex-enhanced recombination term with a length-scale of $l_v = 0.5 \mu\text{m}$. Our estimate is based on a the treatment in reference [27] of suppression of the gap in the vicinity of vortex using the Usadel equations with a prediction of an effective radius of $\sim 2.7\xi$. The qualitative outcome of our simulation would be the same if we used a different functional form other than Gaussian profile or if we used a different value for l_v , but this could impact the value of Γ_v that we extract from comparisons with our data.

We have solved equation 6.1 with MATLAB® using a numerical package involving piecewise Chebyshev polynomial interpolants [110]. In our simulation, we apply a damped Newton method iteratively with an adaptive mesh approach to deal with the sharp, micron-scale features in the vicinity of each vortex while solving the nonlinear differential equation over the entire $L = 17.1 \text{ mm}$ length of the resonator. Because the open-ended geometry of our resonator avoids quasiparticle out-diffusion from the center conductor, we apply the boundary condition $\partial n_{qp}/\partial x = 0$ at both ends. In our simulation of the field-dependence of the quasiparticle density $n_{qp}(x)$, for a particular magnetic field range we include one vortex term for each vortex in the distribution. From the analysis of the steps in $1/Q_v$ for the fundamental mode, we obtain the number of trapped vortices for each magnetic field range. Then we assign the position x_v^i for each vortex to space them evenly in the middle of the resonator in the central bulge region that is $50 \mu\text{m}$ long. For example, in our simulations with two vortices, $x_v^1 = -25 \mu\text{m}$ and $x_v^2 = +25 \mu\text{m}$. For a three-vortex case, $x_v^1 = -25 \mu\text{m}$, $x_v^2 = 0$ and $x_v^3 = +25 \mu\text{m}$. Figure 6.3 contains several resulting $n_{qp}(x)$ profiles for four different vortex configurations.

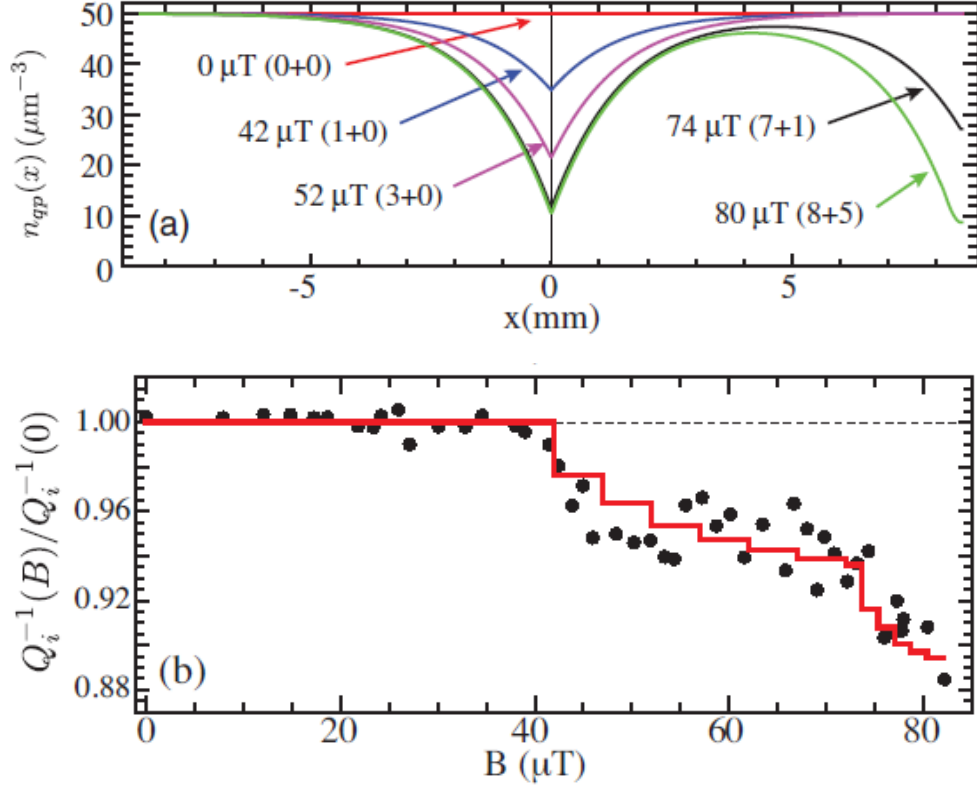


Figure 6.3: (a) Simulated $n_{qp}(x)$ for several example cooling fields. Labels indicate vortex number in central bulge + coupling elbow. (b) Measured $1/Q_i(B)$ for harmonic, normalized by average of $1/Q_i$ below threshold field (points); computed normalized quasiparticle loss on harmonic from simulated $n_{qp}(x)$ (solid line). From Nsanzineza & Plourde, Phys. Rev. Lett. 113, 117002(2014) [3].

At a cooling magnetic field of $72 \mu\text{T}$, following the addition of the sixth vortex to the central bulge, we notice a rapid decrease in $1/Q_v$ for the harmonic (Figure 6.3). We remind that the resonator elbow has a width equal to $6 \mu\text{m}$. The rapid decrease in loss corresponds to the intermediate threshold field $B_{th}(6 \mu\text{m})$ for trapping vortices in $6 \mu\text{m}$ -wide coupling elbow, which also corresponds to at a current node in the current density standing wave pattern. $B_{th}(6 \mu\text{m})$ is in between $B_{th}(8 \mu\text{m})$ for the bulge and $B_{th}(3 \mu\text{m})$ for the rest of the resonator. The area of the resonator elbow region is about three times larger than that of the central bulge. Therefore, beyond $72 \mu\text{T}$ we added one vortex to the elbow every $1.7 \mu\text{T}$, while continuing to add one vortex to the bulge region every $5 \mu\text{T}$. Note that for each vortex-number increment in our simulations, we have spaced the vortices evenly within each trapping region, and for each trapped vortex, we include a separate vortex-related terms in equation 6.1. However, we are unable to determine the precise location of each vortex within the bulge or elbow or in the elbow.

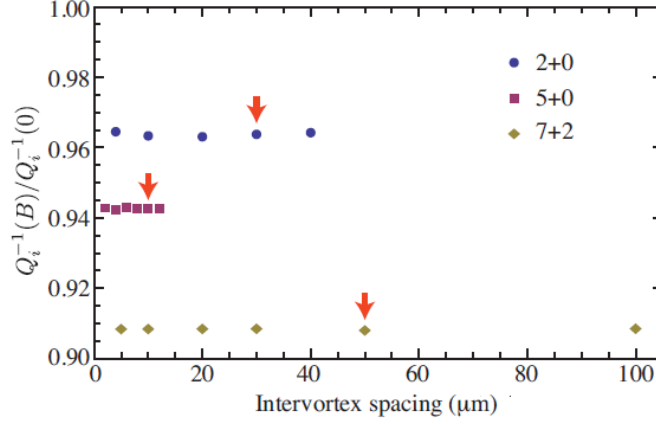


Figure 6.4: Simulated normalized quasiparticle loss on harmonic for different intervortex spacings for (i) 2 vortices in central bulge (circles), (ii) 5 vortices in central bulge (squares), (iii) 7 vortices in central bulge that are fixed in place plus 2 vortices in coupling elbow with variable spacing (diamonds). Red arrows indicate the intervortex spacing used in Figure 6.3(b). From Nsanzineza & Plourde, Phys. Rev. Lett. 113, 117002(2014) [3].

We verified that our simulated reduction in density of quasiparticles does not depend significantly on the detailed locations of each vortex in the distribution. In fact, we have chosen three example steps in the field-dependence from figure 6.3(b). We checked the simulations for three cases: (i) 2 vortices in the bulge and none in the elbow, (ii) 5 vortices in the bulge and none in the elbow, (iii) 7 vortices in the bulge and two in the elbow. And for each case we have repeated the simulation for several different values of the intervortex spacing, within the constraints of the size of the bulge and elbow. In figure 6.4, we show the variation in the simulated normalized quasiparticle loss on the harmonic with intervortex spacing for each of these three cases. The arrows indicate the spacing values that we used to the corresponding points in Figure 6.3(b). We observed that there was no significant dependence on the intervortex spacing. Therefore, we conclude that detailed knowledge of the vortex positions in the central bulge and coupling elbow is not necessary for our current modeling of the vortex-quasiparticle interactions.

We have compared the simulation results with our measured internal loss for the harmonic $1/Q_i(B)$. To do that, we take into account for the variation of the standing-wave current along the length of the resonator because the quasiparticles density $n_{qp}(x)$ is proportional to the local effective resistivity. We computed $\left(\int_{-L/2}^{L/2} I^2(x)n_{qp}(x)dx\right) / \left(\int_{-L/2}^{L/2} I^2(x)dx\right)$, where $I(x)$ is a full period of a sine wave for the harmonic, then we divide by the value of quasiparticles n_{qp} that we obtained from zero-field cooling measurements. We can compare this with the measured $1/Q_i(B)$ for the harmonic, normalized by the average of $1/Q_i(B)$ corresponding to all data we measured with for $B < B_{th}(8\mu\text{m})$. We then adjust Γ_v to get the closest agreement between the simulations and the

experiments.

	Simulation in fig 6.5 (a)	Simulation in fig 6.3 (b)	Simulation in fig 6.5 (b)
$D(\text{cm}^2/\text{s})$	30	60	150
$\Gamma_R(\mu\text{m}^3/\text{s})$	20	30	40
$\Gamma_v(1/\text{s})$	7×10^6	3.5×10^6	2×10^6

Table 6.1: The values of D , Γ_R , Γ_v from the three simulations in figures 6.3 and 6.5

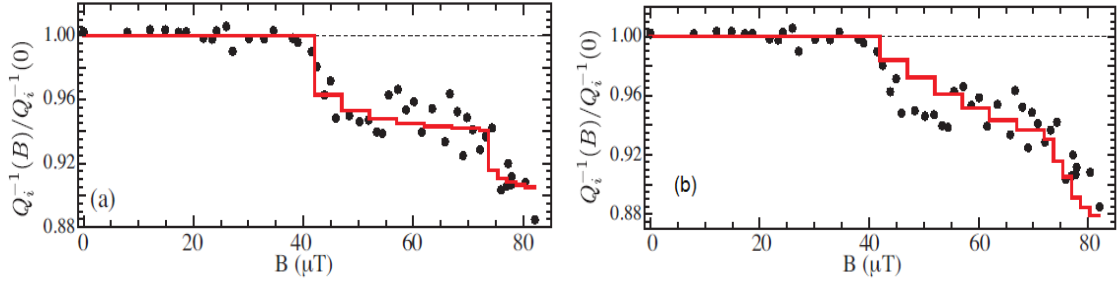


Figure 6.5: (Color online) Measured $1/Q_i(B)$ for harmonic, normalized by average of $1/Q_i$ below threshold field (points); simulations of normalized quasiparticle loss on harmonic for different parameters (solid line): (a) $D = 30 \text{ cm}^2/\text{s}$, $\Gamma_R = 20 \mu\text{m}^3/\text{s}$, $\Gamma_v = 7 \times 10^6 \text{ s}^{-1}$; (b) $D = 150 \text{ cm}^2/\text{s}$, $\Gamma_R = 40 \mu\text{m}^3/\text{s}$, $\Gamma_v = 2 \times 10^6 \text{ s}^{-1}$. From Nsanzineza & Plourde, Phys. Rev. Lett. 113, 117002(2014) [3].

We have found that $\Gamma_R = 30 \mu\text{m}^3/\text{s}$, which is consistent with earlier work for aluminum films [26], combined with $\Gamma_v = 3.5 \times 10^6 \text{ s}^{-1}$ provides a good match with the experiment [Figure 6.3(b)]. The value of Γ_v that we obtained from the simulations is in the range of typical electron-phonon scattering rates for aluminum thin films at low temperatures [111, 112] while it is likely that electron-electron scattering in the vicinity of the vortex core may play a role as well [26]. Our simulations of the quasiparticles n_{qp} in the presence of vortices produce a reasonable qualitative description of our internal loss measurements on the harmonic, they do not provide a perfect match to the data. For example, the initial decrease in internal loss $1/Q_i$ for the harmonic with the very first few trapped vortices is not as rapid in our simulations compared to our experiment. We have explored the sensitivity of our model to the value of D used in the simulations by running our simulations from figure 6.3(b) for different values of diffusion constants. We choose two values of D_n : 30 and $150 \text{ cm}^2/\text{s}$ (figure 6.5). In each case, we adjusted the values of Γ_R and Γ_v to give the best agreement between the simulated curve and the normalized measured loss vs. field for the harmonic. The resulting values in the table above.

We found that for smaller D_n , we obtained the best match to the data for smaller Γ_R and larger

Γ_v . Therefore, our simulation model of the quasiparticle diffusion and interaction with vortices can provide a reasonable description of our experimental measurements over a range of parameters for quasiparticle dynamics, consistent with the variation in values for quasiparticle dynamics in aluminum films reported in the literature.

6.4 Conclusion

Using a variable-linewidth geometry for a weakly coupled resonator, we observed the effects of a single vortex trapped in the resonator through field cooling. For resonant modes where the vortex is near a current antinode, the presence of even a single vortex leads to a measurable decrease in the quality factor. For modes with the vortex located at a current node, the presence of the vortex results in no detectable excess loss and, in fact, produces an increase in the quality factor. We attribute this enhancement to a reduction in the density of nonequilibrium quasiparticles in the resonator due to their trapping and relaxation near the vortex core. In our simulation we used a modified diffusion equation with discrete regions of enhanced recombination localized around each vortex. We treat the diffusion process in 1D, neglecting variations in the width of the center conductor of the resonator and we were able to obtain good agreement between simulations of this simple quasiparticle diffusion model and our measured loss vs. cooling field data.

Chapter 7

Resonator response against direct quasiparticle injection

In this Chapter we describe further efforts to understand the dynamics of nonequilibrium quasiparticles in the superconducting coplanar waveguide resonators. We want to explore further the reduction of quasiparticle loss by vortices. In addition to the constant background non-equilibrium quasiparticle density, which comes from stray light from warmer parts of the cryostat breaking Cooper pairs in the film, we intentionally inject quasiparticles at a constant injection rate by using the normal metal-insulator- superconductor, NIS junction that is connected to the ground plane on the chip. We introduce the NIS junction, and we describe our measurements of quality factor as a function of injected power, and we define the loss due to quasiparticles.

7.1 Introduction to NIS tunnel junction

Normal-Insulator-Superconductor (NIS) junctions are formed by normal metal and superconducting electrodes separated by a thin insulator. Their applications are based on the existence of the Bardeen-Cooper-Schrieffer (BCS) energy gap Δ in the density of states of the superconductor. One of the useful properties of NIS junctions is in the study of quasiparticles dynamics in aluminum resonators. A current through a NIS junction creates quasiparticles in the superconducting resonator ground plane; some quasiparticles can enter directly into the center conductor of the quarter-wave resonator as it is connected to ground plane. Phonons from recombining quasiparticles can enter and travel through the silicon substrate and eventually reach the center conductor of the half-wave resonator. For an ideal NIS junction, there is no single-electron current flow through the NIS junction at

low temperature as long as the absolute value of bias voltage $|V|$ is smaller than Δ/e , with Δ the superconducting energy gap. In this chapter we present our measurements in which we look at microwave resonator response when we inject nonequilibrium quasiparticles using NIS tunnel junction.

7.2 Sample fabrication

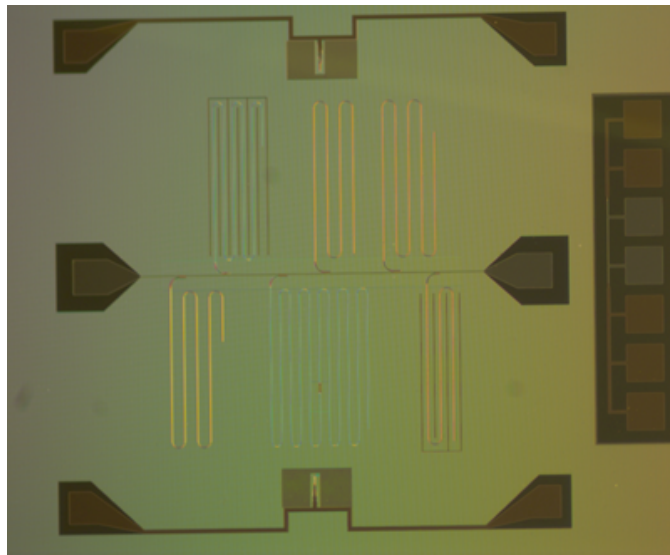


Figure 7.1: Optical photograph of the sample with 6 resonators coupled along same feedline. The sample include two Cu/AlO_x/Al junction with Copper traces used to inject Quasiparticles into the ground plane of chip.

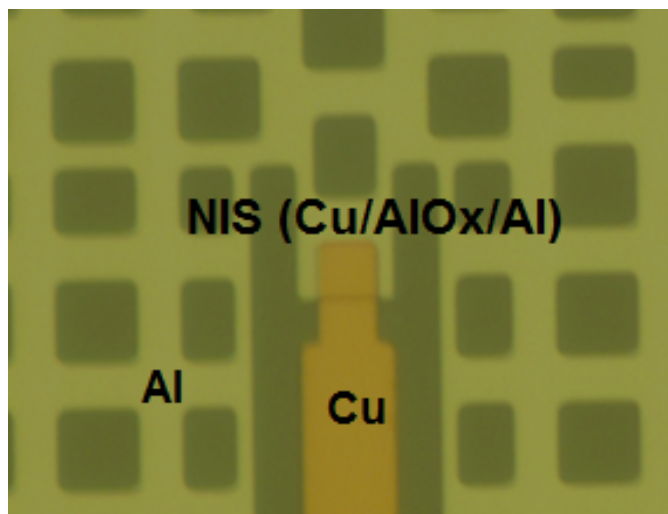


Figure 7.2: Copper-Aluminum oxide-Aluminum junction with overlap area of $5 \times 5 \mu\text{m}^2$.

We designed our chip to include an NIS junction and the current and voltage leads that we needed. The chip has two junctions. In the data we present here, we measured only one junction. Our NIS junction is made of copper (normal metal), aluminum oxide (insulator) and superconducting aluminum film, $\text{Cu}/\text{AlOx}/\text{Al}$. The overlap area of the junction is $5 \times 5 \mu\text{m}^2$. The fabrication process is a two-layer process. In the first layer, we use optical lithography to pattern resonators, followed by wet etch, the film thickness we used is 150 nm. In the second layer, after patterning photolithography we perform in-situ gentle ion-mill the copper traces and junction area followed by evaporation of a very thin layer of aluminum that is oxidized to make AlOx insulating layer on top of the aluminum. With the wafer still loaded in evaporation chamber at a high vacuum, we then evaporate copper on top of AlOx layer followed by lift-off. Note that during the fabrication of second layer, the resonator and some parts of the ground plane are covered with resist. The optical image of the sample and a zoom-in image of the $\text{Cu}/\text{AlOx}/\text{Al}$ junction is shown in figure 7.2. The copper thickness is chosen in such a way that we have a nice overlapping at the junction area. The thickness of copper we used is ~ 100 nm

7.2.1 I-V characteristics of the NIS junction

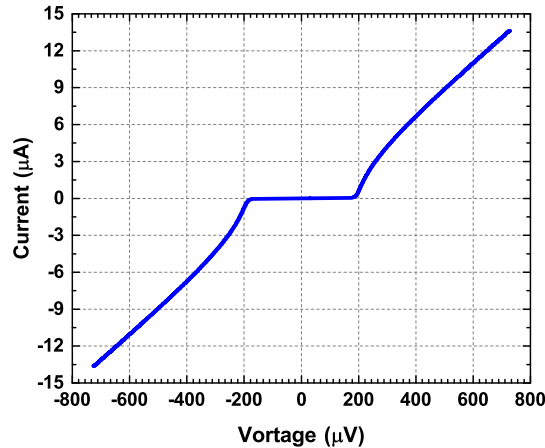


Figure 7.3: Current-Voltage (I-V) characteristics of $\text{Cu}/\text{AlOx}/\text{Cu}$ junction. The normal state resistance of the junction is $\sim 50 \Omega$, and the superconducting energy gap is $\Delta \sim 200 \mu\text{eV}$. Data was taken at 100 mK.

Our measurement setup is described in section 4.4. First we measured the current-voltage characteristics of the normal-insulator-superconductor tunnel junction by biasing the device with a current source and reading out the voltage with a room temperature pre-amplifier. We use a three-point technique for the I-V measurement. The current passes through the junction and goes to the ground

plane of the resonators. We then measure the voltage across the NIS junction on the same sample's ground plane. For the current line, we added a $100\text{ k}\Omega$ resistor at 3 K stage, and an ecosob filter at the cold-finger. On the dc voltage line that we use for reading out the voltage across the junction, we have added $5.6\text{ k}\Omega$ at 3 K stage, and also an ecosob filter at cold-finger. We cooled down using ADR and measured our sample at 100 mK. The energy gap of the superconductor electrode is $\Delta \sim 200\text{ }\mu\text{eV}$. The measured normal-state resistance of the junction turned out to be $50\text{ }\Omega$. In figure 7.3, we notice that our NIS junction behaved well. In fact, no current tunnel through the junction until the voltage across the junction has reached a value close to the gap energy $\Delta \sim 200\text{ }\mu\text{eV}$.

7.2.2 Dependence of resonator quality factor on tunneling power

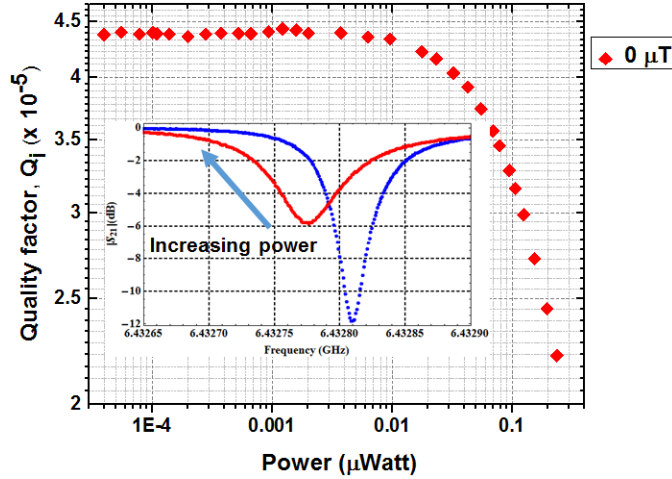


Figure 7.4: Resonator internal quality factor measured at different NIS injection powers in zero magnetic field. Insert: Magnitude of complex transmission S_{21} as function of frequency for two different injection powers (power = current \times voltage).

We have performed resonator measurements for different quasiparticles injection powers (injected current times measured voltage across junction). Quasiparticles are injected into an Aluminum superconductor using the NIS tunnel junction. These excitations diffuse throughout the sample's ground plane and eventually reach the resonator center conductor. We measured the resonator response for each injection power utilizing the same measurement techniques as detailed in chapter 4. We measure the complex transmission S_{21} by recording its magnitude and phase for reasonably high resonator internal power ($\sim 10^5$ photons in the resonator) and frequency span using vector network analyzer. With our 4-parameter fitting routine, we extract the resonator parameters (Q_i , Q_c , f_0). We have performed resonator measurements for different quasiparticles injection powers (injected

current times measured voltage across junction). Quasiparticles are injected into an aluminum superconductor using the NIS tunnel junction. These excitations diffuse throughout the sample's ground plane and eventually reach the resonator center conductor. We measured the resonator response for each injection power utilizing the same measurement techniques as detailed in chapter 4. We measure the complex transmission S_{21} by recording its magnitude and phase for reasonably high resonator internal power ($\sim 10^5$ photons in the resonator) and frequency span using vector network analyzer. With our 4-parameter fitting routine, we extract the resonator parameters (Q_i , Q_c , f_0).

7.2.3 Effects of vortices on the quasiparticles loss

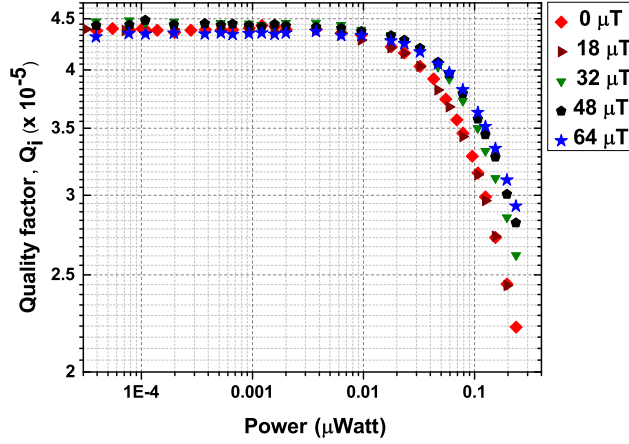


Figure 7.5: Resonator internal quality factor measured at different NIS injection powers and magnetic fields.

We have measured the resonator response against direct quasiparticles injection at different injection powers for various applied magnetic fields. For each plot in figure 7.6 we define the loss due to injected quasiparticles as

$$\frac{1}{Q_{qp}} = \frac{1}{Q_i} \Big|_{P \neq 0} - \frac{1}{Q_i} \Big|_{P=0}. \quad (7.1)$$

Therefore, the quasiparticles loss in the resonator is given by the total resonator internal loss for nonzero injected NIS power by subtracting off the internal resonator loss measured at zero power. We therefore simply subtract off all other loss mechanisms such as dielectric loss, coupling loss, radiation loss or loss from trapped magnetic vortices. In figure 7.6, we plot the quasiparticles loss as a function of injected NIS power.

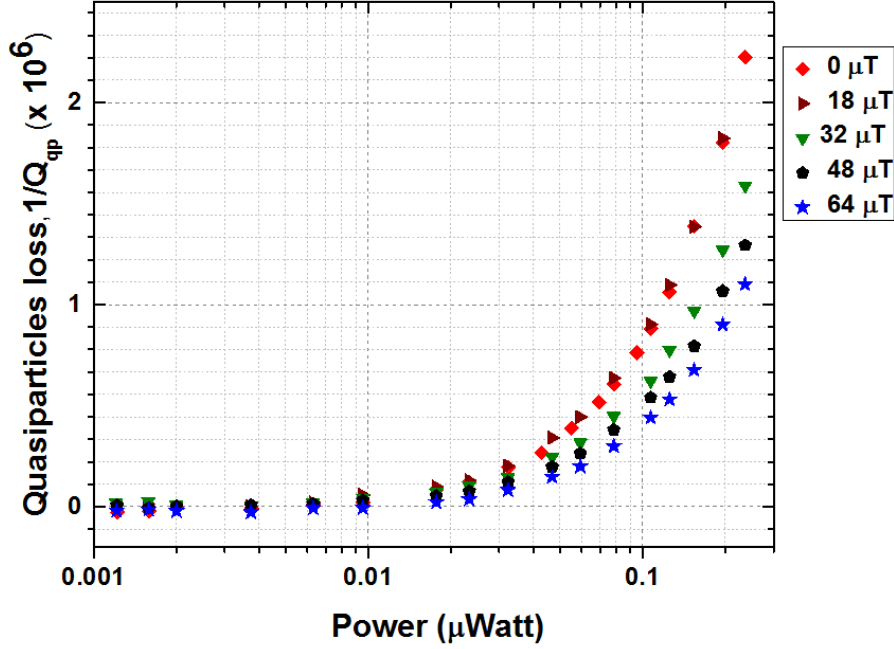


Figure 7.6: Quasiparticles loss measured at different NIS injection powers and magnetic fields.

The quasiparticles loss increases as we increase NIS injection power. The increase in quasiparticles loss with injected power is reduced when we perform the measurements with the vortices trapped in the ground plane and the center conductor of the resonator. As we increase the injection power, the density of injected quasiparticles also increases. The quasiparticles density n_{qp} is related to the loss due to quasiparticles in a superconducting microwave resonator via the equation 3.20.

$$\frac{1}{Q_{qp}} = \left(\frac{\alpha}{\pi} \sqrt{\frac{2\Delta}{hf_0}} \frac{1}{D(E_F)\Delta} \right) n_{qp}. \quad (7.2)$$

For the applied magnetic field that are greater than the threshold field for trapping the vortices in the $10 \mu\text{m}$ wide aluminum traces, the quasiparticles loss decreases as we increase vortex density in the ground plane. Moreover, we observe further decrease in quasiparticles loss when vortices start to appear in the $4 \mu\text{m}$ wide center conductor of the resonator. The increase in loss due to the injection current indicates an interplay of diffusion at energies well above the gap, scattering, and trapping in the vicinity of the vortex core.

7.3 Effects of cuts in the ground plane on the quasiparticles loss

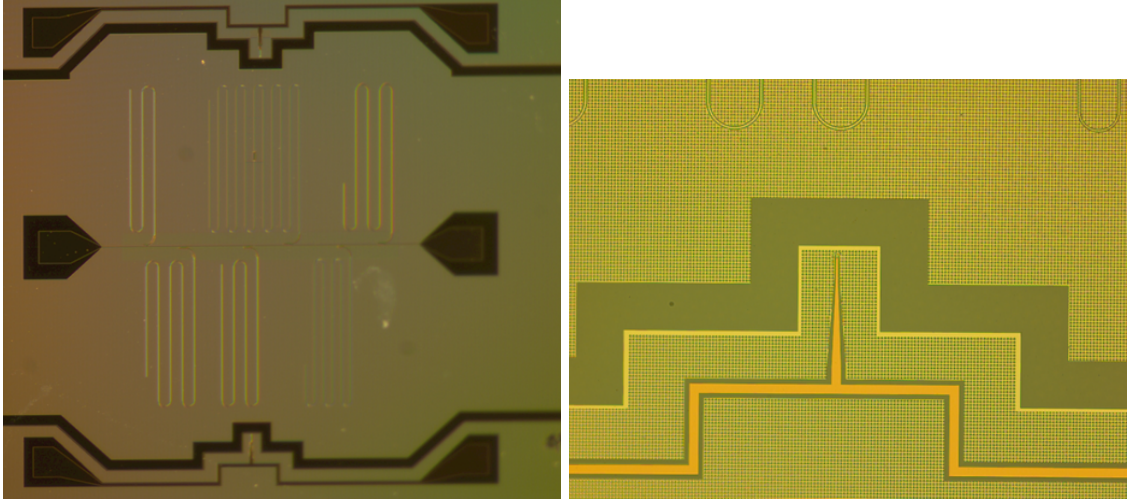


Figure 7.7: Left: Optical image of a chip with a cut in the ground plane of the chip. Right: Zoomed image optical image to aluminum strips that are designed to trap quasiparticles at edge of the ground plane of NIS.

In the experiments with a chip with a continuous ground plane, we found that the quality factor of half-wave resonator decreases as we inject more and more nonequilibrium quasiparticles. The half-wave resonator is not shorted to ground, therefore, the only way quasiparticles diffusing in the ground plane can reach to the resonator is through recombination. Two quasiparticles recombine and emit a 2Δ phonon. This phonon can travel through the silicon substrate and reach the center conductor of the resonator, hence and can break the Cooper pair. As more phonons reach the resonator center conductor of the resonator and break Cooper pairs, the quality factor of the resonator should decrease.

We have performed experiments using a device that has a cut in the ground plane to test the loss due the phonons that break Cooper pairs. The cut is $100\ \mu\text{m}$ wide and separates the ground planes of the resonators from that of NIS-tunnel junctions. Therefore, injected quasiparticles will not directly diffuse to the resonators. Along the edge of the cut, in the ground plane of the junction, we added aluminum strips to slow down quasiparticle recombination (7.7).

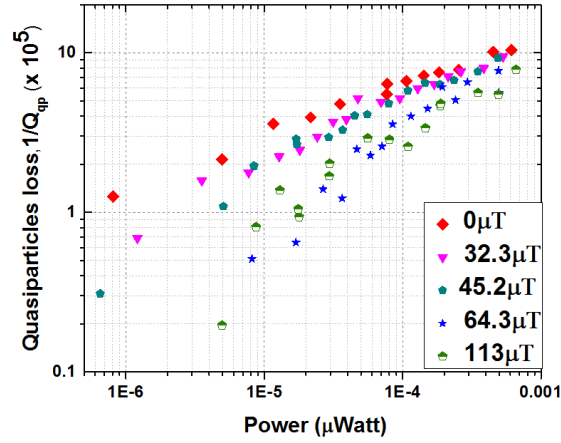


Figure 7.8: Quasiparticles loss a function of injected quasiparticles in NIS junction ground plane, for various magnetic fields.

In figure 7.8, we observed that, although we physically disconnect the ground planes of the NIS junction to that of resonators, nonequilibrium quasiparticles can still diffuse and reach to the devices, by recombination and then Cooper-pair breaking process. Furthermore, in this experiment we observe that with vortices trapped at the edge of the cut on same side as the NIS junction, the quasiparticles loss is lower when vortices are present. Which means many of the quasiparticles that are injected through the junction scatter or relax their energies in the vicinity of the vortex core before they can recombine to produce phonons.

Chapter 8

Nonlinear microwave response of vortices

In this chapter, we present the experiments of the vortex nonlinearity at microwave frequencies, a regime yet to be explored. All previous measurements of the Larkin-Ovchinnikov nonlinearity have all involved dc measurements; we are not aware of experiments looking at this nonlinearity for microwave driving of the vortices. When vortices are subject to a microwave drive, instead of a uniform net flux flow, they will oscillate back and forth with a quite small amplitude (of the order of nm) about their equilibrium positions. Nonetheless, when they cross this equilibrium position (twice on each cycle) they will be traveling at their maximum velocity, which could in principle approach the critical velocity v^* , where one would again expect to see the Larkin-Ovchinnikov nonlinearity play a role. We introduce the Larkin-Ovchinnikov nonlinearity and then we describe our device we used to study the vortex nonlinearity. We show the results of our measurements of power dependence of internal quality factor for various magnetic fields. We show how the vortex loss depends on the microwave driving power.

8.1 Larkin-Ovchinnikov flux-flow nonlinearity

Magnetic vortices in type-II superconductors can move under the action of the Lorentz driving force \mathbf{F}_L that is proportional to a current density \mathbf{J} . If there is no vortex pinning present, a constant Lorentz force will result in the free flux-flow of vortices. The vortex flux flow is characterized by a balance between Lorentz force $j\Phi_0$ and viscous drag force ηv where η is the coefficient of viscosity, v the vortex velocity and Φ_0 is the flux quantum. In this linear-response regime $j\Phi_0 = \eta v$, the

vortex velocity is proportional to the current driven through the superconductor and the viscous coefficient and the conductivity are constant [67]. At high vortex velocities, a nonlinear flux-flow behavior due to the nonequilibrium distribution of quasiparticles in the vicinity of the vortex core was predicted in 1980 by Larkin and Ovchinnikov [113]. When the vortex moves, the electric field that develops across the vortex core accelerates quasiparticles in the inside of the vortex core. Once these quasiparticles have gained enough energy from the electric field, they escape from the vortex core and can diffuse into the surrounding superconducting region. The reduction of quasiparticles from the vortex results in a reduction of the vortex viscosity, and thereby in an increase of the flux-flow velocity. Larkin and Ovchinnikov considered a uniform distribution of quasiparticles to study the instability of vortex motion caused by the change in the quasiparticles distribution near the vortex core. They showed that the non-linear flux flow viscosity $\eta(v)$ and the critical velocity v^* at which the flux flow instability occurs are related as

$$\eta(v) = \frac{\eta(0)}{1 + (v/v^*)^2}, \quad (8.1)$$

where $\eta(0)$ is the viscous damping coefficient at zero vortex velocity. The magnetic and temperature dependence of the critical velocity v^* has been studied extensively via DC measurements of Current-Voltage (I-V) characteristics [68, 114–117]. The LO theory was extended to include these dependencies and the vortex critical velocity v^* takes the form [68, 118]

$$v^* = \left(\frac{\phi_0 \Delta(T)}{\eta(0) \tau_E(T)} n_{qp} \right)^{\frac{1}{2}} B^{-\frac{1}{2}}, \quad (8.2)$$

where n_{qp} is the quasiparticles number density in the vortex core. Therefore, the critical velocity varies with the magnetic field as $v^* \sim B^{-\frac{1}{2}}$ and it also changes with temperature and quasiparticles relaxation time as $v^* \sim [(1 - T/T_c)^{1/2} / \tau_E(T)]^{1/2}$. Pinning strength also influences the vortex dynamics, particularly the vortex critical velocity, v^* decreases as the pinning strength increases [119–122]. The vortex critical velocity goes up as the thickness of the superconducting material is reduced [123].

8.2 Sample design

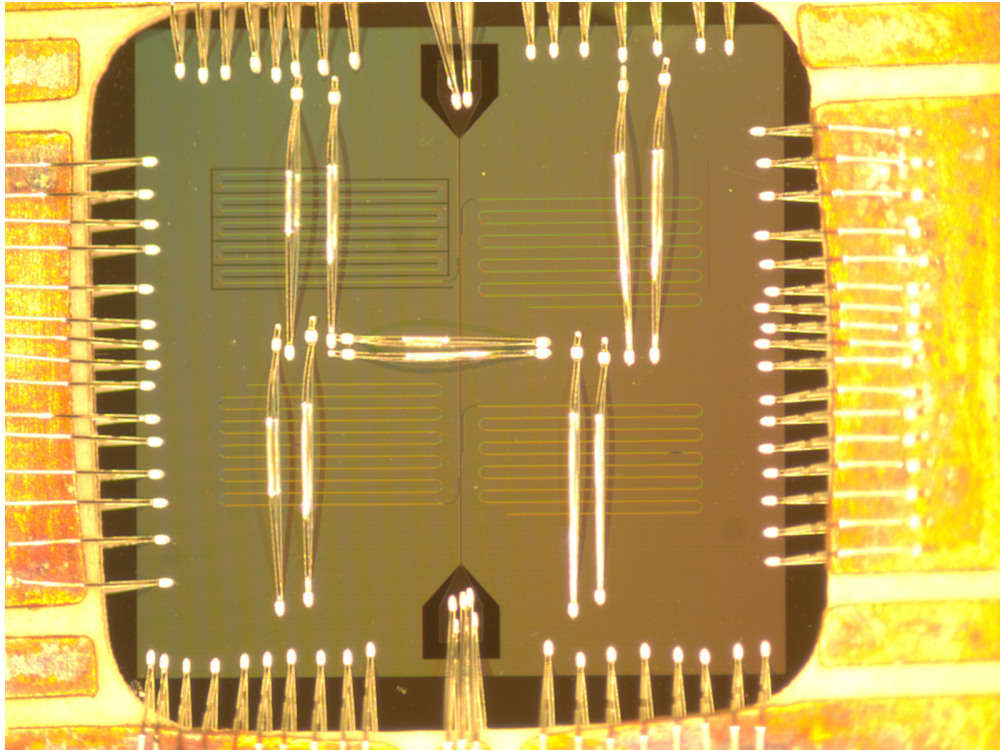


Figure 8.1: Chip wirebonded on a printed circuit board. To minimize unintended spurious transmission modes, we added some interconnections across each resonator and across the feedline.

We use the microwave resonators to study the power dependence of vortex loss and focus our discussion on the high microwave powers where we observed the vortex nonlinearity. We evaporated 65 nm-thick aluminum on an ion-milled silicon wafer, and we fabricated the resonators with the ASML 300C DUV Stepper at Cornell NanoScale Science and Technology Facility, using our fabrication techniques as we described in Chapter 4. The wafer was diced, and a chip was wire bonded using a PCB as shown in figure 8.1. The measured coupling quality factor of resonator we describe in this chapter is $Q_c \sim 250000$.

8.3 Power dependence of internal loss at various applied magnetic field

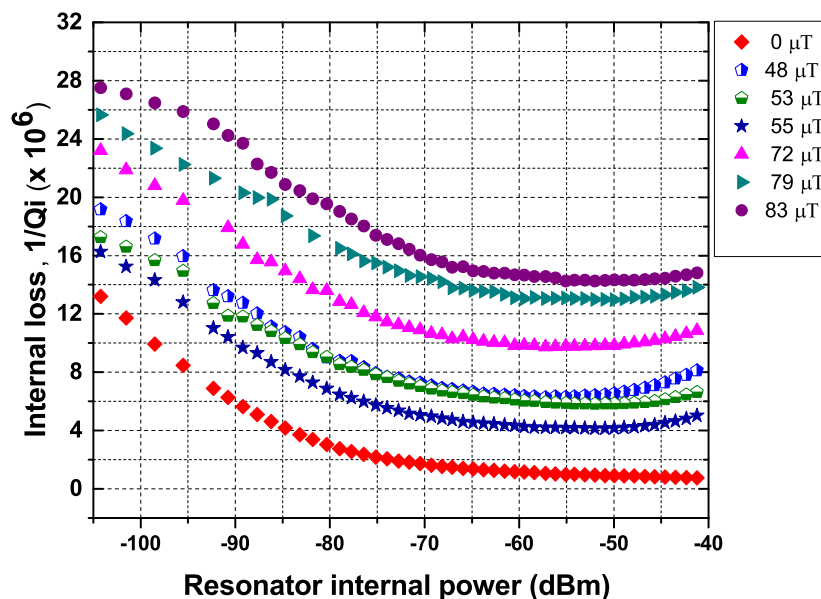


Figure 8.2: Plot of resonator internal loss as function of internal power for various magnetic fields.

We have explored the vortex response in an aluminum film at low temperatures and at microwave frequencies. For the CPW resonators being driven at high microwave powers in the presence of vortices, we expect that the effect of Larkin-Ovchinnikov nonlinearity would be an increase of the microwave loss. In our measurements, we have never gone to high enough powers where we see the instability and an abrupt transition out of the Superconducting state.

Using the vector analyzer we record the magnitude and phase of the complex transmission S_{21} for a wide range of microwave readout powers and we fit calibrated data in complex plane using a 4-parameter fitting model to get the resonator parameters f_0 , Q_c , and Q_i . As we described in section 4.4.2, for each readout microwave power from the input of the vector network analyzer we extract the internal power inside the resonator using the equation 4.11. We performed these measurements on various magnetic fields, each field being applied when the sample temperature is larger than the transition temperature. We applied field corresponding to one, two, three, or more vortices trapped in the bulge region in the middle of the resonators; we also performed power dependence measurements where we trap vortices everywhere in the volume of the resonator. In figure 8.2 we

plot the internal loss a function of resonator internal power for various applied magnetic fields. In zero-field-cooled measurements, the internal loss goes up as we decrease the resonator internal power. We also noticed similar behavior at low powers when we perform power dependence measurements of internal loss with vortices trapped in the resonator. Nonlinearity signatures occur at high powers for measurements with vortices trapped in the resonator. This nonlinear behavior is due to vortices being driven by the high microwave powers. Vortices oscillate around their mean position, and induce electric field which accelerates the bound quasiparticles in the inside of the vortex core. The quasiparticles escape the vortex core once they have gained enough energy, resulting in a reduction of vortex viscosity, and hence the vortex velocity increases. In our experiments, the increase in vortex velocity shows up as an increase in vortex loss at high power drive. Therefore, the power dependence of the loss is due to nonlinear viscosity.

8.4 Dependence of vortex loss on microwave power

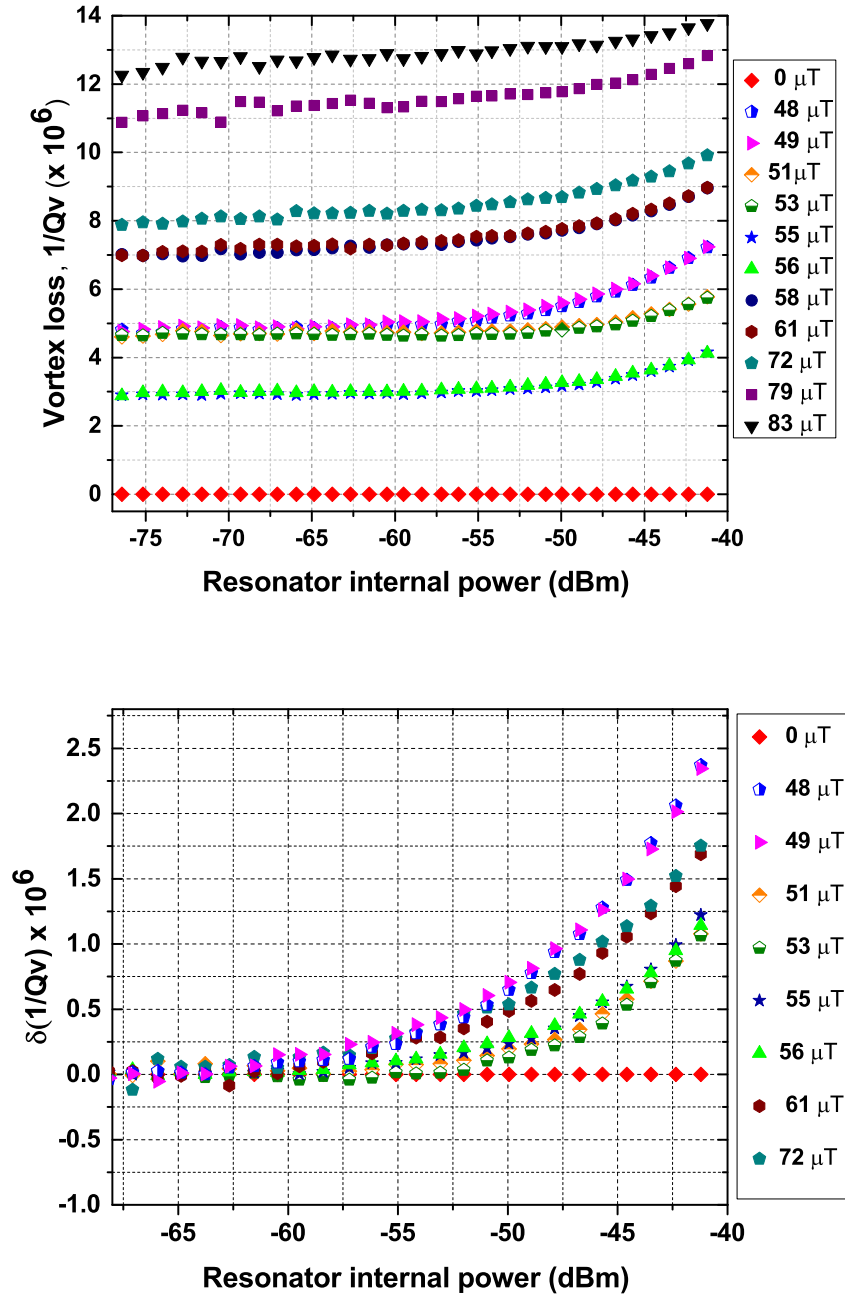


Figure 8.3: Plot of vortex loss and change of vortex loss as function of internal power for various magnetic fields.

We define the vortex loss as $1/Q_v = 1/Q_i(B) - 1/Q_i(B = 0)$ [66], therefore subtracting off other loss mechanisms such as loss from TLS systems, radiation loss, coupling loss, quasiparticles loss. For each plot in figure 8.2 measured at a different field-cool, we subtract off the internal loss measured in zero field-cool, and we do subtraction point by point at same internal power for field-cool and nonzero field-cool measurements. The internal power is function of total Q and Q_c as we explained in section 4.4.2, we use interpolation function to find $1/Q_i(B = 0)$ for each measured internal power. We then make a plot of vortex loss and change of vortex loss as a function of internal power in the resonator as shown in figure 8.3. Below the threshold field $B_{th} \sim 42 \mu\text{T}$ for trapping the vortices in the middle of the resonator, vortex loss is zero for all internal powers. For the power dependence measurements with vortices, the vortex loss is power-independent at low powers. At very high microwave powers, the change in vortex loss increases as we increase the resonator internal power.

8.5 Conclusion

We have measured the power dependence of resonator quality factor at various applied perpendicular magnetic fields. For each applied magnetic field, we extracted the vortex loss as a function of internal power in the resonator. We observed that vortex nonlinearity occurs at very high microwave powers at which the vortex viscosity decreases, resulting in an increase of vortex velocity, and hence an increase in vortex loss.

Chapter 9

Ongoing measurements, future directions, and conclusion

9.1 Ongoing measurements and future directions

Reduction of quasiparticle density with metal traps

We are currently exploring other methods to reduce the density of nonequilibrium quasiparticles. Because the superconducting energy gap decreases in the vicinity of the vortex and vanishes at the center of the vortex core, quasiparticles can scatter and relax their energy at these regions of reduced or vanishing energy gap. Therefore, as an alternative to trapping vortices in the superconductor, we can artificially engineer some regions of reduced energy gap in the superconducting coplanar waveguide resonators to trap nonequilibrium quasiparticles and hence, the loss due to quasiparticles will be reduced. To make regions of reduced energy gap we are using bilayer film of copper and aluminum. We want to make small regions that have this bilayer structure, while most of the circuit remains aluminum as before. We apply our knowledge from the vortex-quasiparticle experiments to determine how big the normal metal traps should be and where they should be located.

we use the fact that the transition temperature of a bilayer film can be lowered by appropriate choice of the thicknesses of the bottom and top film. Martinis et al. [124] have derived a model for the transition temperature in a normal-superconductor bilayer film using the microscopic-based Usadel theory [125, 126], and proposed the following expression for the transition temperature

$$T_c = T_{c0} \left[\frac{d_s}{d_0} \frac{1}{1.13 (1 + 1/\alpha)} \frac{1}{t} \right], \quad (9.1)$$

where t is a transmission factor that depends on the details of the interface layer, and it takes a value of order of one for most clean metals and interfaces. $1/d_0 = (\pi/2)k_B T_{c0} \lambda_f^2 n_s$ and $\alpha = d_n n_n / d_s n_s$ where d_n and d_s are the thickness of the normal and superconducting films, respectively. n_n and n_s are the density of electronic states in the normal and superconducting films. $\lambda_f = 0.478$ nm is the Fermi wavelength for copper.

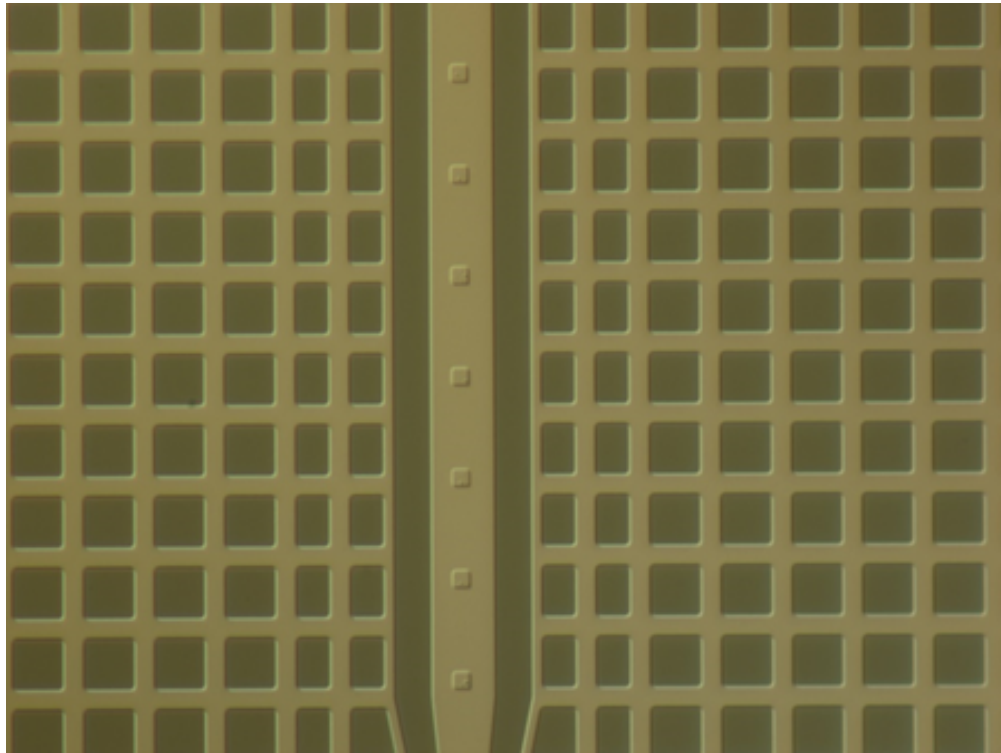


Figure 9.1: Copper traps engineered in the middle of the center conductor of resonator.

We have used a Matlab routine, developed by John Martinis group at the University of California Santa Barbara, that incorporates eqn.(9.1) to estimate the thickness of copper film we should use for a given thickness of aluminum film in order to reduce the T_c of aluminum by about 50%. From the numerical prediction of the Usadel solution, we used 65 nm of aluminum and 30 nm of copper. The copper traps are squares with area $4 \mu\text{m}^2$ and patterned in the center conductor of the resonator.

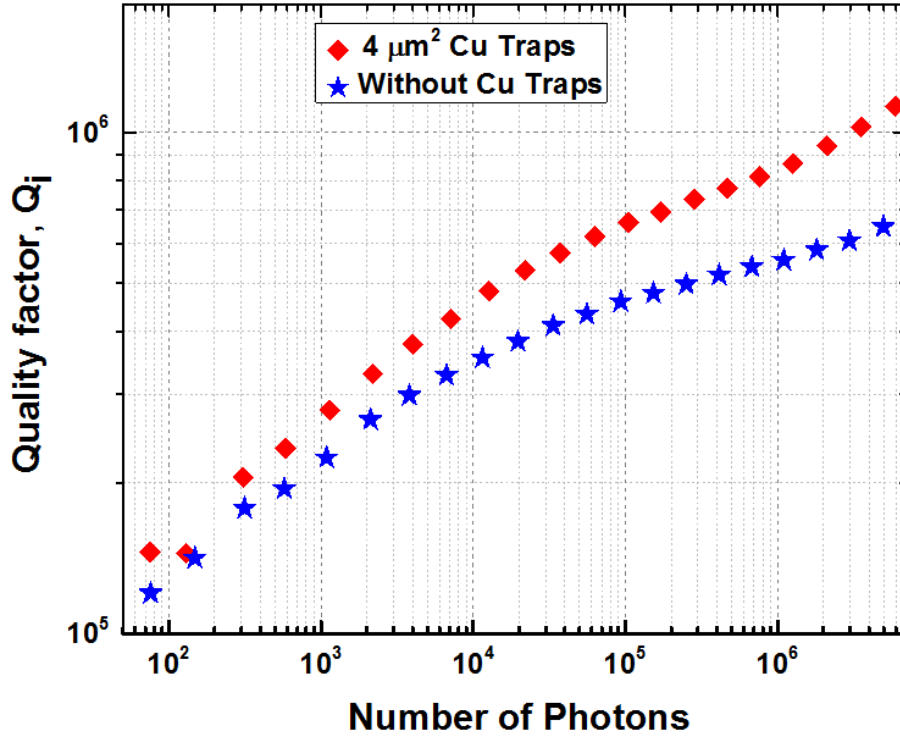


Figure 9.2: Internal quality factor of resonator with and without copper traps.

The spacing between the copper traps is $12 \mu\text{m}$, and we chose the dimensions and spacing of traps to avoid any the metallic loss from copper in locations with large microwave currents. To check the transition temperature T_c of the bilayer film, we evaporated 30 nm of copper onto whole silicon wafer and on top of it we evaporated 65 nm of aluminum. Note that before we evaporate copper we used an adhesion layer of 2.5 – 3.5 nm of titanium. Next we patterned resonators on this bilayer film and measured T_c using ADR and the measured $T_c = 0.6 \text{ K}$ is consistent with our Matlab simulations. The metallic loss of the copper in this case prevented us from measuring any resonances, but we could still measure T_c from the step in S_{21} through the feedline at different temperatures. Therefore, we are confident that the T_c of the copper traps we engineered was more than 50% less than the T_c value at locations where we do not put copper traps. Using the equation for the energy gap in terms of T_c , $\Delta_0 = 1.76k_B T_c$, we can find that the energy gap of the copper traps is reduced by more than half the value of energy gap for aluminum film. With this procedure we find that the quasiparticles traps can actually reduce the density of nonequilibrium quasiparticles as shown in figure 9.2. Future

experiments could reveal the optimal dimensions and spacing of these copper traps as well as their locations in the device for efficient reduction of quasiparticles.

9.2 Conclusions

We have described our field-cooled experiments of the superconducting coplanar waveguide resonators made of thin films of aluminum evaporated onto a silicon substrate. We showed that we can trap single vortices one at a time and we quantified the microwave loss due to a single vortex. The measured loss from a single vortex in the microwave resonator is consistent with the theoretical predictions. We showed that when vortices are trapped at locations of vanishing local current density, they can actually reduce the density of nonequilibrium quasiparticles. We performed numerical simulations of the reduction of nonequilibrium quasiparticles by taking into account recombination of quasiparticles and their trapping by vortices. The simulation results are consistent with our finding in experiments. By injecting nonequilibrium quasiparticles using normal metal-insulator-superconductor (NIS) tunnel junction, we again showed that vortices reduce the microwave loss due to quasiparticles. We are currently exploring alternative methods to reduce the density of nonequilibrium quasiparticles, among techniques we are exploring are cuts in ground plane and the use of copper traps. In addition, we have qualitatively studied the vortex nonlinearity at microwave frequencies. In fact, when vortices are driven by high microwave currents, their fast back-and-forth motion induces an electric field. This accelerates quasiparticles in the vortex core such that they gain energy and can escape from the inside of vortex cores which results in the reduction of the vortex viscosity and hence in an increase of vortex velocity. In our experiments, this nonlinear process results in an increase in the vortex loss with microwave drive power. We have found that the increase in loss depends on the details of vortex distributions or pinning in the microwave resonator.

Bibliography

- [1] U. Mizutani, *Introduction to the Electron Theory of Metals* (Cambridge University Press, 2004).
- [2] G. Stan, S. B. Field, and J. M. Martinis, *Physical Review Letters* **92**, 097003 (2004).
- [3] I. Nsanzineza and B. L. T. Plourde, *Physical Review Letters* **113**, 117002 (2014).
- [4] P. K. Day, H. G. LeDuc, B. A. Mazin, A. Vayonakis, and J. Zmuidzinas, *Nature* **425**, 817 (2003).
- [5] E. A. Tholn, A. Ertl, E. M. Doherty, F. M. Weber, F. Grgis, and D. B. Haviland, *Applied Physics Letters* **90** (2007).
- [6] M. A. Castellanos-Beltran and K. W. Lehnert, *Applied Physics Letters* **91** (2007).
- [7] R. Simon, R. Hammond, S. Berkowitz, and B. A. Willemsen, *Proceedings of the IEEE* **92**, 1585 (2004), ISSN 0018-9219.
- [8] J. A. Schreier, A. A. Houck, J. Koch, D. I. Schuster, B. R. Johnson, J. M. Chow, J. M. Gambetta, J. Majer, L. Frunzio, M. H. Devoret, et al., *Physical Review B* **77**, 180502 (2008).
- [9] J. Majer, J. M. Chow, J. M. Gambetta, J. Koch, B. R. Johnson, J. A. Schreier, L. Frunzio, D. I. Schuster, A. A. Houck, A. Wallraff, et al., *Nature* **449**, 443 (2007).
- [10] R. H. Koch, G. A. Keefe, F. P. Milliken, J. R. Rozen, C. C. Tsuei, J. R. Kirtley, and D. P. DiVincenzo, *Physical Review Letters* **96**, 127001 (2006).
- [11] H. Wang, M. Hofheinz, M. Ansmann, R. C. Bialczak, E. Lucero, M. Neeley, A. D. O'Connell, D. Sank, J. Wenner, A. N. Cleland, et al., *Physical Review Letters* **101**, 240401 (2008).
- [12] M. Hofheinz, H. Wang, M. Ansmann, R. C. Bialczak, E. Lucero, M. Neeley, A. D. O'Connell, D. Sank, J. Wenner, J. M. Martinis, et al., *Nature* **459**, 546 (2009).

- [13] A. Wallraff, D. I. Schuster, A. Blais, L. Frunzio, J. Majer, M. H. Devoret, S. M. Girvin, and R. J. Schoelkopf, *Physical Review Letters* **95**, 060501 (2005).
- [14] M. Metcalfe, E. Boaknin, V. Manucharyan, R. Vijay, I. Siddiqi, C. Rigetti, L. Frunzio, R. J. Schoelkopf, and M. H. Devoret, *Physical Review B* **76**, 174516 (2007).
- [15] J. E. Johnson, E. M. Hoskinson, C. Macklin, D. H. Slichter, I. Siddiqi, and J. Clarke, *Physical Review B* **84**, 220503 (2011).
- [16] A. Lupaşcu, E. F. C. Driessen, L. Roschier, C. J. P. M. Harmans, and J. E. Mooij, *Physical Review Letters* **96**, 127003 (2006).
- [17] J. M. Martinis, K. B. Cooper, R. McDermott, M. Steffen, M. Ansmann, K. D. Osborn, K. Cicak, S. Oh, D. P. Pappas, R. W. Simmonds, et al., *Physical Review Letters* **95**, 210503 (2005).
- [18] A. OConnell, M. Ansmann, R. Bialczak, M. Hofheinz, N. Katz, E. Lucero, C. McKenney, M. Neeley, H. Wang, E. Weig, et al., *Applied Physics Letters* **92**, 112903 (2008).
- [19] H. Wang, M. Hofheinz, J. Wenner, M. Ansmann, R. C. Bialczak, M. Lenander, E. Lucero, M. Neeley, A. D. OConnell, D. Sank, et al., *Applied Physics Letters* **95**, 233508 (2009).
- [20] T. Lindström, J. E. Healey, M. S. Colclough, C. M. Muirhead, and A. Y. Tzalenchuk, *Physical Review B* **80**, 132501 (2009).
- [21] R. Barends, H. L. Hortensius, T. Zijlstra, J. J. A. Baselmans, S. J. C. Yates, J. R. Gao, and T. M. Klapwijk, *Applied Physics Letters* **92**, 223502 (2008).
- [22] R. Barends, N. Vercruyssen, A. Endo, P. J. de Visser, T. Zijlstra, T. M. Klapwijk, P. Diener, S. J. C. Yates, and J. J. A. Baselmans, *Applied Physics Letters* **97**, 023508 (2010).
- [23] R. Barends, J. Wenner, M. Lenander, Y. Chen, R. C. Bialczak, J. Kelly, E. Lucero, P. OMalley, M. Mariantoni, D. Sank, et al., *Applied Physics Letters* **99** (2011).
- [24] A. D. Corcoles, J. M. Chow, J. M. Gambetta, C. Rigetti, J. R. Rozen, G. A. Keefe, M. Beth Rothwell, M. B. Ketchen, and M. Steffen, *Applied Physics Letters* **99**, 181906 (2011).
- [25] P. J. de Visser, J. J. A. Baselmans, P. Diener, S. J. C. Yates, A. Endo, and T. M. Klapwijk, *Physical Review Letters* **106**, 167004 (2011).
- [26] J. N. Ullom, P. A. Fisher, and M. Nahum, *Applied Physics Letters* **73**, 2494 (1998).
- [27] A. Golubov and E. Houwman, *Physica C: Superconductivity* **205**, 147 (1993), ISSN 0921-4534.

- [28] J. T. Peltonen, J. T. Muhonen, M. Meschke, N. B. Kopnin, and J. P. Pekola, *Physical Review B* **84**, 220502 (2011).
- [29] M. Tinkham, *Introduction to Superconductivity* (McGraw-Hill, 1996), 2nd ed.
- [30] P. J. Ford and G. A. Saunders, *The Rise of the Superconductors* (CRC Press, 2004).
- [31] A. V. Narlikar and S. N. Ekbote, *Superconductivity and Superconducting materials* (South Asia Publishers, New Delhi, Madras, 1983).
- [32] J. Bardeen, L. N. Cooper, and J. R. Schrieffer, *Physical Review* **108**, 1175 (1957).
- [33] P. Muller and A. V. Ustinov, eds., *The Physics of Superconductors, Introduction to Fundamentals and Applications* (Springer, 1997).
- [34] J. Gao, Ph.D. thesis, California institute of technology (2008).
- [35] J. Zmuidzinas, *Annual Review of Condensed Matter Physics* **3**, 169 (2012).
- [36] M. Lenander, H. Wang, R. C. Bialczak, E. Lucero, M. Mariani, M. Neeley, A. D. O'Connell, D. Sank, M. Weides, J. Wenner, et al., *Physical Review B* **84**, 024501 (2011).
- [37] J. N. Ullom, Ph.D. thesis, Harvard graduate school of arts and sciences (1998).
- [38] J. B. Ketterson and S. N. Song, *Superconductivity* (Cambridge University Press, 1999).
- [39] C. Song, Ph.D. thesis, Syracuse University (2011).
- [40] R. P. Huebener, *Magnetic Flux Structures in Superconductors* (Springer Series in Solid-State Sciences, 1979).
- [41] B. L. T. Plourde, Ph.D. thesis, University of Illinois at Urbana-Champaign (2000).
- [42] R. P. Huebener, slac.stanford.edu (1979).
- [43] J. Pearl, *Applied Physics Letters* **5**, 65 (1964).
- [44] K. Maki, *Annals of Physics* **34**, 363 (1965).
- [45] F. E. Harper and M. Tinkham, *Physical Review* **172**, 441 (1968).
- [46] J. A. Cape, *Physical Review* **166**, 432 (1968).
- [47] P. Tholfsen and H. Meissner, *Physical Review* **185**, 653 (1969).
- [48] G. Cody, *Physics Letters A* **37**, 295 (1971).

- [49] M. Tinkham, *Physical Review* **129**, 2413 (1963).
- [50] M. D. Maloney, F. de la Cruz, and M. Cardona, *Physics Review B* **5**, 3558 (1972).
- [51] B. Brandt, R. Parks, and R. Chaudhari, *Journal of Low Temperature Physics* **4**, 41 (1971), ISSN 0022-2291.
- [52] H. Boersch, U. Kunze, B. Lischke, and W. Rodewald, *Physical Letters* **44A**, 273 (1973).
- [53] B. Lischke and W. Rodewald, *Physics status solidi (b)* **63**, 97 (1974).
- [54] W. Rodewald, *Physical Letters* **55A**, 135 (1975).
- [55] G. J. Dolan and J. Silcox, *Physical Review Letters* **30**, 603 (1973).
- [56] G. Dolan, *Journal of Low Temperature Physics* **15**, 111 (1974).
- [57] G. Dolan, *Journal of Low Temperature Physics* **15**, 133 (1974), ISSN 0022-2291.
- [58] E. Guyon, A. Caroli, and A. Martinet, *Journal of Physical Radium* **25**, 683 (1964).
- [59] J. Pearl, *Journal of Applied Physics* **37**, 4139 (1966).
- [60] G. Lasher, *Physical Review* **154**, 345 (1967).
- [61] A. L. Fetter and P. C. Hohenberg, *Physical Review* **159**, 330 (1967).
- [62] K. Gray, *Journal of Low Temperature Physics* **15**, 335 (1974), ISSN 0022-2291.
- [63] S. Onori and A. Rogani, *Physica B+C* **132**, 217 (1985).
- [64] J. Bardeen and M. J. Stephen, *Physical Review* **140**, A1197 (1965).
- [65] K. K. Likharev, *Soviet radiophysics* **14**, 722 (1972).
- [66] C. Song, T. W. Heitmann, M. P. DeFeo, K. Yu, R. McDermott, M. Neeley, J. M. Martinis, and B. L. T. Plourde, *Physical Review B* **79**, 174512 (2009).
- [67] M. Liang and M. N. Kunchur, *Physical Review B* **82**, 144517 (2010).
- [68] W. Klein, R. Huebener, S. Gauss, and J. Parisi, *Journal of Low Temperature Physics* **61**, 413 (1985).
- [69] H. Suhl, *Physical Review Letters* **14** (1965).
- [70] A. T. Fiory and A. F. Hebard, *AIP Conference Proceedings* **58**, 293 (1980).

- [71] M. W. Coffey and J. R. Clem, *Physical Review Letter* **67**, 386 (1991).
- [72] J. Andrews and V. Mathew, *Journal of Applied Physics* **114**, 163914 (2013).
- [73] J. I. Gittleman and B. Rosenblum, *Physical Review Letters* **16**, 734 (1966).
- [74] M. W. Coffey and J. R. Clem, *Physical Review Letters* **67**, 386 (1991).
- [75] E. H. Brandt, *Physica Scripta* **1992**, 63 (1992).
- [76] N. Pompeo and E. Silva, *Physical Review B* **78**, 094503 (2008).
- [77] R. Barends, H. Hortensius, T. Zijlstra, J. Baselmans, S. Yates, J. Gao, and T. Klapwijk, *Applied Physics Letters* **92** (2008).
- [78] P. J. de Visser, J. J. A. Baselmans, P. Diener, S. J. C. Yates, A. Endo, and T. M. Klapwijk, *Applied physics letters* **100**, 162601 (2011).
- [79] J. M. Martinis, M. Ansmann, and J. Aumentado, *Physical Review Letters* **103**, 097002 (2009).
- [80] R. Barends, S. van Vliet, J. J. A. Baselmans, S. J. C. Yates, J. R. Gao, and T. M. Klapwijk, *Journal of Physics: Conference Series* **150**, 052016 (2009).
- [81] U. Vool, I. M. Pop, K. Sliwa, B. Abdo, C. Wang, T. Brecht, Y. Y. Gao, S. Shankar, M. Hatridge, G. Catelani, et al., *Physical Review Letters* **113**, 247001 (2014).
- [82] A. Rothwarf and B. N. Taylor, *Physal Revieew Letters* **19**, 27 (1967).
- [83] D. M. Pozar, *Microwave Engineering* (John Wiley and Sons, Inc., 2007), 3rd ed.
- [84] R. Simons, *Coplanar Waveguide Circuits, Components, and Systems* (Wley-Interscience, 2001).
- [85] B. A. Mazin, Ph.D. thesis, California Institute of Technology, Pasadena, California (2004).
- [86] P. de Visser, Ph.D. thesis, Delft University of technology (2014).
- [87] M. Calvo, Ph.D. thesis, Sapienza University of Roma (2008).
- [88] C. Wang, C. Axline, Y. Y. Gao, T. Brecht, Y. Chu, L. Frunzio, M. H. Devoret, and R. J. Schoelkopf, *Applied Physics Letters* **107**, 162601 (2015).
- [89] J. P. Pekola, D. V. Anghel, T. I. Suppala, J. K. Suoknuuti, A. J. Manninen, and M. Manninen, *Applied Physics Letters* **76**, - (2000).

- [90] J. Gao, M. Daal, A. Vayonakis, S. Kumar, J. Zmuidzinas, B. Sadoulet, B. Mazin, P. Day, and H. Leduc, *Applied Physics Letters* **92**, 152505 (2008).
- [91] J. Gao, M. Daal, J. Martinis, A. Vayonakis, J. Zmuidzinas, B. Sadoulet, B. Mazin, P. Day, and H. Leduc, *Applied Physics Letters* **92** (2008).
- [92] D. P. Pappas, M. R. Vissers, D. S. Wisbey, J. S. Kline, and J. Gao, *Applied Superconductivity, IEEE Transactions on* **21**, 871 (2011), ISSN 1051-8223.
- [93] A. Bruno, S. Skacel, C. Kaiser, S. Wnsch, M. Siegel, A. Ustinov, and M. Lisitskiy, *Physics Procedia* **36**, 245 (2012), ISSN 1875-3892.
- [94] A. Megrant, C. Neill, R. Barends, B. Chiaro, Y. Chen, L. Feigl, J. Kelly, E. Lucero, M. Mariantoni, P. J. J. OMalley, et al., *Applied Physics Letters* **100**, 113510 (2012).
- [95] C. Song, M. P. DeFeo, K. Yu, and B. L. T. Plourde, *Applied Physics Letters* **95**, 232501 (2009).
- [96] D. Bothner, T. Gaber, M. Kemmler, D. Koelle, and R. Kleiner, *Applied Physics Letters* **98**, 102504 (2011).
- [97] D. Bothner, C. Clauss, E. Koroknay, M. Kemmler, T. Gaber, M. Jetter, M. Scheffler, P. Michler, M. Dressel, D. Koelle, et al., *Applied Physics Letters* **100**, 012601 (2012).
- [98] S. E. d. Graaf, A. V. Danilov, A. Adamyan, T. Bauch, and S. E. Kubatkin, *Journal of Applied Physics* **112**, 123905 (2012).
- [99] F. Pobell, *Matter and Methods at Low Temperatures* (Springer, 2007), revised and expanded 3rd ed.
- [100] K. G. White, *Experimental Techniques in Low-Temperature Physics* (Clarendon Press, 1979), 3rd ed.
- [101] G. Ventura and L. Risegari, *The Art of Cryogenics, Low-Temperature Experimental Techniques* (Elsevier Ltd, 2008), 1st ed.
- [102] *Adiabatic Demagnetization Refrigerator, Installation and Operation Manual for models 102 Denali, 103 Rainier, 104 Olympus and 106 Shasta*, High Precision Devices (HPD) , Inc. (2012).
- [103] M. Golio and J. Golio, eds., *RF and Microwave Circuits, Measurements, and Modeling* (CRC Press, Taylor and Francis group, 2008), 2nd ed.
- [104] I. J. Collier and A. D. Skinner, eds., *Microwave Measurements* (The institution of engineering and technology, 2007), 3rd ed.

- [105] R. Barends, Ph.D. thesis, Delft University of technology (2009).
- [106] J. E. Healey, T. Lindström, M. S. Colclough, C. M. Muirhead, and A. Y. Tzalenchuk, *Applied Physics Letters* **93**, 043513 (2008).
- [107] E. Bronson, M. P. Gelfand, and S. B. Field, *Physical Review B* **73**, 144501 (2006).
- [108] A. Anthore, H. Pothier, and D. Esteve, *Physical Review Letters* **90**, 127001 (2003).
- [109] S. Friedrich, K. Segall, M. C. Gaidis, C. M. Wilson, D. E. Prober, A. E. Szymkowiak, and S. H. Moseley, *Applied Physics Letters* **71**, 3901 (1997).
- [110] L. N. Trefethen et al, *CHEBFUN version 4.2* (Pafnuty Publications, 2011).
- [111] S. B. Kaplan, C. C. Chi, D. N. Langenberg, J. J. Chang, S. Jafarey, and D. J. Scalapino, *Phys. Rev. B* **14**, 4854 (1976).
- [112] C. C. Chi and J. Clarke, *Physics Review B* **19**, 4495 (1979).
- [113] A. Larkin and Y. Ovchinnikov, *Journal of Low Temperature Physics* **34**, 409 (1979).
- [114] S. Doettinger, R. Huebener, and A. Khle, *Physica C: Superconductivity* **251**, 285 (1995), ISSN 0921-4534.
- [115] F. Lefloch, C. Hoffmann, and O. Demolliens, *Physica C: Superconductivity* **319**, 258 (1999), ISSN 0921-4534.
- [116] G. Grimaldi, A. Leo, C. Cirillo, C. Attanasio, A. Nigro, and S. Pace, *Journal of Physics: Condensed Matter* **21**, 254207 (2009).
- [117] G. Grimaldi, A. Leo, D. Zola, A. Nigro, S. Pace, F. Laviano, and E. Mezzetti, *Physical Review B* **82**, 024512 (2010).
- [118] A. I. Bezuglyj and V. A. Shklovskij, *Physica C: Superconductivity* **202**, 234 (1992).
- [119] A. Leo, G. Grimaldi, A. Nigro, S. Pace, N. Verellen, A. Silhanek, W. Gillijns, V. Moshchalkov, V. Metlushko, and B. Ilic, *Physica C: Superconductivity* **470**, 904 (2010), vortex Matter in Nanostructured Superconductors.
- [120] G. Grimaldi, A. Leo, C. Cirillo, A. Casaburi, R. Cristiano, C. Attanasio, A. Nigro, S. Pace, and R. Huebener, *Journal of Superconductivity and Novel Magnetism* **24**, 81 (2011), ISSN 1557-1939.

- [121] A. V. Silhanek, A. Leo, G. Grimaldi, G. R. Berdiyrov, M. V. Miloevic, A. Nigro, S. Pace, N. Verellen, W. Gillijns, V. Metlushko, et al., *New Journal of Physics* **14**, 053006 (2012).
- [122] A. Leo, G. Grimaldi, A. Nigro, E. Bruno, F. Priolo, and S. Pace, *Physica C: Superconductivity* **503**, 140 (2014).
- [123] G. Grimaldi, A. Leo, A. Nigro, S. Pace, C. Cirillo, and C. Attanasio, *Physica C: Superconductivity and its Applications* **468**, 765 (2008), ISSN 0921-4534, proceedings of the Fifth International Conference on Vortex Matter in Nanostructured Superconductors Proceedings of the Fifth International Conference on Vortex Matter in Nanostructured Superconductors.
- [124] J. M. Martinis, G. Hilton, K. Irwin, and D. Wollman, *Nuclear Instruments and Methods in Physics Research Section A: Accelerators, Spectrometers, Detectors and Associated Equipment* **444**, 23 (2000).
- [125] K. D. Usadel, *Physical Review Letters* **25**, 507 (1970).
- [126] S. Guéron, H. Pothier, N. O. Birge, D. Esteve, and M. H. Devoret, *Physical Review Letters* **77**, 3025 (1996).

VITA

NAME OF AUTHOR: Ibrahim Nsanzineza

PLACE OF BIRTH: Gatsibo District, East Province, Rwanda

DATE OF BIRTH: June 04, 1979

GRADUATE AND UNDERGRADUATE SCHOOLS ATTENDED:

Syracuse University, Syracuse, New York

University of Cape Town,
Cape Town, South Africa

Kigali Institute of Education, Kigali, Rwanda

DEGREES AWARDED:

Master of Science in Physics, 2012

Syracuse University

Master's diploma in Mathematical Sciences, 2008

University of Cape Town

Bachelor of Science in Physics and Chemistry, 2005

Kigali Institute of Education

PROFESSIONAL EXPERIENCE:

Graduate Research Assistant, Syracuse University, 2011 - 2015

Graduate Teaching Assistant, Syracuse University, 2008 - 2011

Undergraduate Teaching Assistant, 2006 - 2007

Kigali Institute of Education, Kigali, Rwanda

High School Physics Teacher, 2005 - 2006

Muhura High School, Gatsibo District, East Province, Rwanda

JOURNAL PUBLICATIONS:

I. Nsanzineza, B. L. T. Plourde: Trapping a Single Vortex and Reducing Quasi-particles in a Superconducting Resonator. *Physical Review Letters* 09/2014; 113(11):117002.

DOI:10.1103/PhysRevLett.113.117002